Analysis of Alterations in Cellular Architecture by cryo-Soft X-ray Tomography and Ultrastructure Expansion Microscopy

Inaugural-Dissertation

to obtain the academic degree

Doctor rerum naturalium (Dr. rer. nat.)

submitted to the Department of Biology, Chemistry, Pharmacy

of Freie Universität Berlin

by

Michael Carsten Alexander Dyhr

2024

This doctorate study was conducted between April 2020 and February 2024 under supervision of Prof. Dr. Helge Ewers at the Institute of Chemistry and Biochemistry in the Department of Biology, Chemistry, Pharmacy of the Freie Universität Berlin.

1st reviewer: Prof. Dr. Helge Ewers

Freie Universität Berlin
Department of Biology, Chemistry, Pharmacy
Institute of Chemistry and Biochemistry
Thielallee 63
14195 Berlin
Germany

2nd reviewer: Prof. Dr. Gerd Schneider

Helmholtz Zentrum Berlin für Materialien und Energie GmbH
X-ray Microscopy Group
Albert-Einstein-Str. 15
12489 Berlin
Germany

Date of defense: May 27th, 2024

Declaration of Authorship

Herewith I, Michael Carsten Alexander Dyhr, certify that I have prepared and written my thesis independently and that I have not used any sources and aids other than those indicated by me. The intellectual property of other authors has been marked accordingly. I also declare that I have not applied for an examination procedure at any other institution and that I have not submitted the dissertation in this or any other form to any other faculty as a dissertation.

Summary

Zusammenfassung

Das zentrale Ziel dieser Dissertation war es, Veränderungen der zellulären Architektur zu visualisieren, welche durch Umweltfaktoren wie z.B. Wirkstoffbehandlungen oder Virusinfektion verursacht werden. Hochauflösende mikroskopische Analyse solcher Veränderungen ist von zentraler Bedeutung für die Aufklärung der Entstehung von Krankheiten und für die Entwicklung wirksamer Therapien. Die COVID-19 Pandemie hat einmal mehr die Wichtigkeit dessen unterstrichen, als weltweit Millionen von Menschen durch das SARS-CoV-2 Virus infiziert wurden, teils mit tödlichem Verlauf. Der Einsatz hochauflösender Kryo-Röntgentomographie (cryo-SXT) ermöglichte die dreidimensionale Visualisierung schnell auftretender Veränderungen in Zellen, welche mit SARS-CoV-2 oder dem felinen infektiösen Peritonitis Virus (FIPV) infiziert waren. Vorbehandlung mit bereits zugelassenen Medikamenten, welche als erfolgreiche Kandidaten aus vorherigen Studien gegen SARS-CoV-2 hervorgegangen waren, beeinträchtigte die durch Virus induzierten zellulären Veränderungen. Mittels cryo-SXT konnte die Bildung Lysosom-assoziierter dunkelrandiger Vesikel (DRVs) gezeigt werden. Per Transmissionselektronenmikroskopie wurde die Feinstruktur dieser Vesikel als multilamellare Lipidablagerungen nachgewiesen. Das bemerkenswerte Wechselspiel der durch Wirkstoffe und Viren induzierten Veränderungen hinsichtlich der Größe und Anzahl der lysosomalen DRVs deutet auf eine wichtige Rolle lysosomaler Funktionen bei der Hemmung der Virusreplikation durch die Wirkstoffe hin. Ein wahrscheinlicher Mechanismus der Virushemmung ist die Störung des Virus beim Austritt aus dem Lysosom in Richtung Zytoplasma. Ein weiterer wahrscheinlicher Mechanismus ist die Störung der Mobilisierung zellulärer Lipide, welche für die Umprogrammierung der Zelle für die Virusreplikation benötigt werden. Um diese Modelle umfassend zu testen, bedarf es neben cryo-SXT ergänzender Methoden für effizientere Screenings zur Visualisierung solcher Veränderungen der zellulären Ultrastruktur. Das erst kürzlich entwickelte Verfahren der Ultrastruktur-Expansionsmikroskopie (U-ExM) ist hierfür ein vielversprechendes Mittel. Beim Vergleich zwischen cryo-SXT und U-ExM hinsichtlich der Präservation verschiedener zellulärer Strukturen wurde deutlich, dass die Morphologie großer Organellen wie etwa Nukleus und Plasmamembran in U-ExM sehr effizient dargestellt werden können, während kleine oder lipid-reiche Organellen nur bedingt originalgetreu zu erhalten sind. Diese Ergebnisse verdeutlichen einerseits den Wert von cryo-SXT, aber auch das Potential von U-ExM, welches einen höheren Durchsatz, aber eine geringere Auflösung und Strukturgenauigkeit als cryo-SXT erreicht. U-ExM eignet sich so hervorragend zur Optimierung experimenteller Parameter zur Strukturanalyse und bietet so einen wichtigen Schritt zu höherer Effizienz von cryo-SXT. Ein weiterer Schritt ist die Automatisierung der Segmentierung von cryo-SXT-Datensätzen. Zu diesem Zweck wurde ein neurales Netzwerk mit einer großen Menge an cryo-SXT-Daten trainiert und validiert. Dieses Netzwerk ist in der Lage, zelluläre Strukturen in neuen Datensätzen vollautomatisch innerhalb von weniger als einer halben Stunde auf herkömmlichen GPUs zu segmentieren. Dies beschleunigt den Prozess der Datenanalyse auf signifikante Weise. Zusammengenommen zeigen die vorliegenden Ergebnisse, wie cryo-SXT, U-ExM und Deep Learning einander bei der Beantwortung wichtiger biologischer Fragen wirkungsvoll ergänzen können.

Abstract

The central aim of this thesis was to visualize changes in cellular architecture induced by environmental factors such as drug treatment or viral infection. High-resolution microscopic analysis of such alterations is crucial to elucidate the mechanisms of disease, as well as to develop potential therapies. The importance thereof was clearly underscored by the COVID-19 pandemic, whose causative agent, the novel severe acute respiratory syndrome coronavirus 2 (SARS-CoV-2), infected and killed millions of people across the globe. By using high-resolution 3D-imaging by cryo-soft X-ray tomography (cryo-SXT), rapid changes in the cellular ultrastructure upon infection with SARS-CoV-2 or feline infectious peritonitis virus (FIPV) could be visualized. The changes induced by viral infection were affected by treatment with FDA-approved drugs, which had previously emerged as candidates from drug-repurposing screens to combat SARS-CoV-2. Cryo-SXT analysis revealed formation of lysosome-associated dark-rimmed vesicles (DRVs), which were demonstrated to be multilamellar lipid deposits by transmission electron microscopy. The observed striking interplay of drug- and virus-induced alterations on the level of size and number of lysosome-associated DRVs suggests involvement of lysosomal function in the inhibition of the viruses by the drugs. It is likely that this inhibition is either due to impairment of lysosomal escape or due to reduced lipid availability for membrane remodeling essential for virus replication. To comprehensively test these models, complementary screening tools are required, which allow ultrastructural analysis at a higher throughput than cryo-SXT. For that, the recently developed ultrastructure expansion microscopy (U-ExM) is a promising technique. Comparing the structural preservation of cell organelles after the U-ExM sample preparation to that of cells acquired under near-native conditions in cryo-SXT, it emerged that the morphology of large organelles such as nuclei and plasma membrane can be visualized efficiently by U-ExM, while very small or lipid-dense structures were more difficult to preserve accurately. These results highlight the benefits of cryo-SXT, but also the potential of U-ExM to complement cryo-SXT with its higher throughput of ultrastructure visualization, even if its resolution is lower than that of cryo-SXT. Therefore, U-ExM can be used for experimental characterization for cryo-SXT, as one step towards more efficiency of cryo-SXT. Another step is to automate the segmentation of cryo-SXT tomograms. To that end, a deep learning platform was trained and validated on a large pool of cryo-SXT data acquired in this work. This convoluted neural network performs full annotation of cellular features in cryo-SXT tomograms within less than half an hour on consumer-grade GPUs, thereby significantly reducing the time required for data analysis. Taken together, these results illustrate how cryo-SXT, U-ExM and deep learning can be used complementarily to address highly relevant biological questions.

Graphical Abstract

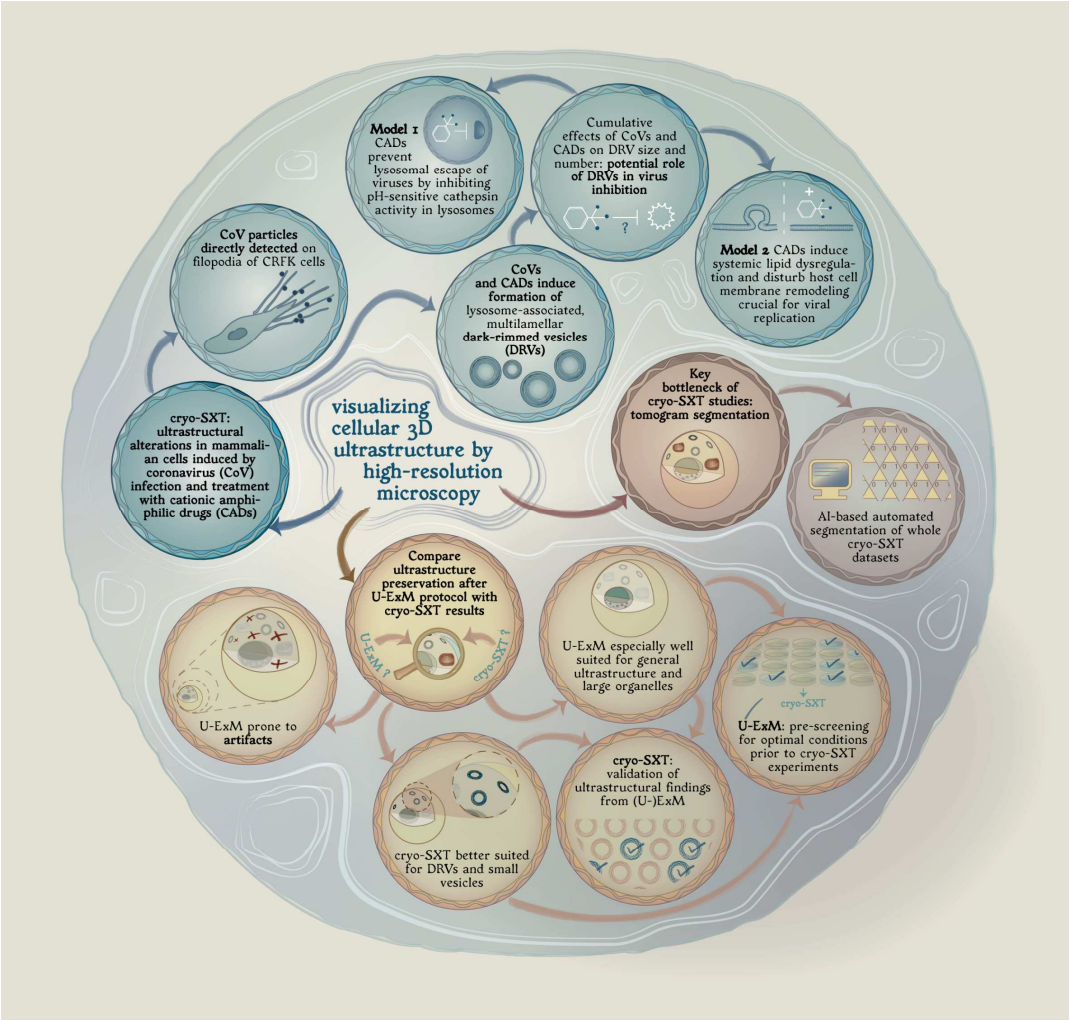

Table of Contents

List of Abbreviations

ABBR	Abbreviation
ASM	acid sphingomyelinase
AA	acrylamide
ALS	Advanced Light Source
APN	aminopeptidase N
ADE	antibody-dependent enhancement
BSL	biosafety level
CCOV	canine coronavirus
CAD	cationic amphiphilic drugs
CHIKV	Chikungunya virus
Con A	concanavalin A
CNN	convolutional neural network
COVID-19	Coronavirus Disease 2019
CLXM	correlative light and X-ray microscopy
CRFK	Crandell-Rees Feline Kidney
cryo-SXT	cryo-soft X-ray microscopy
DRV	dark-rimmed vesicle
DC-SIGN	Dendritic cell-specific ICAM-3 grabbing non-integrin
DENV	Dengue virus
DMSO	dimethyl sulfoxide
dSTORM	direct stochastic optical reconstruction microscopy
DMV	double-membrane vesicle
DMEM	Dulbecco‘s Modified Eagle Medium
EBOV	Ebola virus
EM	electron microscopy
ER	endoplasmic reticulum
EMA	European Medicines Agency
ExM	expansion microscopy
ExSTED	expansion STED microscopy
ExSRRF	expansion-enhanced super-resolution radial fluctuations
FCoV	feline coronavirus
FECV	feline enteric coronavirus
FIPV	feline infectious peritonitis virus
FOV	field of view
FM	fluorescence microscopy
FDA	Food and Drug Administration
FZP	Fresnel zone plate
FIASMA	functional inhibitor of acid sphingomyelinase
GA	glutaraldehyde
GPU	graphics processing unit
HZB	Helmholtz-Zentrum Berlin
HCV	hepatitis C virus
hpi	hours past infection
HCoV	human coronavirus
MβCD	methyl-β-cyclodextrin
MERS	Middle East respiratory syndrome

MLB	multilamellar body
MOI	multiplicity of infection
TEMED	N,N,N′,N′-Tetramethylethane-1,2-diamine
Bis	N,N′-Methylenedi(prop-2-enamide)
NIH	National Institute of Health
NHS	N-hydroxysuccinimide
NPD-A /-B /-C	Niemann-Pick disease type A / B / C
NPC	nuclear pore complex
PFA	paraformaldehyde
PBS	phosphate-buffered saline
RNA	ribonucleic acid
SARS-CoV(-1)	severe acute respiratory syndrome coronavirus 1
SARS-CoV-2	severe acute respiratory syndrome coronavirus 2
SIRT	Simultaneous Iterative Reconstruction Technique
SA	sodium acrylate
SDS	sodium dodecyl sulfate
SDS PAGE	sodium dodecyl sulfate–polyacrylamide gel electrophoresis
STED	stimulated emission depletion
STORM	stochastic optical reconstruction microscopy
SRRF	super-resolution radial fluctuations
TREX	Ten-fold robust expansion microscopy
TGEV	transmissible gastroenteritis coronavirus
TEM	transmission electron microscopy
TXM	transmission X-ray microscopy
U-ExM	ultrastructure expansion microscopy
VSV	vesicular stomatitis virus
WNV	West Nile virus
WGA	wheat germ agglutinin
WHO	World Health Organization
XRM	X-ray microscopy

1. Introduction

1.1. The Structure-Function Relationship and Cellular Architecture

The structure-function relationship is a central principle across scientific disciplines. It describes how the function of an entity is closely related to its structure and vice versa. Any entity can only exert functions which its structure permits and alterations of its structure can provide novel functions to this entity. This concept is extensively used by scientists, for instance to engineer novel structures based on desired functionality or to elucidate unknown functions of any given structure.

Eukaryotic cells have evolved to perform a plethora of physiological functions, such as nutrient uptake, energy metabolism, DNA replication, as well as biomolecule synthesis and degradation. Many of these functions are spatially coordinated by the structural organization of the cellular volume into compartments by means of semi-permeable lipid bilayers. This compartmentalization is a key principle in cell biology, as it allows a wide range of pH, ion concentrations, or enzymatic functions to be present inside a single, densely packed cell by division into organelles such as nucleus, endoplasmic reticulum, mitochondria, lysosomes, and others (see fig. 1-1).

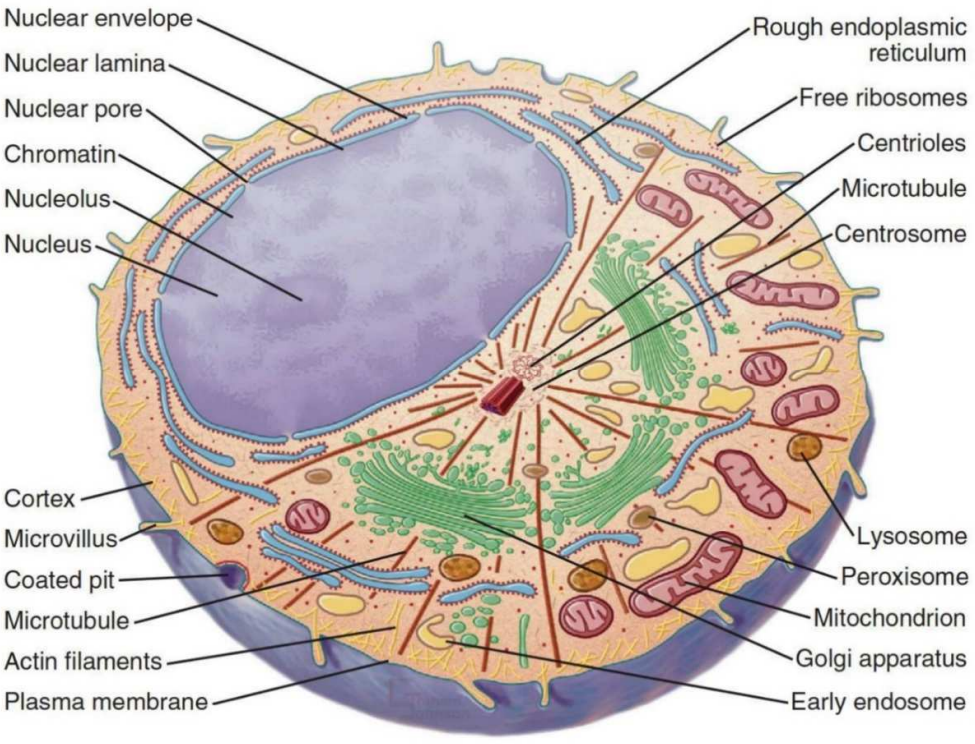

Figure 1-1: Overview of the Architecture of a Typical Eukaryotic Cell. Reprint from: J. L. Corden, C. Morrison, S. Maciver, D. Tollervey: *Cell Biology*, 3rd edition, 2017, with permission from Elsevier.

Not only the structure and function of individual organelles, but also their interactions and organization in the context of the whole cellular architecture are important fields for investigation. Microscopic characterization of the fine structure, or *ultrastructure*, of a cell can be used to better understand its function under normal conditions, as well as to identify morphological alterations caused by disease. Such knowledge is crucial to correctly diagnose a disease, as well as to identify the underlying pathogenesis and thereby develop potential treatments. This holds true for a wide range of diseases, from rare genetic disorders (fig. 1-2 A) to viral infections (fig. 1-2 B). Especially the latter received significant public attention due to the onset of the global Coronavirus Disease 19 (COVID-19) pandemic which began in late 2019.

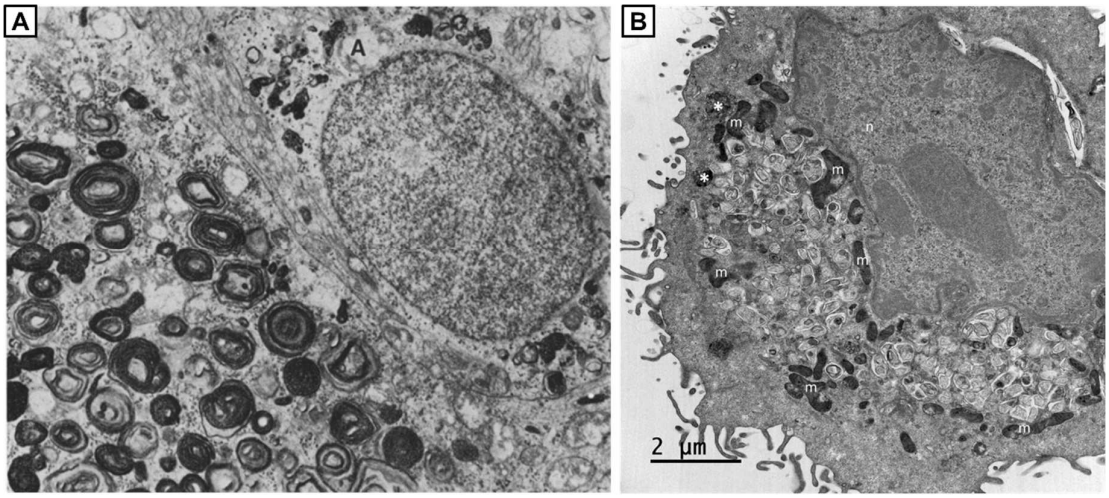

Figure 1-2: Alterations in Cellular Ultrastructure Are Important Hallmarks of Disease. A: Prominent formation of multilamellar, cytoplasmic bodies is shown in this electron Micrograph of a neuron from the cerebral cortex of a Friesian calf with GM1 gangliosidosis, a lysosomal storage disease. B: Electron micrograph of a Vero cell infected with SARS-CoV-2 for 24 hours reveals formation of an extensive network of double-membrane replication organelles. A: reused from Sheahan, Donnelly, Acta Neuropathol. 30(1):73-84 (1974)[1]. B: reused from Roingeard et al., Cell Mol Life Sci. 78(7):3565-3576 (2021)[2] both with permission from Springer Nature.

1.2. Biology of Coronaviruses and SARS-CoV-2

The causative agent of COVID-19 is the severe acute respiratory syndrome-related coronavirus 2 (SARS-CoV-2)[3], which emerged as a novel virus in 2019 and rapidly spread across the globe and evolved into a pandemic. Being a virus, it is not a fully autonomous living entity, but instead relies on the machinery of a host cell to produce its progeny. To accomplish that, any virus must successfully enter the host cell, release its genome, and hijack cellular machineries to generate copies of the viral genome and proteins, organize viral assembly and egress, while also evading the host cell defense mechanisms. To do that, it needs to functionally reprogram the host cell, which is also accompanied by structural remodeling of the cellular organization. Thus, studying

virus-induced ultrastructural alterations can help scientists to elucidate the process of viral function and develop targeted antiviral therapies that interfere with viral infection or replication.

SARS-CoV-2 is a member of the *Coronaviridae* family of enveloped, non-segmented positive-strand RNA viruses which infect vertebrates[3–5]. The Coronaviruses belong to the subfamily *Coronavirinae*, which consists of the genera *Alpha-, Beta-, Gamma-*, and *Deltacoronavirus*[6]. These viruses can cause respiratory or enteric disease in mammals and birds[4,7,8]. Before 2019, four endemic human coronaviruses (HCoVs) were known to exist: HCoV-229E, -NL63, (genus *Alphacoronavirus*) -OC43, and HKU-1 (genus *Betacoronavirus*)[7,9], as well as two epidemic human viruses, which caused serious outbreaks: the severe acute respiratory syndrome-related coronavirus (SARS-CoV)[10] in 2002 and the Middle East respiratory syndrome coronavirus (MERS-CoV)[11] in 2012[12]. SARS-CoV and MERS belong to the genus *Betacoronavirus*[9], as does the novel SARS-CoV-2[13], the causative agent of the COVID-19 pandemic.

Coronavirus virions are either spherical or pleiomorphic particles with average diameters of 80 - 120 nm[4]. These particles consist of the structural proteins Envelope (E), Membrane (M), and Spike (S) proteins which are embedded in the lipid envelope, as well as the Nucleocapsid (N) proteins which binds the RNA genome of the virus[4] (see fig. 1-3). The Spike protein of coronaviruses forms large protrusions from the virion surface and mediates attachment to the host cell receptor and fusion with the host cell membrane. The SARS-CoV-2 Spike protein is known to bind to the angiotensin-converting enzyme 2 (ACE2) on host cells and to undergo proteolytic activation and membrane fusion through cleavage by the cell-surface resident transmembrane protease serine subtype 2 (TMPRSS2) or endolysosomal cathepsins[8,9,13]. Accordingly, SARS-CoV-2 is believed to release its genome into the host cell either through direct TMPRSS-2-mediated fusion with the plasma membrane or through endocytosis and endolysosomal release through action of cathepsins[8,9].

The released positive-sense viral RNA genome is translated into two polyproteins, which are proteolytically processed into multiple non-structural proteins (nsp). These nsps perform a series of functions, such as RNA remodeling, RNA replication or remodeling of the host cell membrane system to form the replication organelles (fig. 1-3). Coronaviruses and other positive-strand RNA viruses form characteristic double-membrane vesicles (DMVs) as replication organelles[8,14]. These structures are 100 – 300 nm in size[15] and originate from the ER membrane[2,16,17] (fig. 1-3, 1-4).

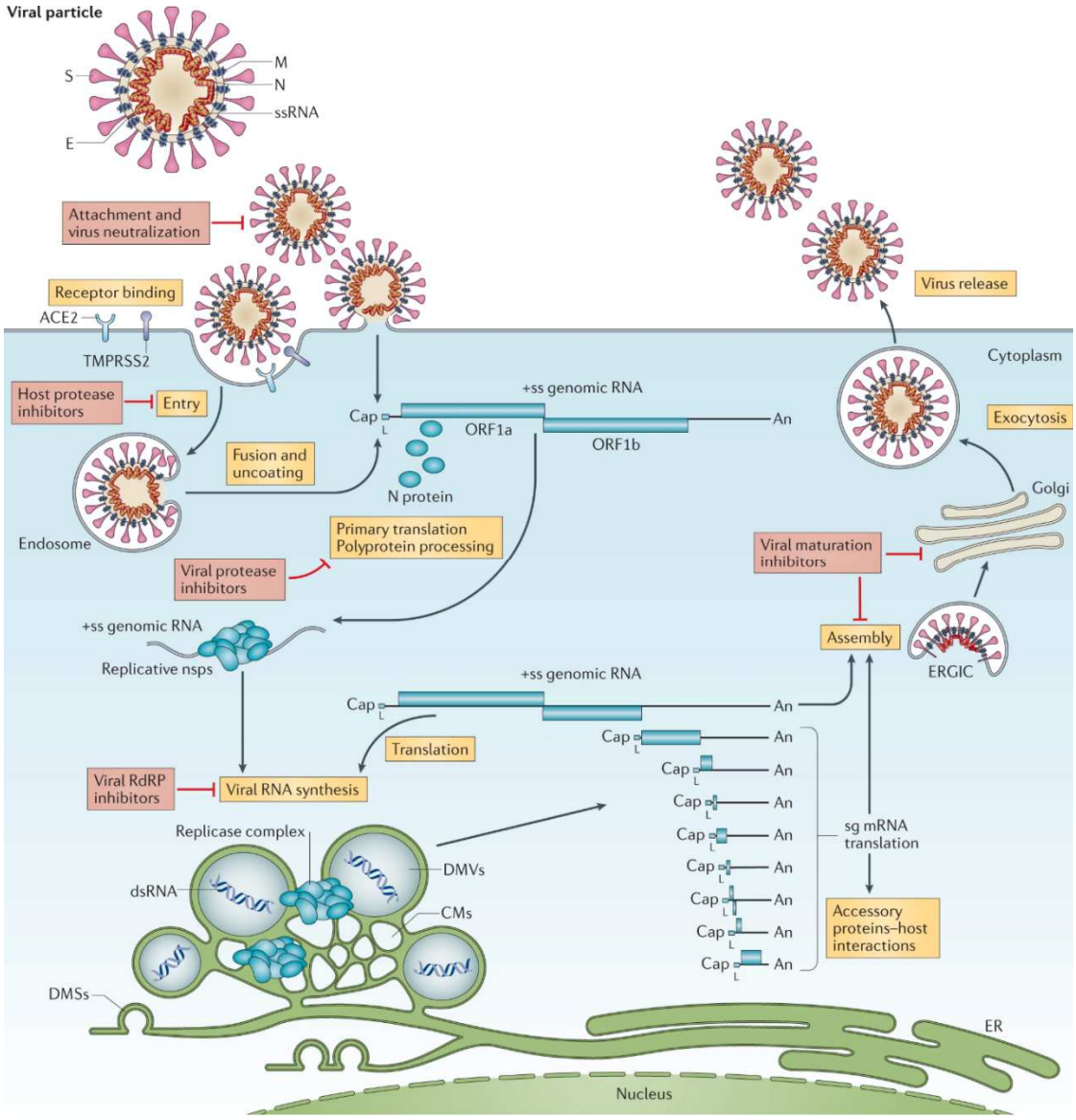

Figure 1-3: The Infectious Cycle of SARS-CoV-2. A schematic of the anatomy of a SARS-CoV-2 virion is shown on top with spike (S), envelope (E), membrane (M), nucleocapsid (N) proteins, as well as the positive-sense single-stranded RNA (+ssRNA) genome. Below, the infectious cycle is illustrated, as well as some intervention strategies (red boxes). The virus binds to its receptor ACE2 and may be either fused directly with the plasma membrane or be internalized through lysosomal escape and release its positive-sense single-stranded (+ss) RNA genome into the cell. Translation of the encoded open reading frames (ORF) produces non-structural proteins (nsps) which facilitate RNA synthesis in association with membranous viral replication organelles, consisting of double-membrane spherules (DMSs), convoluted membranes (CMs) and double-membrane vesicles (DMVs), which provide a favorable microenvironment for double-stranded RNA (dsRNA) intermediates for genome replication and transcription of subgenomic messenger RNA (sgRNA). New virions are assembled at the endoplasmic reticulum Golgi intermediate compartment (ERGIC), from which they are trafficked through the Golgi apparatus towards egress by exocytosis. RdRP: RNA-dependent RNA polymerase, An: 3' poly-A sequence. Reprint from V'kovski, P., Kratzel, A., Steiner, S. et al. Nat. Rev. Microbiology 19:155–170 (2021)[8], with permission from Springer Nature.

Besides replication, they also protect the viral genome against host defense mechanisms which detect RNA replication intermediates[8,16]. Transmembrane channels spanning across the both membrane layers have been observed by electron microscopy[18,19] and are believed to mediate export of viral RNA from the DMV interior[19] towards the assembly sites at the ER-Golgi intermediate compartment[20]. While extensive research has been directed at understanding the intricacies of the cellular reprogramming during the SARS-CoV-2 life cycle, many open questions remain as to the mechanisms underlying the reorganization of the cellular architecture, including, but not limited to, DMV formation and their interaction with host factors[8,15,16,20,21].

For the study of a dangerous and contagious pathogen such as SARS-CoV-2, experiments need to be conducted under high biosafety standards. This significantly limits the number of facilities that can perform experiments with fully active viruses and therefore incentivizes the use of model systems, such as, for example, other coronaviruses, that are not pathogenic to humans, such as the feline coronavirus.[6,12,13,18,19]

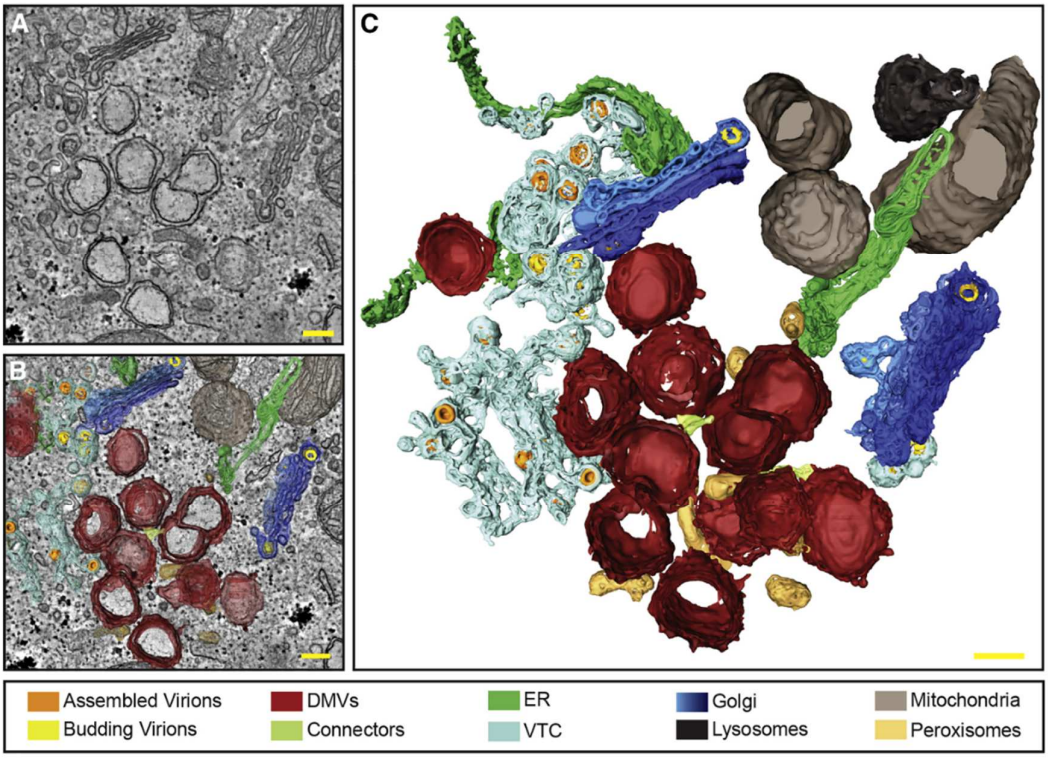

Figure 1-4: Remodeling of the Host Cell Membrane System by Infection with SARS-CoV-2. Virus-induced remodeling of the cellular membrane system is illustrated with the tomographic slice of a Calu-3 cell infected for 24 h with SARS-CoV-2 (A). The cellular and viral structures are highlighted once superimposed with the tomographic slice (B) and alone as a 3D-rendering (C). Scale bars: 200 nm. DMVs: Double-membrane vesicles. ER: endoplasmic reticulum. VTC: vesicular-tubular compartment. Reprint from: M. Cortese, Y. Schwab, R. Bartenschlager et al., Cell Host & Microbe 28, 853-866 (2020)[15] with permission from Elsevier.

1.3. The Feline Coronavirus

Even if the feline coronavirus (FCoV) belongs to a different genus than SARS-CoV-2, its systemic immunopathological effects and relatively advanced characterization[22,23] make it an attractive model system since it can be maintained and experimented with at biosafety level (BSL) 2 instead of BSL 3.

The feline coronavirus (FCoV) belongs to the *Alpha-coronavirus* genus which infects cats primarily through the fecal-oral route[24]. Two different, but closely related biotypes are known: the feline enteric coronavirus (FECV) and the feline infectious peritonitis virus (FIPV)[24], the latter being used in this work. While FECV is much more infectious and usually leads to asymptomatic or mild infections, the mutational variant FIPV is less infectious but leads to chronic and fatal disease in cats[25]. To date, it is not clear what determines the different clinical and epidemiologically behaviors of these otherwise similar biotypes[25], however it is believed that FIPV emerges by mutation in FECV-infected cats[26,27].

Serotype II FCoV and other Alpha-coronaviruses such as canine coronavirus (CCOV), transmissible gastroenteritis coronavirus (TGEV) and the human CoV HCoV-229E use the cell-surface resident aminopeptidase N (APN, or CD13) as the main receptor for on their respectively native host cells[26]. However, they all can also use the feline APN as a receptor[26,28]. FIPV enters cells through the endocytic route and escapes from endolysosomes upon proteolytic cleavage of its spike protein by cathepsin B[29].

Serotype II FCoV can be routinely propagated and purified in cell culture[25] and is therefore often used as model system for coronavirus infection.[26,29] The serotype II FIPV strain WSU 79-1146 used for the experiments in this dissertation is highly virulent and is known to also infect monocytes and macrophages through DC-SIGN[26,30], leading to systemic infection and inflammatory response[31], which is exacerbated by antibody-dependent enhancement (ADE)[22,32]. It is therefore an interesting model strain to study coronaviruses leading to systemic disease, such as SARS-CoV-2.

1.4. Repurposing of FDA-Approved Drugs to Combat Coronavirus Infection.

Most of the work related to this thesis was performed during the COVID-19 pandemic. Laboratories all across the planet started working towards better understanding how the virus infects humans, causes disease, and how it could be potentially combated by pharmaceutical and non-pharmaceutical means. Even if now, by the time of writing this thesis, the impact of SARS-CoV-2 on the everyday life of most humans has significantly subsided, the prospect of

another coronavirus with pandemic potential emerging remains a possibility[33,34], emphasizing the current and future relevance of coronavirus research.

Considering the time required for the development and approval of a totally new antiviral drug directed against SARS-CoV-2 and its subsequent variants, much effort was directed towards identifying potential drug candidates. Of particular interest were drugs that were already approved for treatment of other diseases by influential pharmaceutical regulators such as the Food and Drug Administration (FDA) of the United States or the European Medicines Agency (EMA) of the European Union, as they would not have to undergo all three clinical trial stages. Instead, only clinical trials would be needed to show efficacy against SARS-CoV-2, potentially saving not only money and time, but most importantly human lives. Before approval of effective vaccines or novel drugs against SARS-CoV-2, early results from such repurposing studies observed antiviral effects of multiple members of the cationic amphiphilic (CAD) drug family[35–37].

The chemical structure of CADs consists of a hydrophobic part and at least one primary or substituted nitrogen group, which provides weak basic properties[38]. While unprotonated, CADs may cross lipid membranes due to their hydrophobicity. In acidic environments such as lysosomes, the molecule will become cationic through protonation and thus unable to leave the lysosome. The resulting lysosomal accumulation of such compounds is known as lysosomotropy. Members of the CAD family include (hydroxy)chloroquine, fluvoxamine, fluoxetine and imipramine[38], which have been reported to exert antiviral activity against SARS-CoV-2 and other viruses *in vitro*[35–37]. While one of the most prominent members of this drug class, chloroquine, and its less toxic sister drug hydroxychloroquine failed publicly in clinical trials against SARS-CoV-2[39–49], another CAD member, fluvoxamine, showed positive results against COVID-19 in clinical settings[50] and clinical trials[51,52]. Regulatory institutions such as the World Health Organization (WHO) and the National Institute of Health (NIH) criticized lack of direct evidence for a mechanism of action against COVID-19[53,54]. While the use of fluvoxamine in the treatment of COVID-19 is only recommended in the context of clinical studies[54] and more effective drugs have since been developed, the inhibition of viral infection by several CAD family members *in vitro* raises interesting questions in basic cell biology and virology and therefore merits further study.

1.5. Aim of Study

The **first goal** of this thesis was to study the cellular remodeling caused by infection with viruses such as SARS-CoV-2 and the feline peritonitis virus (FIPV) at early time points, as well as potential mechanisms of action of FDA-approved antidepressant drugs, which have been shown to exert antiviral activity against SARS-CoV-2. To that end, cryo-soft X-ray tomography (cryo-SXT) was used, which enables visualization of the cellular 3D-ultrastructure at high resolution under near-native conditions. Since cryo-SXT only relies on the intrinsic chemical contrast of samples, it can serve as a powerful tool to uncover unexpected changes in cells, which is crucial when investigating a novel virus such as SARS-CoV-2. This work is presented in **chapter 2**.

While cryo-SXT has significant strengths in accurately visualizing cellular ultrastructure, access to the instrumentation is highly centralized at a small number of synchrotron facilities worldwide. Continuous efforts in the field have been undertaken to improve and automate the technology at the beamline and to train and advise users in experimental design, sample preparation, and data analysis. However, in order to make use of these advancements, users are still dependent on the synchrotron facilities. Hence, the **second goal** of this work was to make cryo-SXT more efficient and accessible for users independently of synchrotron facilities. This goal was addressed from two sides: *A priori* characterization of samples by expansion microscopy and automated image segmentation by deep learning.

Despite all the technological progress in cryo-SXT, the overall throughput is very limited, meaning that researchers require as much *a priori* information about their biological system and experimental conditions as possible before using their limited beamtime. The novel technique of expansion microscopy can address this limitation and shows great promise for cellular ultrastructure characterization. However, the extensive sample processing raises questions on the quality of ultrastructural preservation, which can be addressed by cryo-SXT. On the other hand, ExM is a highly accessible technique, which enables ultrastructural screenings with conventional, commonly accessible fluorescence microscopes. The complementary use of cryo-SXT and ExM is explored in **chapter 3**.

Besides the limited access to cryo-TXMs, the analysis of cryo-SXT data is a major bottleneck in the field. In particular, image segmentation is an important but extremely time-consuming process. With the onset of artificial intelligence, this problem in image analysis is being actively researched across the fields of EM, FM and cryo-SXT to reduce the time and effort users have to spend to obtain quantifiable information from their data. A plethora of deep learning tools have emerged for fluorescence and EM segmentation, but for X-ray microscopy, deep learning is challenging

because of scarcity of high-quality training data. The **third goa**l of this work was to tackle this challenge and to provide a platform for fully automated, on-the-fly segmentation of cryo-SXT data. This enables users to segment their data quickly already while on the beamline, saving weeks otherwise required for segmentation of a single dataset. This deep learning platform was developed and published in collaboration with Dr. Mohsen Sadeghi and Dr. Frank Noé and is described in **chapter 4**.

2. Studying Coronavirus Infection with cryo-Soft X-ray Tomography

2.1. Abstract

Cryo-soft X-ray tomography (cryo-SXT) enables high-resolution visualization of the 3D-ultrastructure of whole cells in their near-native state. The technique exploits the high intrinsic contrast of carbon-dense structures such as lipid membranes in the spectrum of soft X-rays, as well as the principles of sample vitrification and tomography. This technique poses a powerful tool to visualize and uncover ultrastructural alterations of cells in response to environmental factors, such as viral infection, without requiring extensive *a priori* knowledge as to what alterations to expect and look for. This is particularly relevant when studying novel emerging viruses, such as SARS-CoV-2 during the COVID-19 pandemic, when such *a priori* knowledge was scarce. In this work, the infection of cultured cells with the feline coronavirus or SARS-CoV-2 were predominantly investigated by means of cryo-SXT. By using this technique, binding of feline coronavirus particles to the filopodia of CRFK cells was observed within only few minutes of virus addition. While such clear binding was not observed in the case of SARS-CoV-2, a striking number of multilamellar bodies formed in cultured Vero E6 cells within few minutes of infection. Such organelles were also observed in Vero E6 cells treated with fluvoxamine and in CRFK cells treated with imipramine or fluoxetine in presence and absence of feline coronavirus. These three drugs are FDA-approved members of the family of cationic amphiphilic drugs and have been shown to exert antiviral activity against either feline coronavirus in our work or against SARS-CoV-2 in previously published work. Due to the limited access to cryo-SXT and insufficient fluorescent labeling of the viruses, it was not possible to conclusively elucidate antiviral mechanisms of action exerted by the drugs. However, the observed alterations in size and number of dark-rimmed vesicles in drug-treated cells in presence versus absence of virus in both model systems suggests two possible modes of inhibition. The first proposed mode is inhibition of lysosomal escape by drug-mediated elevation of lysosomal pH, leading to impairment of the pH-sensitive activity of the enzymes that mediate the second proteolytic priming event of coronavirus spike proteins for viral fusion with the lysosomal membrane. The second mode of inhibition is a systemic dysregulation of lipid metabolism, which interferes with multiple stages of the viral replication cycle that relies extensively on the host cell membrane system, including formation of membranous replication organelles and viral assembly. Testing these two not mutually exclusive models with additional experiments will not only further clarify the mechanism of action of the drugs against coronavirus infection but will also advance our understanding of fundamental cell biology.

2.2. Introduction: Studying Cellular Ultrastructure with Microscopy

Microscopy techniques of various forms have become central tools for the study of the structure-function relationship in cell biology. The two most prominent examples are fluorescence microscopy (FM) and electron microscopy (EM). Besides these two widely employed groups of microscopy techniques, a third, lesser-known technique called cryo-soft X-ray tomography (cryo-SXT) has been established. Unlike conventional EM or FM techniques, cryo-SXT relies on intrinsic absorption properties of the sample, such that no staining or fixation procedures are required to generate contrast. Furthermore, it allows the volumetric analysis of cellular ultrastructure under near-native conditions at 25 – 40 nm resolution of a 10 – 15 x 10 – 15 µm large field of view within less than half an hour of acquisition time[55–57]. These benefits make cryo-SXT a powerful tool for the investigation of cellular architecture and alterations induced by, for instance, viral infections.

Before describing the principle of cryo-SXT in more detail in the next section, the use of this technique shall be briefly contextualized among the more commonly used EM and FM techniques to highlight the relevance of cryo-SXT for biological research. Key points of the different techniques are summarized in table 1-1 below.

Conventional FM uses fluorescent proteins or dyes that specifically highlight structures or molecules of interest. The most significant benefits of FM-techniques are: (1) an extensive toolset of fluorescent markers to visualize specific structures or molecules of interest with (2) high contrast, (3) rapid acquisition times. It provides access to (4) temporal resolution and (5) relatively large and complex specimens such as tissues or whole organisms. However, there are some important drawbacks as well: Firstly, the attainable resolution of structural information is limited by the diffraction properties of light, unless more advanced tools such as super-resolution microscopy techniques or expansion microscopy are employed (see also chapter 3). Secondly, the basic principle of FM depends on the use of specific fluorescent labels that need to be somehow introduced into the sample during the experiment. Therefore, the information obtained by any FM experiment depends on the *a priori* hypotheses, based on which fluorescent labels were selected. An experiment designed to visualize, for example, ER morphology under overexpression of a given protein of interest can easily miss other structural alterations occurring in the cell, unless the affected structures were serendipitously labeled with fluorescent markers too.

EM techniques have been the gold standard for microscopic analysis of cellular ultrastructure at the nanoscale for decades. While many different variants have been developed in the past decades, the central benefit of EM is its unmatched resolution. Depending on the specific

approach, it can serve to resolve single particles at atomic resolution (single-particle analysis), or the cellular ultrastructure of a thin slice of the specimen's volume, independently of markers for specific structures. These important qualities notwithstanding, there are also important drawbacks of EM-based techniques: (1) The inelastic scattering of electrons limits the thickness of the specimen that can be imaged at a time. Traditionally, covering the volume of biological specimen by conventional transmission EM required fixation, resin-embedding, sectioning, and serial acquisition of countless sections, which is extremely time-consuming and prone to introduction of various kinds of artifacts[58–62]. The introduction of technologies such as vitrification[63,64] and focused ion-beam (FIB) techniques[65–69], has made volumetric scanning electron microscopy imaging much more efficient, but it still often relies on resin-embedding and heavy metal staining[70,71] and even with FIB SEM, acquisitions of a cellular volume still require several hours or days, depending on the resolution and acquired volume[72,73].

Cryo-SXT bridges the gap between fluorescence and electron microscopy. Compared to fluorescence microscopy, it offers intrinsically higher resolution and overall cellular context, independently of specific fluorescent markers. As will be shown in the results in this section, cryo-SXT can visualize even unexpected cellular changes at high resolution in absence of a fluorescent label. Compared to EM, cryo-SXT can acquire a large volume within only a short acquisition time, while at the same time not requiring fixation or staining with heavy metals. The following section explains further how this is possible.

Table 1-1: Overview of Important Microscopy Techniques Used in Biology. This table is based on Fitzpatrick et al., 2020[74], unless otherwise cited. Note that the values may vary, depending on the specific application or variation of the microscopy technique. STA = sub-tomogram averaging.

TECHNIQUE	RESOLUTION	IMAGING DEPTH	IMAGING TIME	FIXATION	REQUIRED STAIN	TEMPORAL IMAGING
CONFOCAL MICROSCOPY	~ 200 nm	tens of µm[75]	minutes	chemical, none	fluorescent dyes	possible
SUPER-RESOLUTION MICROSCOPY	~ 20 nm	usually < 10 µm[75]	minutes	chemical, none	fluorescent dyes	possible
TEM	> 1 nm[76,77]	tens of nm[78]	minutes	chemical, vitrification	heavy metals	impossible
CRYO-ET	~ 0.3 nm (STA)[79,80] ~ 5 nm[81,82]	few hundreds of nm[83–85]	hours (STA)[86] minutes[86]	vitrification	none	impossible
FIB SEM	~ 5 nm	tens of µm[72,87]	hours	chemical	heavy metals	impossible
CRYO-FIB SEM	~ 5 nm	tens of µm[88,89]	hours	vitrification	none	impossible
CRYO-SXT	25 - 40 nm	< 15 µm[90]	minutes	vitrification	none	impossible

2.3. The Principle of cryo-Soft X-ray Tomography

The basic principle of cryo-SXT is to exploit the intrinsic absorption properties of the samples under the soft X-ray wavelengths used and to visualize the original 3D structure at 25 – 40 nm resolution[56,91,92] by means of tomographic reconstruction.

The term “soft” in “soft X-ray microscopy” refers to a spectral region of 0.1 – 10 nm wavelength. The key peculiarity of soft X-rays in the context of biological research lies in a spectral range called the “water window” (fig. 2-1), which lies between the carbon K edge at 284 eV and the oxygen K edge at 543 eV photon energy (4.37 – 2.28 nm wavelength). Wavelengths in this range are only slightly absorbed by oxygen and hydrogen atoms, while carbon and nitrogen atoms show very strong absorption. Carbon-dense structures in a biological specimen, such as lipid bilayers or dense protein structures absorb very strongly, while more aqueous parts of the specimen, such as the cytoplasm, appear more transparent. As a result, the intrinsic chemical composition of the sample can be used to acquire a label-free absorption contrast in a transmission soft X-ray microscope[91–93].

Vitrification is a method that allows practically immediate cryo-fixation of a sample in its near-native state by freezing the specimen quickly enough to prevent formation of crystalline ice which would distort the original structures[63,94]. It has become the gold standard in structure preservation and allowed development of cryogenic techniques, including cryo-EM and cryo-SXT. While there are several techniques for vitrification, plunge-freezing has become the dominant method in cryo-SXT, effectively vitrifying thin samples such as cell monolayers[55,91]. The basic idea for plunge-freezing is to have the specimen mounted onto the carbon foil on gold TEM grids, then blotting excess liquid away through the holes in the carbon film before finally dipping the entire specimen into liquid ethane for vitrification[63]. This technique can be performed either manually or using an automated, humidity-controlled device for more reproducible results[55,95].

Once vitrified, the sample is mounted on a sample holder and inserted into the light path of the transmission X-ray microscope. A schematic is shown in figure 2-1 A. The sample is illuminated with soft X-rays via an elliptically shaped mirror ("capillary") and a nano-fabricated Fresnel zone plate objective projects the magnified image of the specimen onto the camera. The two-dimensional projection image captured by the camera is composed, in approximation, of line integrals of the local absorption contrast across the specimen's volume. By acquiring a series of such 2D projection images at known tilt angles, the original, three-dimensional distribution of local absorption contrast can be calculated, which essentially reveals the original structure of the specimen (fig. 2-1 B). This procedure is known as tomographic reconstruction and allows volumetric analysis of the specimen's ultrastructure.

For correct interpretation of cryo-SXT datasets, it is important to be aware of two phenomena that play a role in the formation of the final 3D image.

Missing wedge artifact: The missing wedge artifact arises in tomographic reconstructions, when the image data do not cover the full ± 90° tilt range. The 'wedge' describes the shape of missing information, i.e. the missing high tilt images, in Fourier space (see fig. 2-1 C). In the data, this artifact is noticeable as missing information on the top and bottom of reconstructed objects, as well as elongation of objects in the Z direction (fig. 2-1 C). One reason for the incomplete rotation is the increased path length of the X-ray beam through the sample at high tilts and a second reason is possible physical collision of a highly tilted sample holder with the zone plate objective in the X-ray microscope. As a result, the typical tilt range covered by cryo-SXT on flat supports is ± 60 - 70° [91,92]. This problem can be addressed, for instance, by acquiring a second tilt series for the same field of view with a second tilt axis. This reduces the missing wedge artifact to a missing

pyramid[96,97] (see fig. 2-1 C). Alternatively, samples can be mounted and vitrified in thin capillaries, which allow full coverage of the tilt range[98,99].

Sample thickness and depth of focus: The maximum thickness of cryo-SXT specimens is approximately 15 µm. This size limitation originates from the significant increase of the path length through the sample when the sample is being tilted. The increased path length leads to reduced transmission of the beam and a lower signal-to-noise ratio of the resulting projection images. While it is thus currently not possible to image tissues, cell monolayers[90,100–106] or small single-cell organisms such as algae[107,108], yeast[98,109] or malaria parasites[110] can still be visualized in great detail.

More importantly, the optics used in the transmission X-ray microscope have a limited depth of focus. The XY resolution, as well as the depth of focus of the system are dictated by the Fresnel zone plate used. Because the numerical aperture of the X-ray microscope is with NA = 0.03 much lower than that of light microscopes, the depth of field in cryo-SXT is much higher than that of fluorescence microscopes. The lower-resolution 40 nm Fresnel zone plate objective provides a depth of focus of approximately 3.6 µm, while the higher-resolution 25 nm FZP has a depth of field of approximately 1.6 µm[111]. For cells thicker than the depth of focus, including typical mammalian cells, this leads to decreased resolution outside of the focus volume.

2.3.1. Application of cryo-SXT

Despite these limitations, cryo-SXT has found application in addressing a wide range of biological problems. For instance, it has been used to study the life cycle of yeast cells[109] and parasites[112]. Extensive efforts have been directed towards the in-depth, high-resolution study of the ultrastructure of mammalian cells under near-native conditions[56,90,100,113], as well as in interactions with viruses[101,103,114–116], bacteria[117], parasites[110] or functionalized nanoparticles[104].

Over the course of the COVID-19 pandemic, cryo-SXT was also used to characterize the cellular remodeling induced by SARS-CoV-2 in cells at late time points of infection[106,114]. In contrast, the work presented here focused on the early time points of infection with the virus, looking for early signs of cellular remodeling induced by the virus. The second goal was to identify clues for how members of the cationic amphiphilic drug family exerted the antiviral effect against coronaviruses, which had been reported from multiple *in vitro* experiments and drug repurposing studies published at the time[35–37,118,119].

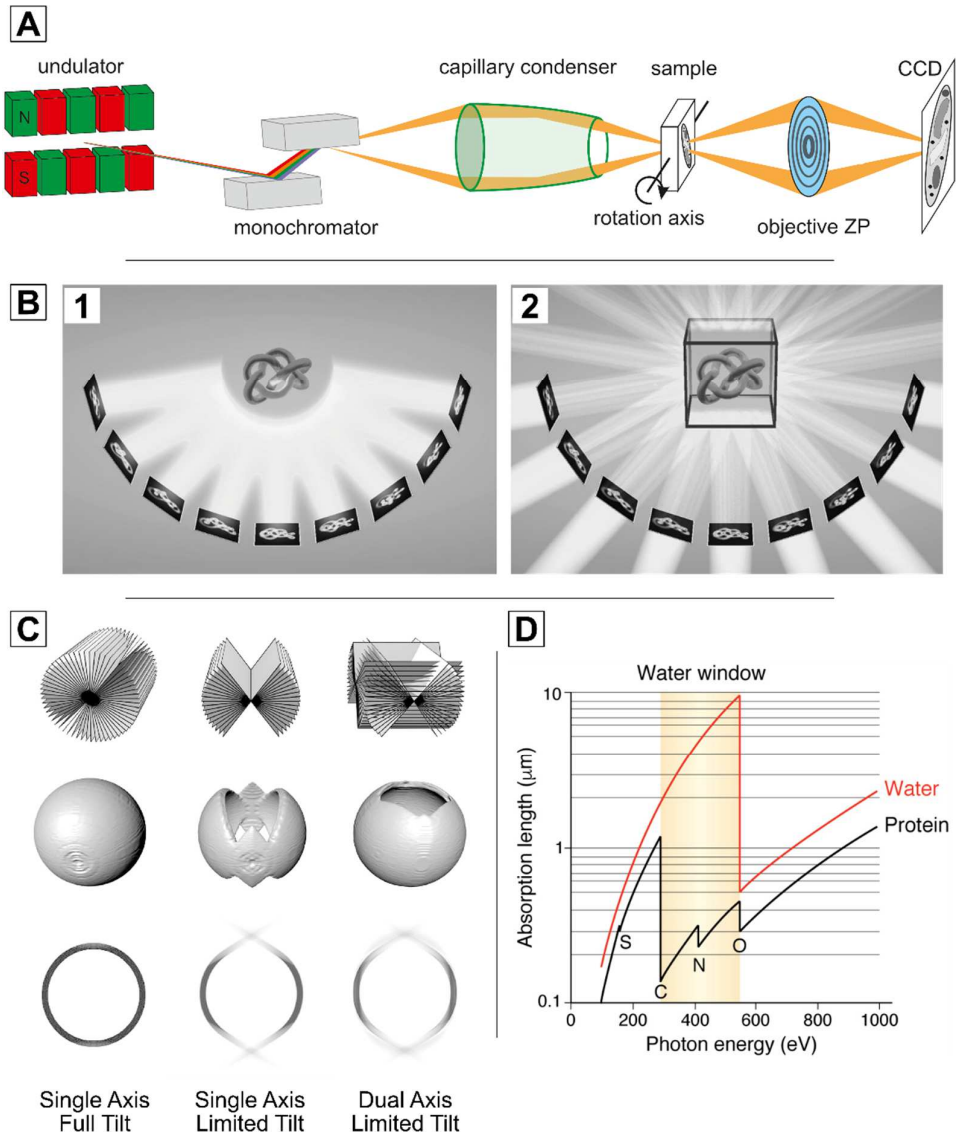

Figure 2-1: Basic Principle of cryo-Soft X-ray Tomography. A: The layout of the soft X-ray microscope at BESSY II. An undulator serves as a light source by generating X-rays. A combination of a grating and a mirror acts as monochromator. An elliptically shaped mirror ("capillary condenser") illuminates the sample mounted on a rotatable holder. An optical element called zone plate (ZP) is used as objective and relays the image onto the charge-coupled device (CCD) chip used for detection. Figure provided by Stephan Werner. **B:** The tomography principle. Images of the original structure are acquired at various angles (1). These images are then used to computationally reconstruct the original image (2). Reproduced from Baumeister et al., Trends Cell Biol. 1999[120] with permission from Elsevier. **C:** Illustration of the missing wedge phenomenon and its consequences. The first column shows the scenario of acquiring a full ± 90° tilt series with a single axis, which yields almost full reconstruction of the original thin-walled sphere. The second column illustrates the scenario of a limited tilt range, where the missing images form a missing wedge in Fourier space (top row). In tomographic reconstructions, this is noticed as missing information on the top and bottom of the sphere (middle row), as well as elongation and blurring in alongside the Z direction in YZ-slices of the tomogram (bottom row). Dual-tilt tomography can mitigate this problem to an extent. Image reproduced from Koning et al., Ann. Anat. 2018[121] under CC-BY-NC-ND license. **D:** Illustration of the water window. The plot depicts the absorption lengths of different photon energies in different media, specifically water and protein. Image reproduced from Fitzpatrick et al., J. Biol. Chem. 2020[74] under CC-BY license.

2.4. Results

2.4.1. Studying Early Timepoints of Feline Coronavirus Infection Using cryo-SXT

The very first question arising in this work was whether coronavirus particles could be directly visualized with the cryo-transmission X-ray microscope at BESSY II. This would allow effective study of early events in the infectious cycle by cryo-SXT. Already at this time, the majority of the experiments related to ultrastructural alterations caused by SARS-CoV-2 were performed at later time points of infection, while the earlier time points were rarely reported. Especially in the beginning, biosafety considerations and access to SARS-CoV-2 experiments were a major concern. Therefore, the emphasis of the first experiments in this work was on another coronavirus, the feline infectious peritonitis virus (FIPV), which served as a model system for optimization of sample preparation, handling, and cryo-SXT visualization. These experiments were undertaken in close collaboration with Dr. Chuanxiong Nie, who propagated and purified FIPV and determined stock titers. He and Dr. Susanne Kaufer from the veterinary medicine department at FU Berlin supported this work with their expertise on experimental design for virus visualization.

For the FIPV infection experiments, CRFK cells were seeded in 12-well plates with plasma-cleaned gold TEM finder grids. The cells were then placed on ice for a short period of time to slow down endocytosis. Then, purified FIPV was added to an estimated multiplicity of infection (MOI) of 20, 50, 100 or 200 virions per cell, to increase the likelihood of observing virus particles in the TXM. The cells were then kept on ice for another 10 or 15 minutes to allow binding and synchronous uptake by the cells during the actual infection period in the incubator at 37 °C.

In a first infection experiment, particles adherent to the filopodia of CRFK cells could be observed by TXM within only a few minutes of infection (fig. 2-2). Uninfected control cells never showed any such particles on their surfaces, indicating that these were indeed FIPV particles. In some instances, it was even possible to observe these particles bound to the cell surface already in the scanning mode of the microscope, prior to performing tomographic reconstruction, raising the possibility of screening the sample for virus binding events (fig. 2-2 A). However, such screening for virus-bearing cells was limited to thin structures such as filopodia that were not overlapping with more dense parts of the cells, where it would be impossible to discern viruses from the also highly absorbing background of the cells in transmission view. The formation of invaginations on the cell surface bearing particles (see fig. 2-2 v) suggested that FIPV particles were also already being internalized into the cells. However, it was difficult to clearly distinguish them from other cellular structures in the cell interior and therefore the virus uptake process into CRFK cells could not be tracked further by cryo-SXT.

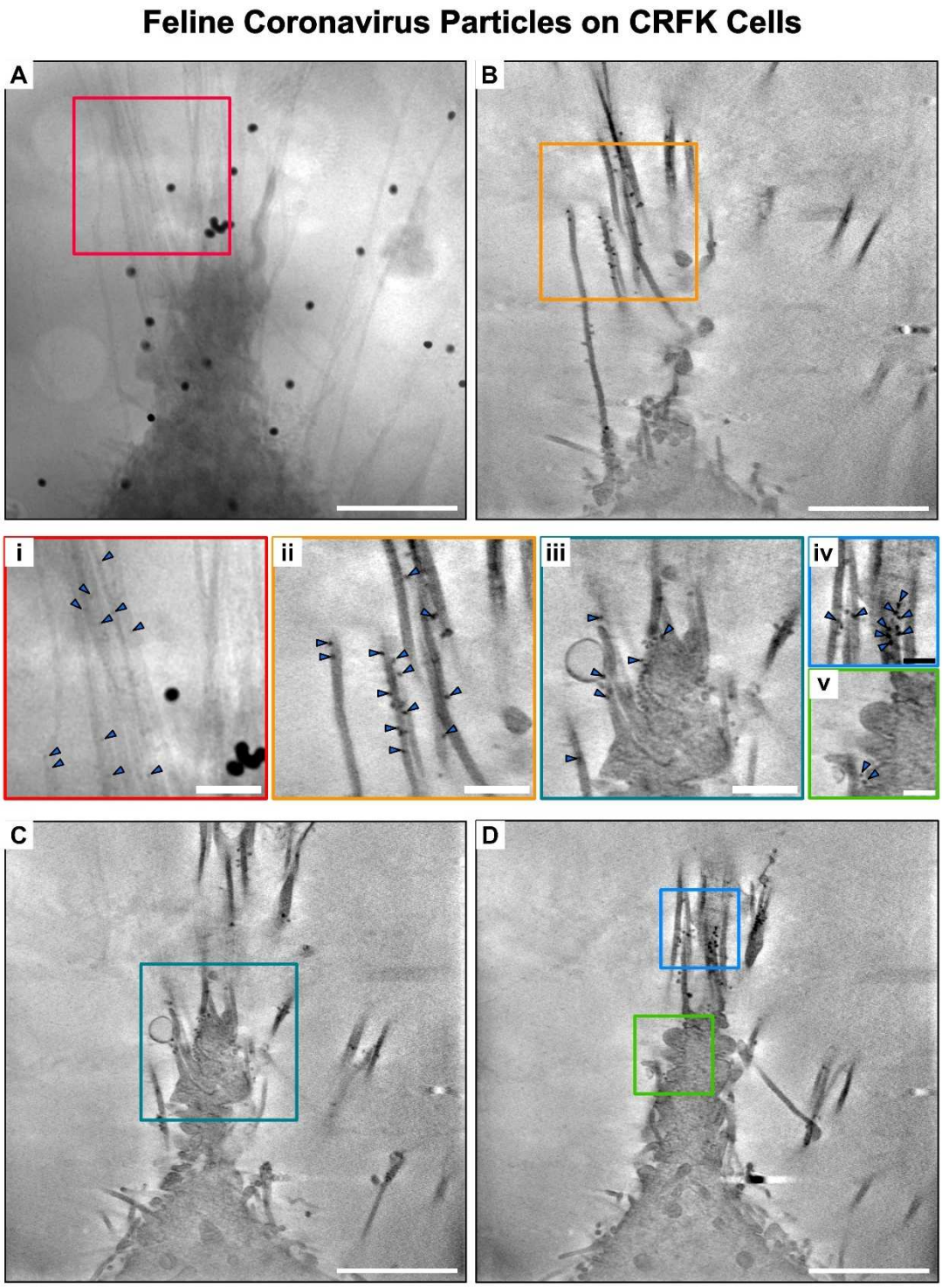

Figure 2-2: Cryo-Soft X-ray Tomography Reveals Feline Coronavirus Particles on Filopodia of a CRFK Cell after 3 Minutes of Infection. Panel A shows an X-ray transmission micrograph taken at 0° tilt angle. The box denotes the area magnified in panel i, where virus particles are highlighted by blue arrows. The image was smoothened with a 2-2 median filter for presentation. Panels B-D show parts of the tomographic reconstruction from the same FOV presented in panel A. The colored boxes denote the areas shown magnified in panels ii-v, where virus particles are highlighted by arrows. The shown tomogram slices are Z-projections of 10 consecutive slices. Scale bars: Panels A-D: 3 µm. Panels i-iii: 1 µm. Panels iv & v: 0.5 µm.

2.4.2. Effects of the Antidepressants Fluoxetine and Imipramine on FIPV Infection

Cryo-SXT is an invaluable tool to investigate ultrastructural alterations in cells and can visualize even unexpected alterations in cells under given conditions. Therefore, it is a lucrative approach to investigate the inhibition of viral replication. The observation that the feline coronavirus quickly binds to the filopodia of CRFK cells suggested that inhibition of filopodia formation could lead to a reduction in virus uptake and replication. Therefore, the next question was whether such an effect could be responsible for the antiviral effect observed in several FDA-approved drugs which were emerging from drug-repurposing screens against SARS-CoV-2 infection at the time. Two of these drugs were selected: The antidepressant drug imipramine is believed to inhibit formation of filopodia by binding to fascin-1 at a concentration of 10 µM[122]. Also, it is known to inhibit macropinocytosis[123], which is a possible virus entry mechanism[124–127] and has been suggested to play a role in SARS-CoV-2 infection[128]. Furthermore, imipramine inhibits replication of several viruses, including CHIKV, WNV and DENV[129]. Another, structurally related drug called fluoxetine emerged early on as a promising candidate from drug-repurposing screenings against SARS-CoV-2[35–37,119].

The first necessary step to investigate the mechanism of action of imipramine and fluoxetine against viral replication is to determine the appropriate dosage and confirm their activity in the model system. Our own preliminary tests in CRFK cells did not show cytotoxic effects in the low micromolar range of either imipramine or fluoxetine upon treatment for periods longer than 48 hours, in accordance with drug-repurposing studies against SARS-CoV-2 published at the time using the same drugs[35–37,118]. Thus, Mr. Chuanxiong Nie tested for antiviral effect of fluoxetine and imipramine by plaque assay under various conditions (fig. 2-3). Across all three experimental conditions tested, his results showed that both imipramine and fluoxetine inhibited replication of FIPV in CRFK cells when 10 µM of either drug was present. Of the two drugs, 10 µM fluoxetine treatment showed a consistently stronger reduction of viral titer compared to untreated controls with 97-fold reduction or 407-fold reduction for 12 hours or 24 hours post-infection treatment, respectively, compared to 15-fold and 71-fold reduction for 10 µM imipramine.

These results suggest that treatment of cells with 10 µM of either drug for 24 hours is sufficient to effectively inhibit FIPV replication in CRFK cells and therefore this condition was used as standard treatment for the following experiments.

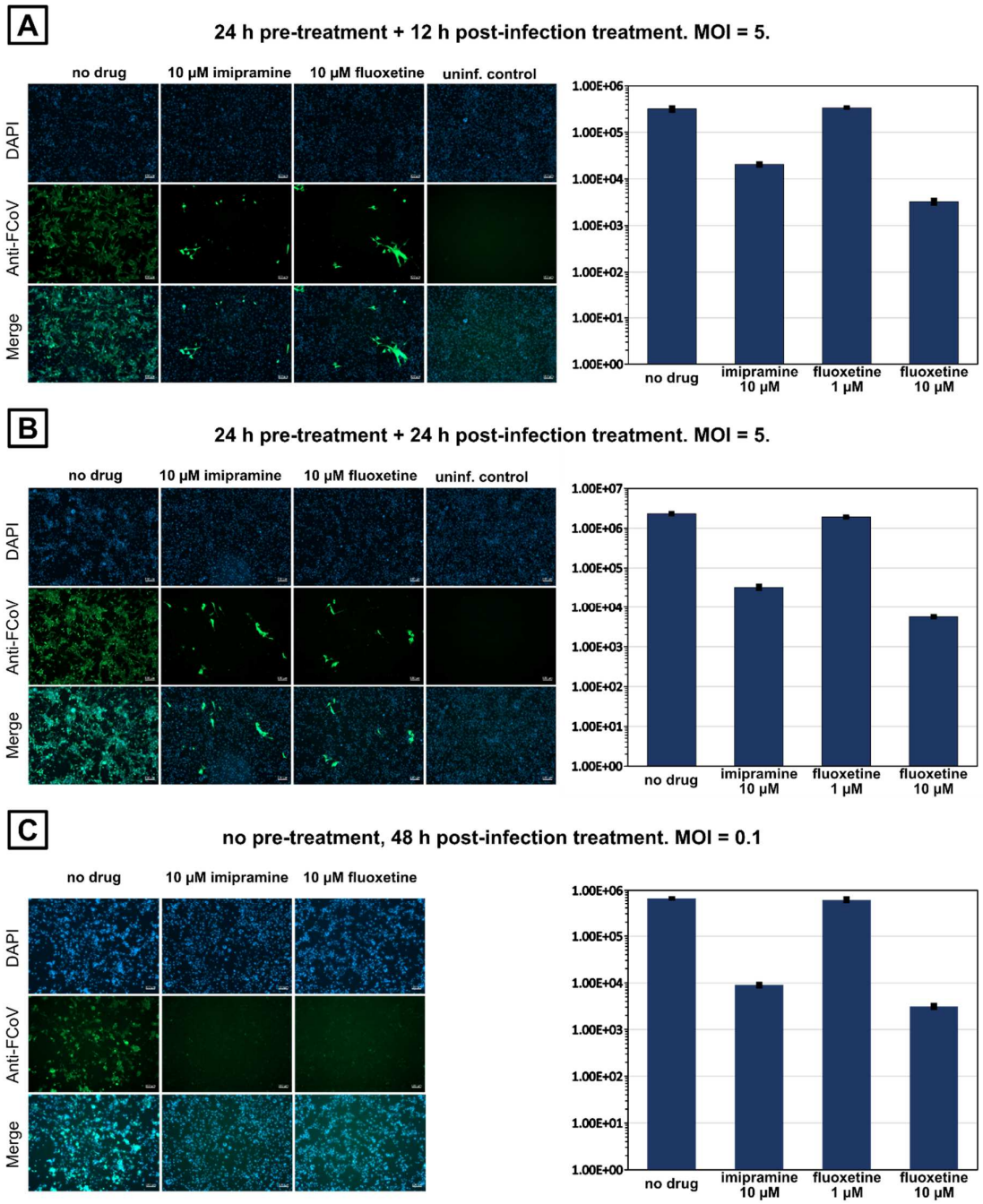

Figure 2-3: Plaque Assay Shows Antiviral Effect of Antidepressant Drugs Imipramine and Fluoxetine Against Infection with FIPV. A, B: Cells were pre-treated for 24 h with drug in the given concentration and subsequently incubated with FIPV for 1 h with an MOI of 5 and then cultured for another 12 h (A) or 24 h in presence of drug before quantitation by plaque assay. C: Untreated cells were infected for 1 h with an MOI of 0.1 and then cultivated for 48 h in presence of drug in given concentrations. The error bars denote the standard deviation between the two technical replicates used for each measurement. n=1. Scale bar: 100 µm.

The first hypothesis for the antiviral mechanism of the drugs by impairment of virus attachment to the cell surface of filopodia was difficult to test comprehensively at early time points, since only few instances of infected control cells could be found with clear virus attachment. However, the unexpected observation of formation of a striking number of dark-rimmed vesicles (DRVs) in drug-treated infected and uninfected cells (fig. 2-4, red arrows) suggested a mechanism of action not mediated by filopodia. These DRVs were only rarely observed in our cryo-SXT data of untreated cells. They consistently occurred clustered in association with organelles with a comparatively high soft X-ray absorption, which resembled late endosomes/lysosomes shown in work by McNally et al.[90] and are clearly distinct from early endosomes and autophagosomes identified by CLXM by Collinson et al.[102]. This suggested that the DRVs are associated with late endosomes/lysosomes. Besides the DRVs, large whorls with clearly discernible membrane layers could occasionally be observed (see fig. 2-4, purple arrows in panels iv, vii and ix) in infected and uninfected cells, as well as highly absorbing, more linear structures, that also seemed to be multilamellar figures (yellow arrows in fig. 2-4, panels i, ii, v, vi). While it is possible that the linear membrane figures, DRVs and whorls are different stages of the formation of the same structure, no clear intermediate stages between these objects could be observed.

Analysis of the number of DRVs showed a baseline presence in untreated, uninfected CRFK cells (fig. 2-5). The average number of DRVs per cell remained relatively constant in untreated control cells versus cells infected with a multiplicity of infection (MOI) of 200 of FIPV for 3 minutes. Infection with an MOI of 100 for 5 minutes increased the average number from 3.1 – 7.7 DRVs per cell to 13.3 per cell. This number doubled, when cells were pre-treated with 10 µM fluoxetine for 24 hours prior to infection with an MOI of 20 for 3 minutes, and sextupled when drug-treated cells were infected with an MOI of 50 for the same period. In absence of virus after 24 hours drug-treatment, the average DRV number increased 20-fold to 158.6 DRVs per cell in comparison to controls. Thus, it appears that treatment with 10 µM fluoxetine induces formation of a large number of DRVs, which is rapidly reduced upon infection with FIPV for only a few minutes and that infection with FIPV alone also leads to an increase in the number of DRVs per cell.

Not only did the average number of DRVs change, but also their size, as shown by analysis of manually segmented DRVs (fig. 2-5). In absence of virus, control and drug-only cells showed a relatively constant median DRV diameter of 310 – 342 nm, which did not change significantly upon very short infection with virus for 30 seconds. However, when the cells were infected with an MOI of 200 for 3 minutes or an MOI of 100 for 5 minutes, the median DRV diameter increased to 413 nm or 386 nm, respectively. In drug-treated, infected cells, the median DRV diameter

increased by approximately half to 474 – 485 nm in comparison to controls. The increased diameter of the DRVs was also reflected in an increased volume (fig. 2-6). The median DRV volume in fluoxetine-treated, infected cells was more than four-fold higher than those in the untreated, uninfected cells and more than three times larger than the median volume of drug-only cells (fig. 2-6).

The strikingly rapid reaction of the size and quantity of these DRVs raised the possibility of a direct or indirect mechanism of interference with viral replication already at an early stage of infection. However, as explained above, unambiguously locating virus particles inside the cells in cryo-SXT is very difficult this close to the resolution limit of 30 – 40 nm. Therefore, we collaborated with Kunio Nagashima from the National Institute of Health in the United States, who supported this work with his extensive experience with electron microscopy. Cells were prepared according to his instructions and sent to him for sample processing and imaging by TEM.

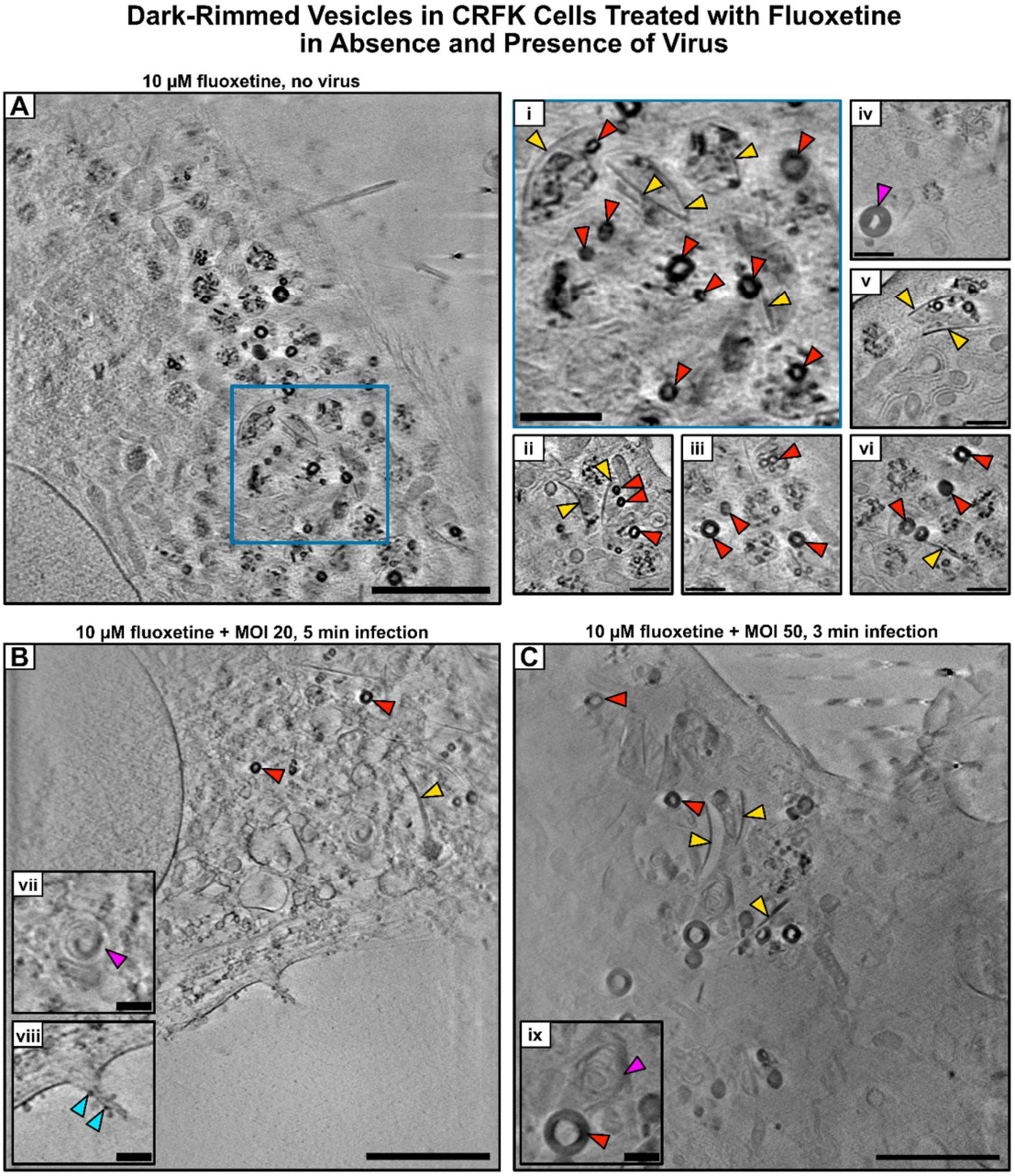

Figure 2-4: Formation of Dark-Rimmed Vesicles in CRFK Cells in Presence or Absence of Feline Coronavirus after 24 Hours of Fluoxetine Treatment. Panel A: Tomogram of a CRFK cell treated for 24 hours with 10 µM fluoxetine, then fixed with 2 % glutaraldehyde. Scale bar 3 µm. Panel i: taken from the large panel, highlighting dark-rimmed vesicles (red arrows) and linear figures (yellow arrows). Panels ii-vi are from other tomograms from other fluoxetine-treated uninfected cells. Panels B, C: Tomogram of fluoxetine treated CRFK cells infected for 5 minutes with an MOI of 20 (B) or 3 minutes with an MOI of 50 (C). Clearly multilamellar features (whorls) are highlighted with purple arrows. Blue arrows highlight particles binding to the plasma membrane. Shown are representative minimum Z-projections of 10 consecutive tomographic slices. Scale bars for panels A-C: 3 µm, panels i-vi 1 µm, vii-ix: 0.5 µm.

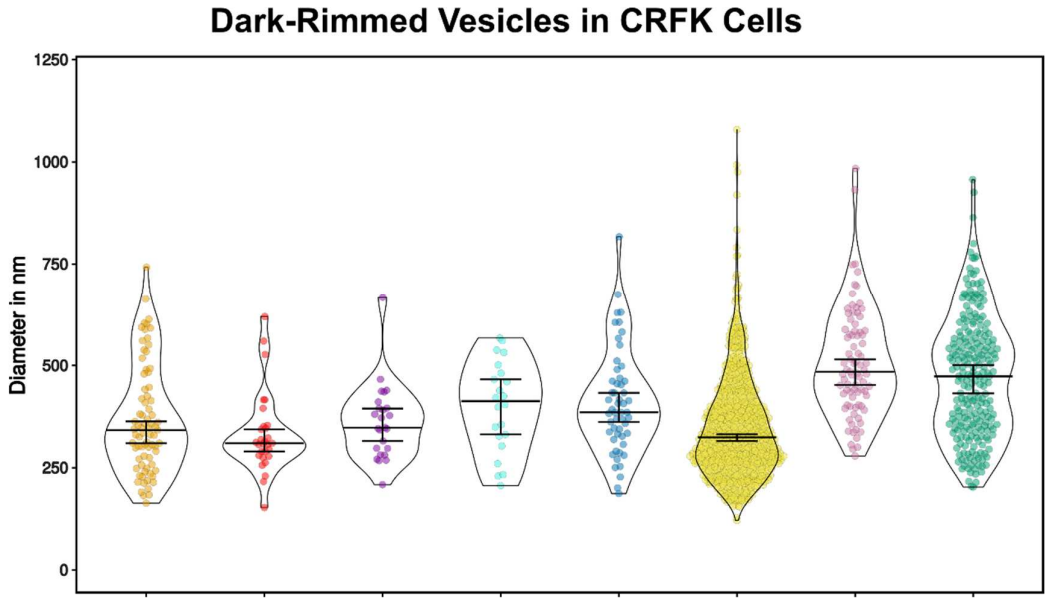

	Ctrl no ice unfixed	Ctrl 1'+10' ice fixed	MOI 20 30 s 1'+10' ice fixed	MOI 200 3 min 15'+15' ice fixed	MOI 100 5 min 15'+15' ice fixed	Fluoxetine Ctrl 1'+10' ice fixed	Fluoxetine MOI 20 3 min 1'+10' ice fixed	Fluoxetine MOI 50 3 min 1'+10' ice fixed
Average DRVs/cell	**7.7** (77 in 10)	**3.2** (29 in 9)	**5.0** (25 in 5)	**3.1** (22 in 7)	**13.3** (53 in 4)	**158.6** (793 in 5)	**27.7** (83 in 3)	**78.7** (236 in 3)
Median DRV size	**342 nm**	**310 nm**	**348 nm**	**413 nm**	**386 nm**	**325 nm**	**485 nm**	**474 nm**

Figure 2-5: Size Distribution of DRVs in CRFK Cells in Presence and Absence of Virus and Fluoxetine. The violin plots indicate the major axis length as determined by manual segmentation in Microscopy Image Browser, with each dot representing a single vesicle. The horizontal bar indicates the median and the error bars the 95 % confidence interval. The plot was created using Plots of Data[130].

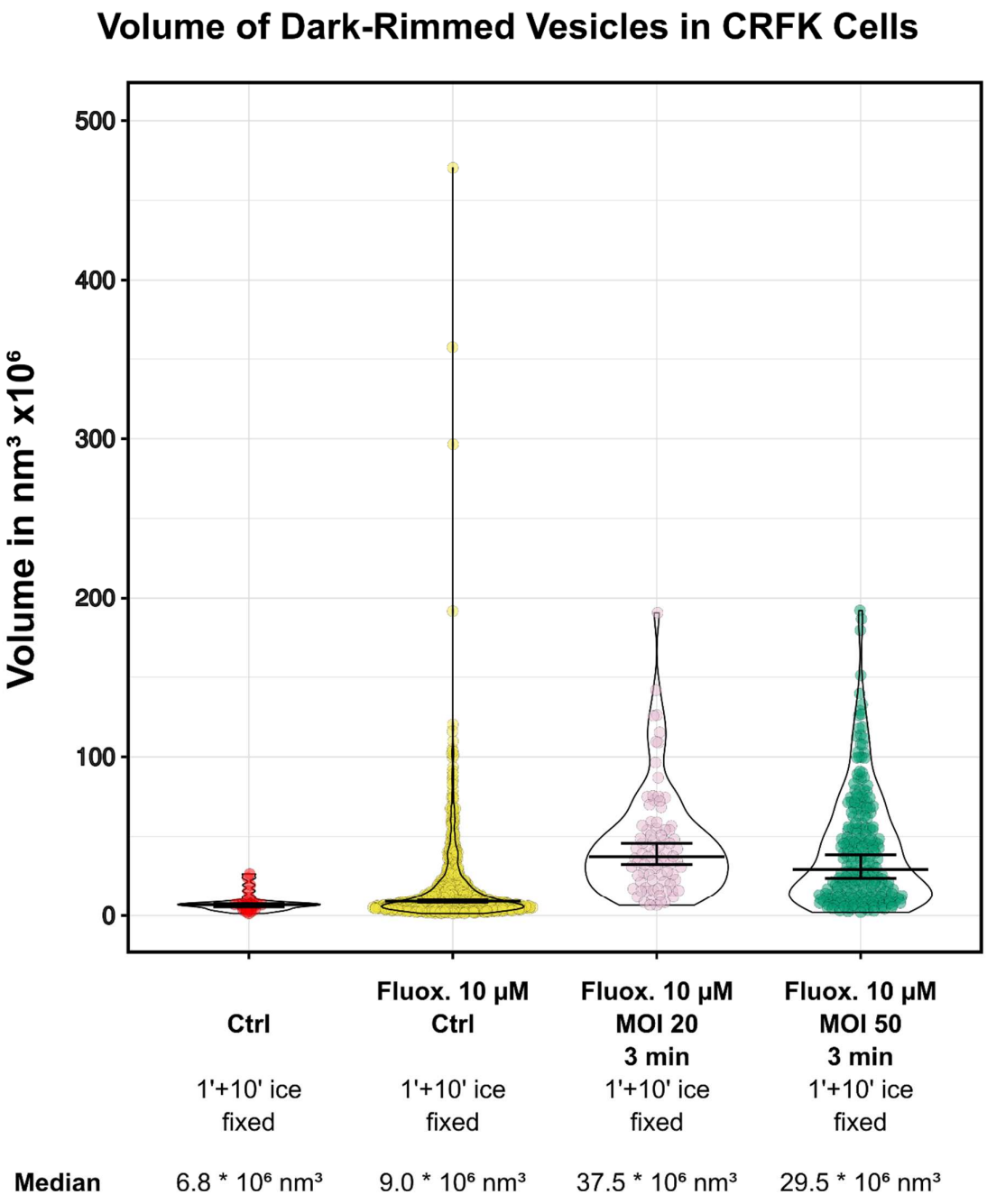

Figure 2-6: Comparison of Volumes of DRVs in CRFK Cells in Presence or Absence of Feline Coronavirus and Fluoxetine. The violin plots show the distributions of volumes of the dark-rimmed vesicles under the indicated conditions. The horizontal bar indicates the median and the error bars the 95 % confidence interval. Each dot represents one manually segmented dark-rimmed vesicle. For calculation of the volumes, an isotropic voxel with 9.8 nm side lengths was assumed. The depicted populations correspond to the ones shown in fig. 2-5 with the same colors. The plot was created using Plots of Data[130].

There were two main questions of this TEM experiment: The first question related to the nature of these dark-rimmed vesicles. The high absorption contrast of these vesicles and the thickness of the dark rim suggested several layers of membrane being stacked on top of each other. This hypothesis was supported by the presence of whorl-like structures in some instances of drug-treated cells in presence and absence of virus (purple arrows, fig. 2-4 vii, ix), but there was no further evidence from our cryo-SXT data to support this. Resolving the finer structure could elucidate how these DRVs are formed and how their structure and formation relate to the antiviral effect observed in the plaque assay. The second question was whether viral particles could be identified inside the cells and potentially in association with the DRVs. This could allow further conclusions on the antiviral mechanism of the drugs such as, for instance, trapping of the virus inside the DRVs or lysosomes.

Representative electron micrographs of the different conditions are presented in fig. 2-7 (untreated, infected), fig. 2-8 (fluoxetine-only), fig. 2-9 (fluoxetine-treated, infected) and fig. 2-11 (imipramine-only).

The electron micrographs of drug-treated cells clearly confirmed the presence of multilamellar structures associated with endolysosomes in drug-only and drug-treated and infected cells (red arrows in figs. 2-8 and 2-9). Such multilamellar structures would correspond to doughnut-shaped dark-rimmed structures observed in the cryo-SXT data. Furthermore, several TEM micrographs contained linear membrane features that consisted of one or more layers of membrane (yellow arrows in fig. 2-9 C and fig. 2-11 B1). Occasionally, linear electron-light regions were observed (purple arrows in figs. 2-7 B1, 2-8 A1, and 2-9 A1), which were often adjacent to electron-light vesicles. Equivalent, hardly absorbing features were never observed in cryo-SXT, where the samples only needed to be chemically fixed and vitrified. This suggests that these are imprints of multilamellar structures or cholesterol crystals[131,132] that were not preserved during TEM sample preparation. Taken together, our observations in TEM confirmed that the DRVs consist of endolysosome-associated, multilamellar membrane structures.

Unfortunately, it was difficult to unambiguously identify FIPV particles in any of the TEM sections. While there were many structures in the size range of coronavirus particles of 80 - 120 nm[4], only one instance of round particles with a proteinaceous corona was observed (blue arrows in fig. 2-9 D), which was in an early endosome of an infected fluoxetine-treated cell. Due to their scarcity, the identity of these particles as FIPV virions could not be confirmed with certainty. Since FIPV virions could not be found in association with lysosomes, DRVs, or anywhere else in the cells, the hypothesis of lysosomal entrapment upon drug-treatment could not be confirmed.

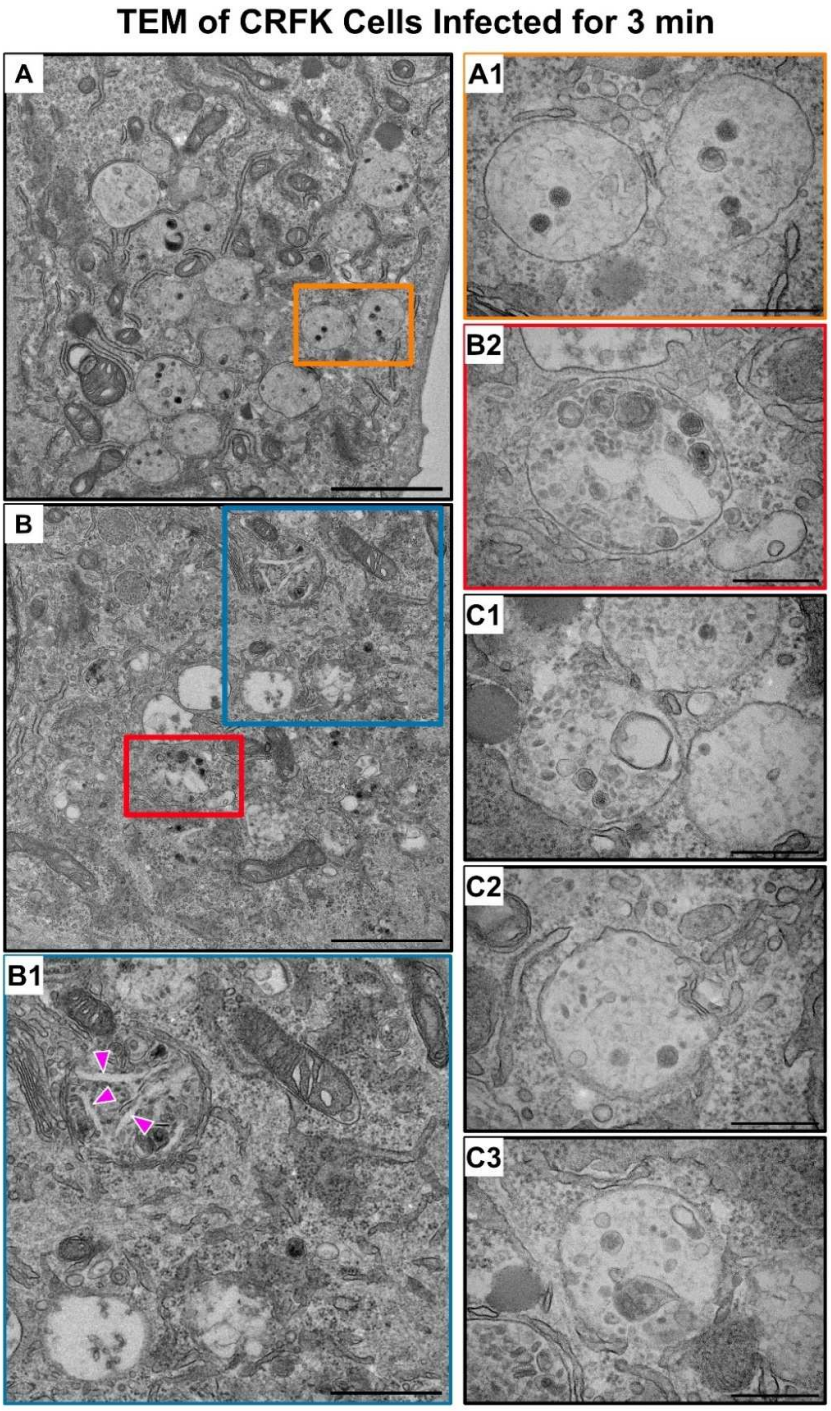

Figure 2-7: TEM Micrographs of CRFK Cells Infected with FIPV for 3 Minutes with an MOI of 50. Panels A and B show representative ultrathin slices. Panels A1, A2 and B1 are magnified displays of the areas indicated by the colored boxes in panels A and B. Panels C1-C3 are from other micrographs of the same specimen. The purple arrows in panel B1 indicate areas resembling the appearance of linear myelin figures. Scale bars: A, B: 2 µm. B1: 1 µm. All others: 500 nm.

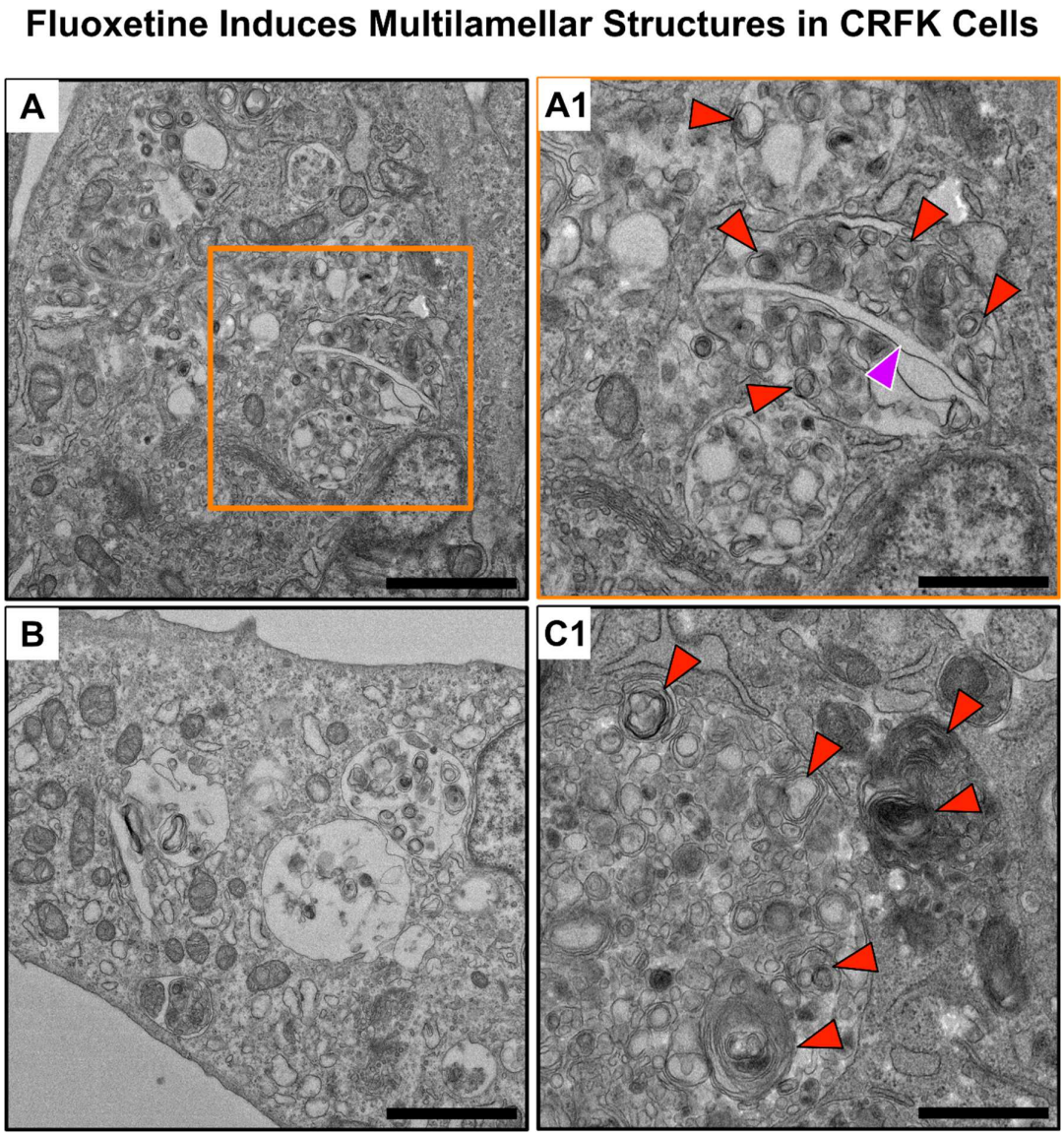

Figure 2-8: TEM Micrographs of CRFK Cells Treated with 10 µM Fluoxetine for 24 hours. Red arrows highlight multilamellar bodies. Purple arrows denote regions where multilamellar structures appear to have been lost during sample preparation. Scale bars: A, B: 2 µm. A1, C1: 1 µm

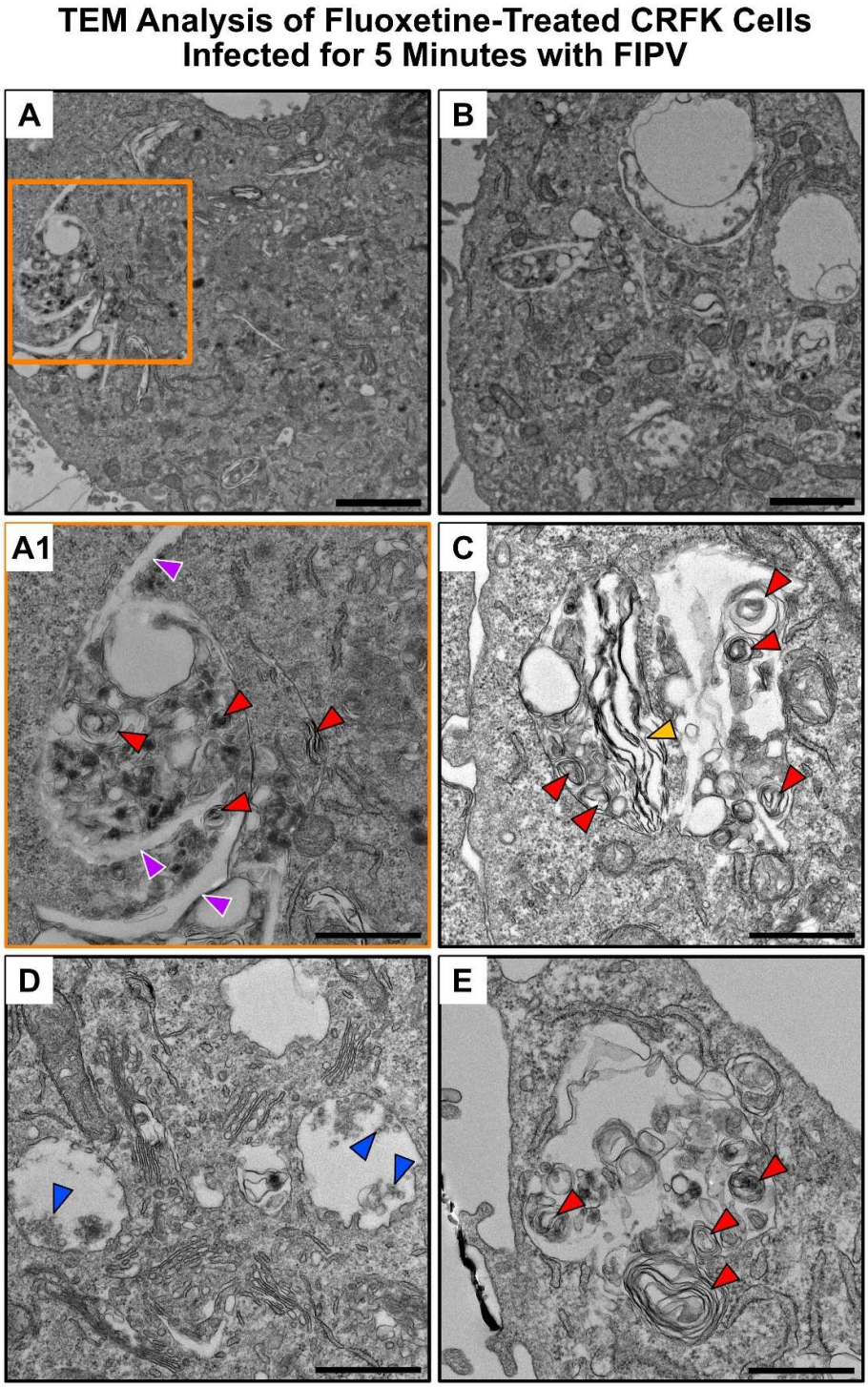

Figure 2-9: TEM Micrographs of CRFK Cells Treated with 10 µM Fluoxetine for 24 Hours prior to Infection with FIPV for 5 Minutes with an MOI of 50. Red arrows highlight multilamellar bodies. The yellow arrow highlights a multilamellar linear feature. Purple arrows denote regions where multilamellar structures appear to have been lost during sample preparation. Blue arrows indicate small particles inside endosomes, which exhibit a proteinaceous corona. Scale bars: A, B: 2 µm. A1, C-E: 1 µm.

In cells treated with 30 µM imipramine, a moderate formation of DRVs (fig. 2-10) could be observed. However, these cells also tended to round up and generally showed a higher-absorbing cytosol, resulting in overall poor contrast in the cryo-SXT data. While not enough data for quantitative analysis could be acquired, the multilamellar nature of the structures could also be confirmed by TEM analysis (fig. 2-11).

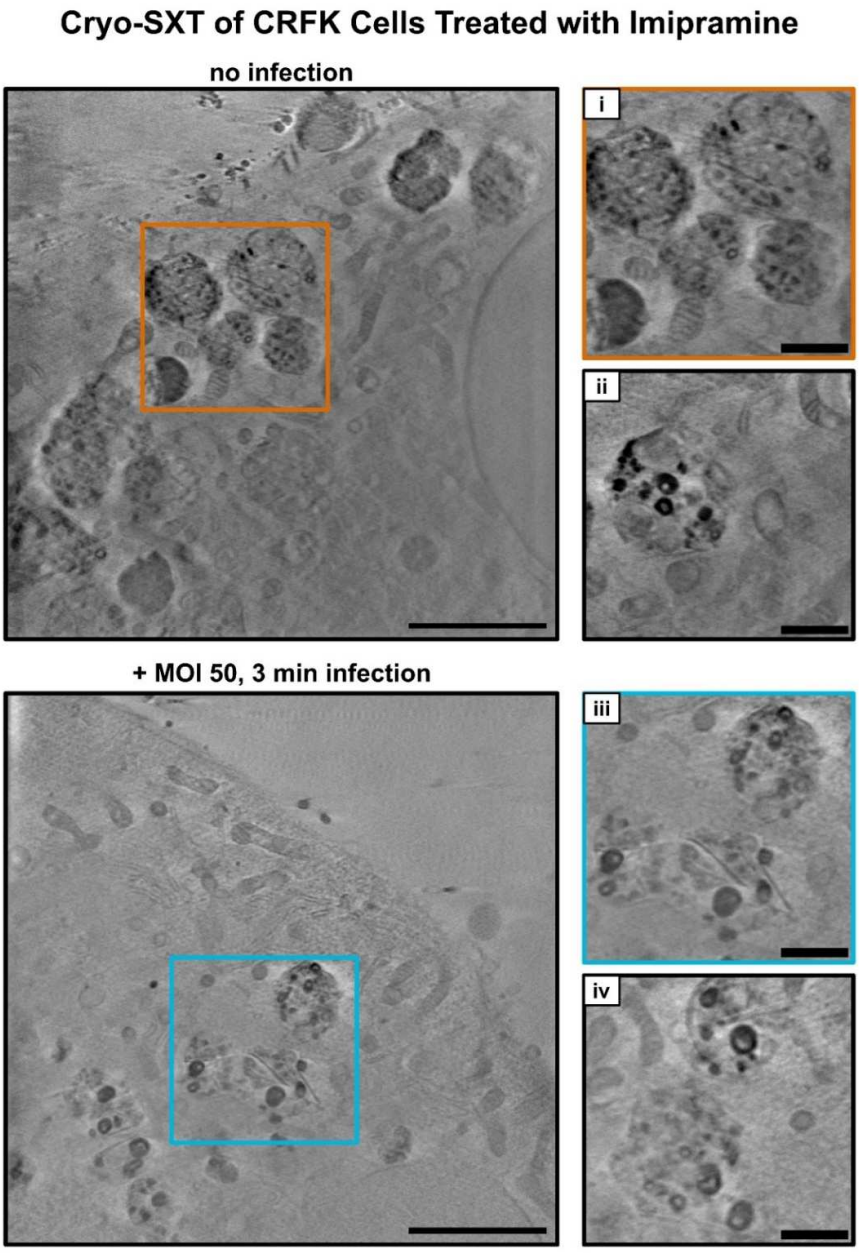

Figure 2-10: Cryo-SXT Visualizes DRVs Formed in Infected and Uninfected CRFK Cells Pre-treated with 30 µM Imipramine for 24 Hours. The colored boxes highlight the areas magnified on the side (panels i and iii). Panels ii and iv show other regions from the same datasets. All panels are minimum Z projections of 10 consecutive slices. Scale bars: large panels 3 µm. Small panels: 1 µm.

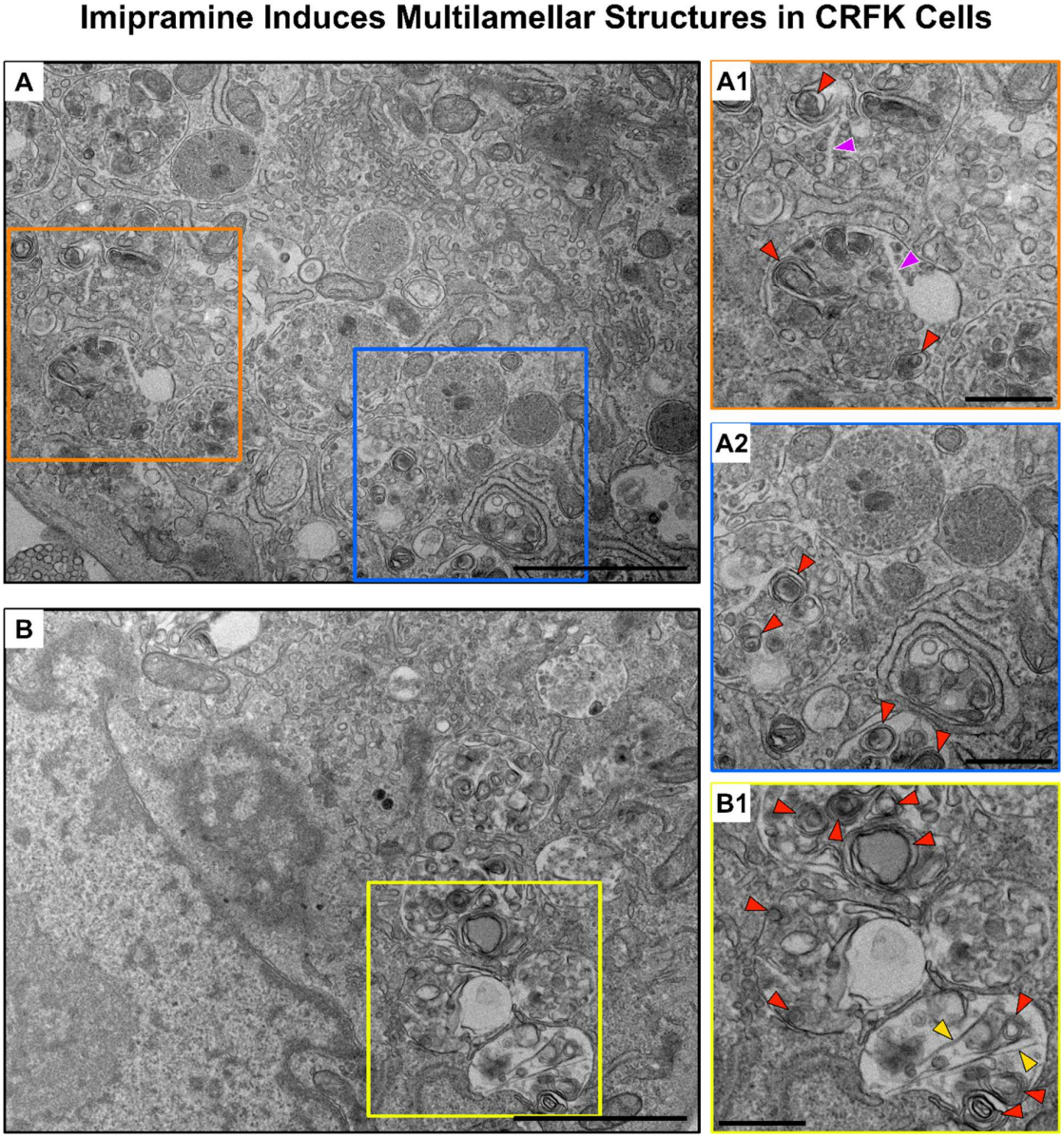

Figure 2-11: TEM Micrographs of Uninfected CRFK Cells Treated with 30 µM Imipramine for 24 Hours. Red arrows highlight multilamellar bodies. The yellow arrows highlight linear membrane features. Purple arrows denote regions where multilamellar structures appear to have been lost during sample preparation. Scale bars: Large panels: 2 µm. Small panels: 1 µm.

2.5. Effects of Fluvoxamine on Early Time Points of SARS-CoV-2 Infection

While studying the impact of the antidepressant drugs imipramine and fluoxetine on the infection by the feline coronavirus is of interest in its own right, investigating the causative agent of the COVID-19 pandemic was the ultimate goal of this work. Thanks to the effort and commitment of my collaborators in the veterinary medicine department of the Freie Universität Berlin, it was possible to perform some analysis of early time points of infection of SARS-CoV-2 in Vero E6 cells. Dr. Jakob Trimpert and his colleagues supported this work by performing experiments involving SARS-CoV-2 infection under the necessary biosafety level 3 conditions according to my guidelines for cryo-SXT sample preparation.

By the time the bulk of FIPV experiments had been performed and analyzed, another CAD family member, fluvoxamine, was being actively investigated by clinical trials for the treatment against SARS-CoV-2 and began showing positive results against SARS-CoV-2[50–52], while its mechanism of action remained elusive. Based on the observations made in the FIPV system at early time points, we aimed at investigating the potential effect of fluvoxamine on the infection of SARS-CoV-2 at early time points. In analogy to the experiments with FIPV, Vero E6 cells were treated with 10 µM fluvoxamine for 24 hours before being transferred to the BSL-3 environment, where they were infected for a few minutes and then fixed, alongside the untreated infected and mock-infected control cells.

As with the feline coronavirus, the initial question was whether any virus particles could be visualized by cryo-SXT at early time points of infection on or inside cells. Unfortunately, no SARS-CoV-2 virions could be visualized on the surface or in the cytoplasm of Vero E6 cells.

However, much unlike the observations in the feline model system, a striking formation of DRVs was observed inside the cells upon brief infection with SARS-CoV-2, even when they were not pre-treated with any drug. While uninfected, fixed control cells showed only few instances of small vesicles resembling the DRVs observed in CRFK cells, Vero E6 cells that were infected with SARS-CoV-2 rapidly formed many endolysosome-associated DRVs, which became even more abundant when the cells had been treated with fluvoxamine prior to (mock-)infection (fig. 2-12).

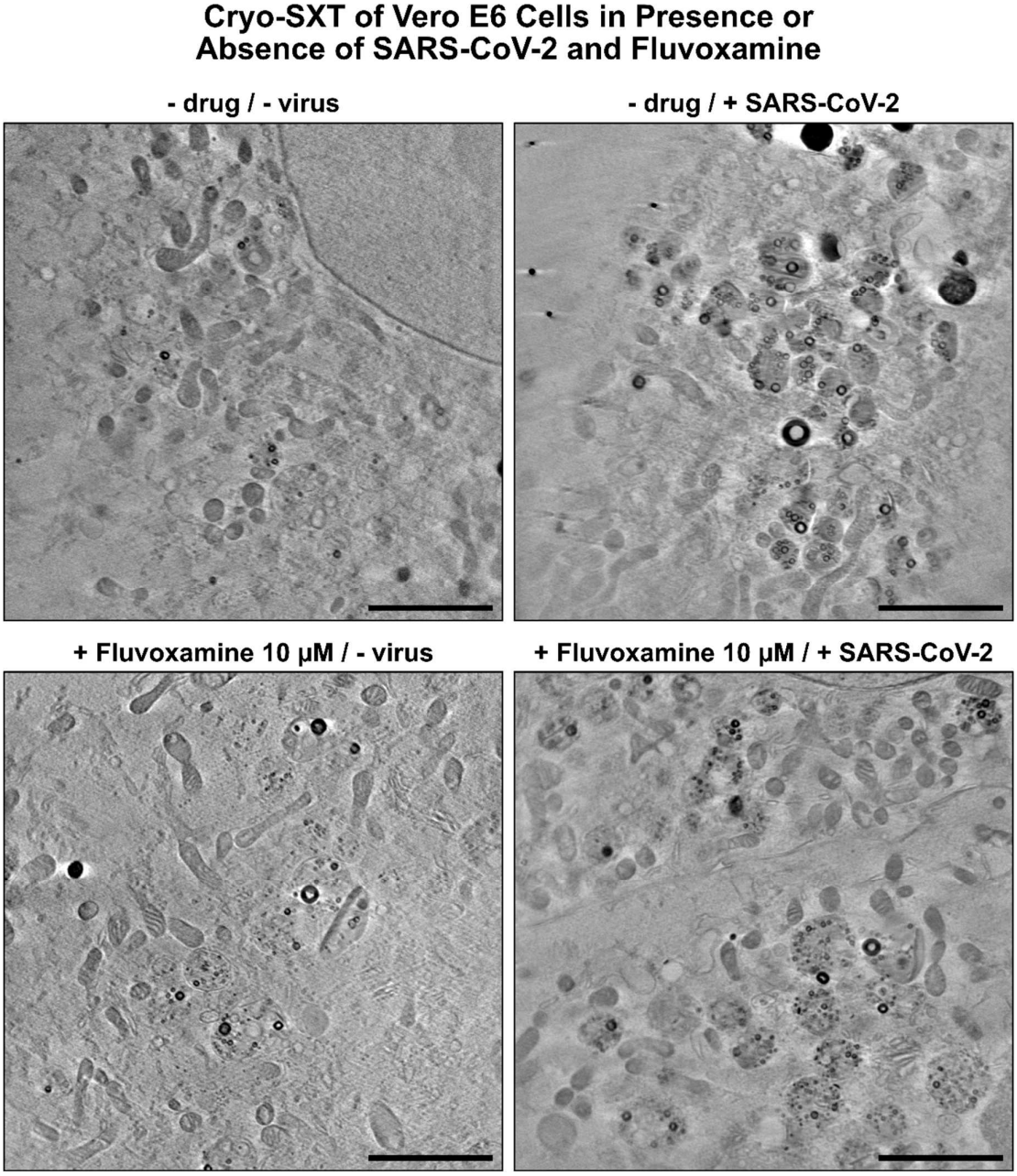

Figure 2-12: Cryo-SXT of Vero E6 Cells in Presence or Absence of SARS-CoV-2 and Fluvoxamine. In absence of drug and virus, cells form a small number of dark-rimmed vesicles. These dark-rimmed vesicles form in much higher numbers upon infection with SARS-CoV-2 for 5 minutes, treatment with 10 µM fluvoxamine for 24 hours, as well as when fluvoxamine-treated cells are infected. Shown are representative minimum Z-projections of 10 consecutive tomographic slices. Scale bar: 3 µm.

Quantification of manually segmented DRVs showed a striking difference in number and size of the DRVs across the different conditions. Vero E6 control cells formed an average of 47.8 DRVs per cell (see fig. 2-13). Upon infection with 10^7 pfu/ml of SARS-CoV-2 for 5 minutes, the average DRV number more than tripled to 161.1 DRVs/cell. Treatment for 24 hours with 10 µM fluvoxamine lead to a more than seven-fold increase in the DRV number in the one cell that could be analyzed. Cells infected with SARS-CoV-2 after 24 hours drug treatment lead to an even higher, 13-fold increase, with 626 DRVs per cell in comparison to controls. Furthermore, not only did the number of DRV change across conditions, but also their size. The DRVs formed in control cells had a median diameter of 245 nm. Upon infection with SARS-CoV-2, DRVs exhibited a similar median diameter of 254 nm. DRVs in drug-only cells were significantly smaller with a median diameter of 180 nm, which moderately increased in drug-treated infected cells to 211 nm, still below controls.

Interestingly, no DRVs were observed in untreated, uninfected control cells that were fixed directly from culture and not exposed to (mock-)infection conditions. Apparently, brief infection with SARS-CoV-2 and drug-treatment exert a cumulative effect on the number of DRVs in Vero E6 cells and pre-treatment with fluvoxamine significantly reduces DRV size in infected and uninfected cells.

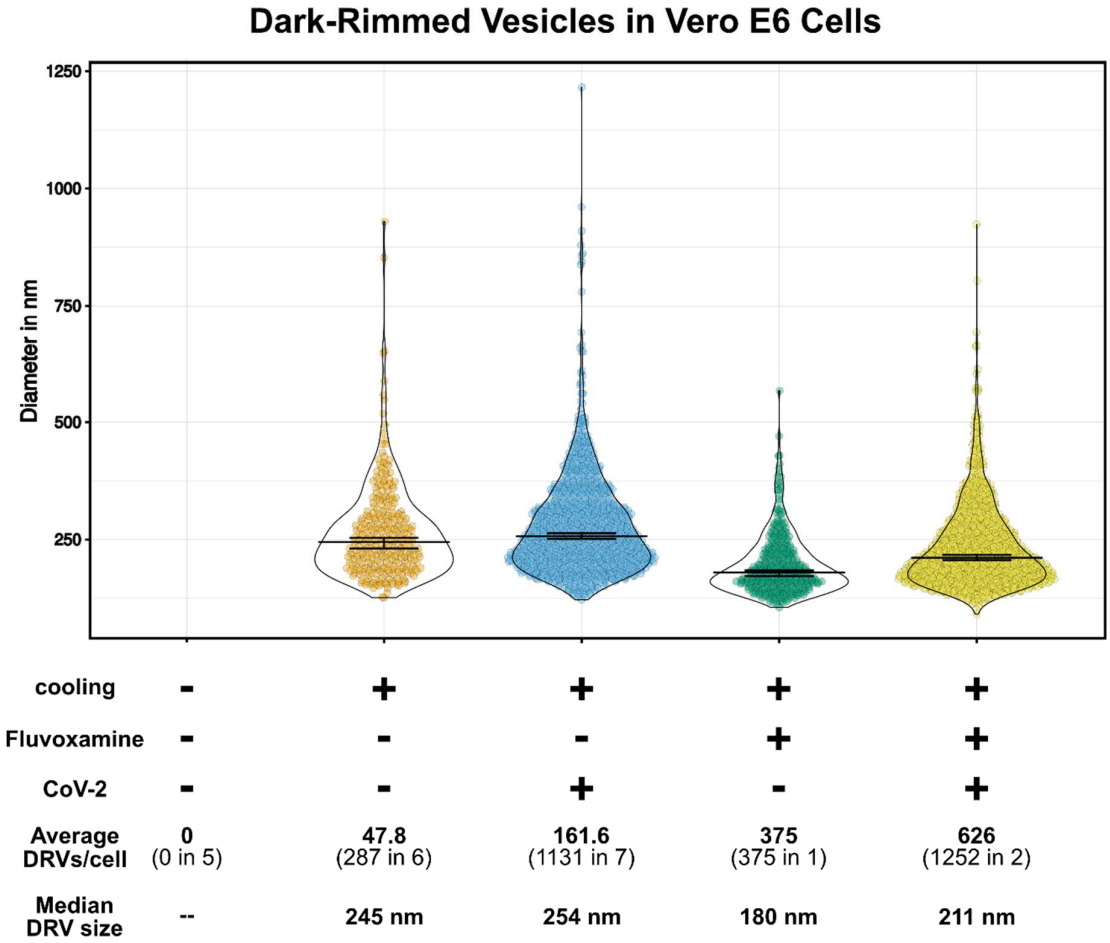

Figure 2-13: Size Distribution of DRVs in Vero E6 Cells in Presence or Absence of Fluvoxamine and SARS-CoV-2. The violin plots show major axis lengths of manually segmented dark-rimmed vesicles. The horizontal bar denotes the median, which is also written below the plots for each population. The error bars denote the 95% confidence interval. The number of dark-rimmed vesicles and the number of analyzed datasets are indicated under the graph. Fluvoxamine: pre-treatment with 10 µM fluvoxamine for 24 h prior to infection. CoV-2: infection with 10^7 pfu/ml SARS-CoV-2 for 5 min. Cooling: Cells that were infected or mock-infected were placed on cooled gel packs to allow synchronous uptake of the virus. The population on the far left were cells that, unlike the others, were not subjected to cooling and BSL-3 conditions, but instead fixed directly from culture. The plot was created using Plots of Data[130].

2.6. Discussion

The aim of the work presented in this section was to investigate the early steps of cellular remodeling caused by infection with viruses such as SARS-CoV-2 and FIPV at early time points and to find ultrastructural clues for the mechanism of viral inhibition exerted by the FDA-approved antidepressant drugs fluoxetine, imipramine, and fluvoxamine.

2.6.1. Surface-bound Coronaviruses Visualized by cryo-SXT.

Using the cryo-TXM at BESSY II, surface-bound FIPV particles could be clearly observed in tomographic reconstructions, as well as directly in scanning mode. Upon internalization of the particles, it became impossible to distinguish viral particles from other small intracellular features with confidence. The CRFK cells used for FIPV experiments are generally thicker than Vero E6 cells. As a result, the overall contrast in CRFK data is lower, as there is more carbon-dense material absorbing the soft X-rays. Still, in Vero E6 cells it was impossible to identify SARS-CoV-2 virus particles inside the cells in the cryo-SXT data. This is in accordance with work published by other cryo-SXT groups, where even at later stages of infection and replication, unambiguous distinction of SARS-CoV-2 virus particles by cryo-SXT alone is challenging[18,101,106]. However, our results showing FIPV virions binding to the cell surface and other published results[114] suggest, that visualization of SARS-CoV-2 is possible by cryo-SXT. Observing early binding events by cryo-SXT essentially depends on the amount of virus present and time available to screen for regions of interest.

2.6.2. Drug-Induced Dark-Rimmed Vesicles and Their Impact on Virus Replication

Even if intracellular visualization of viruses was not successful, the interplay of DRV size and number induced by drug-treatment and viral infection at a short timescale was a striking observation. The rapid and significant changes suggest an interaction between the early stages of the viral replication cycle and the effects of the drugs on the cell. This interaction could be responsible for the viral inhibition by the drugs.

The results are summarized in the two figures below for clarity: figure 2-14 for Vero E6 cells (SARS-CoV-2) and figure 2-15 for CRFK cells (FIPV).

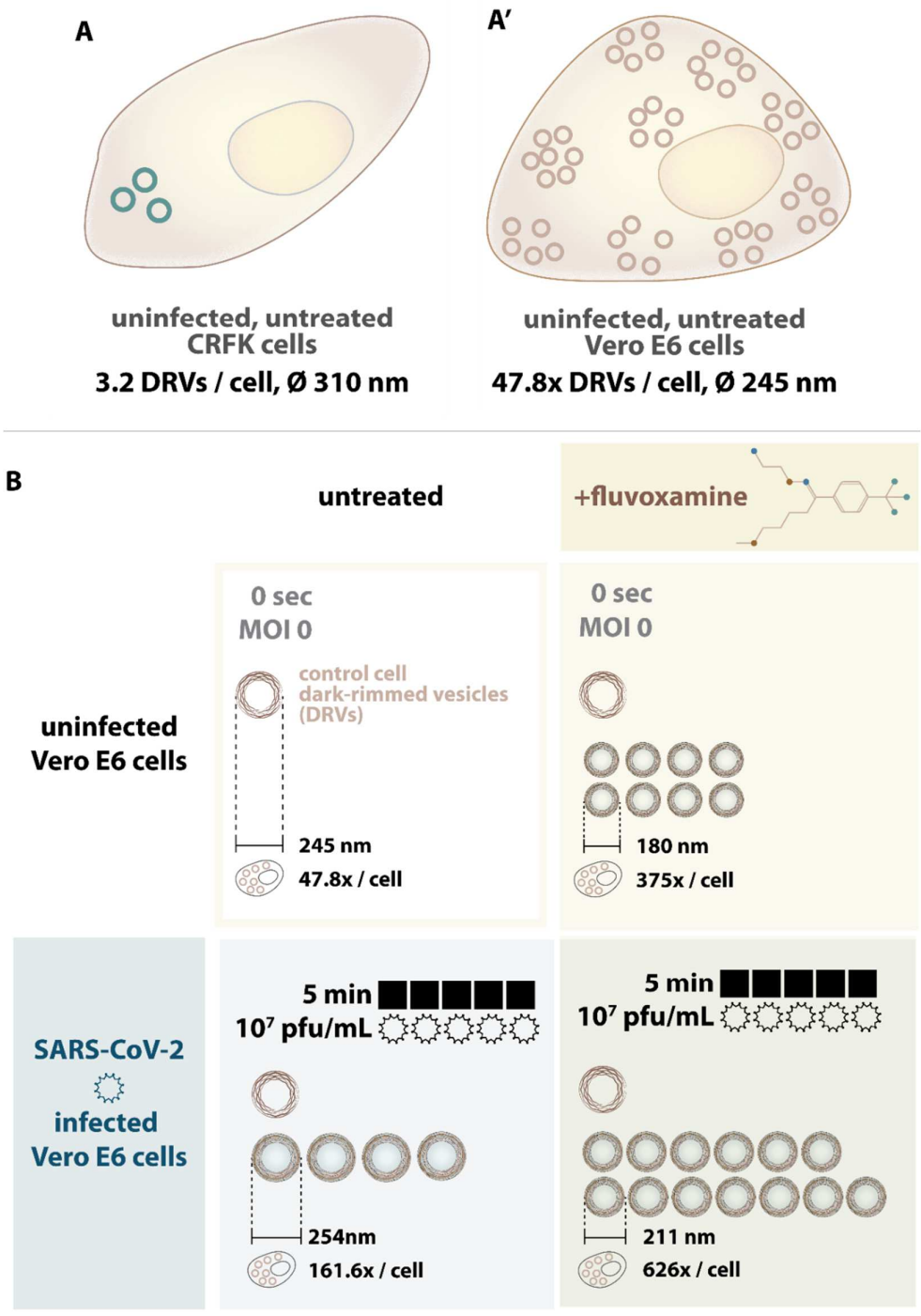

Figure 2-14: Summary of the Experimental Conditions and Results of the SARS-CoV-2-related Experiments in the Vero E6 System.

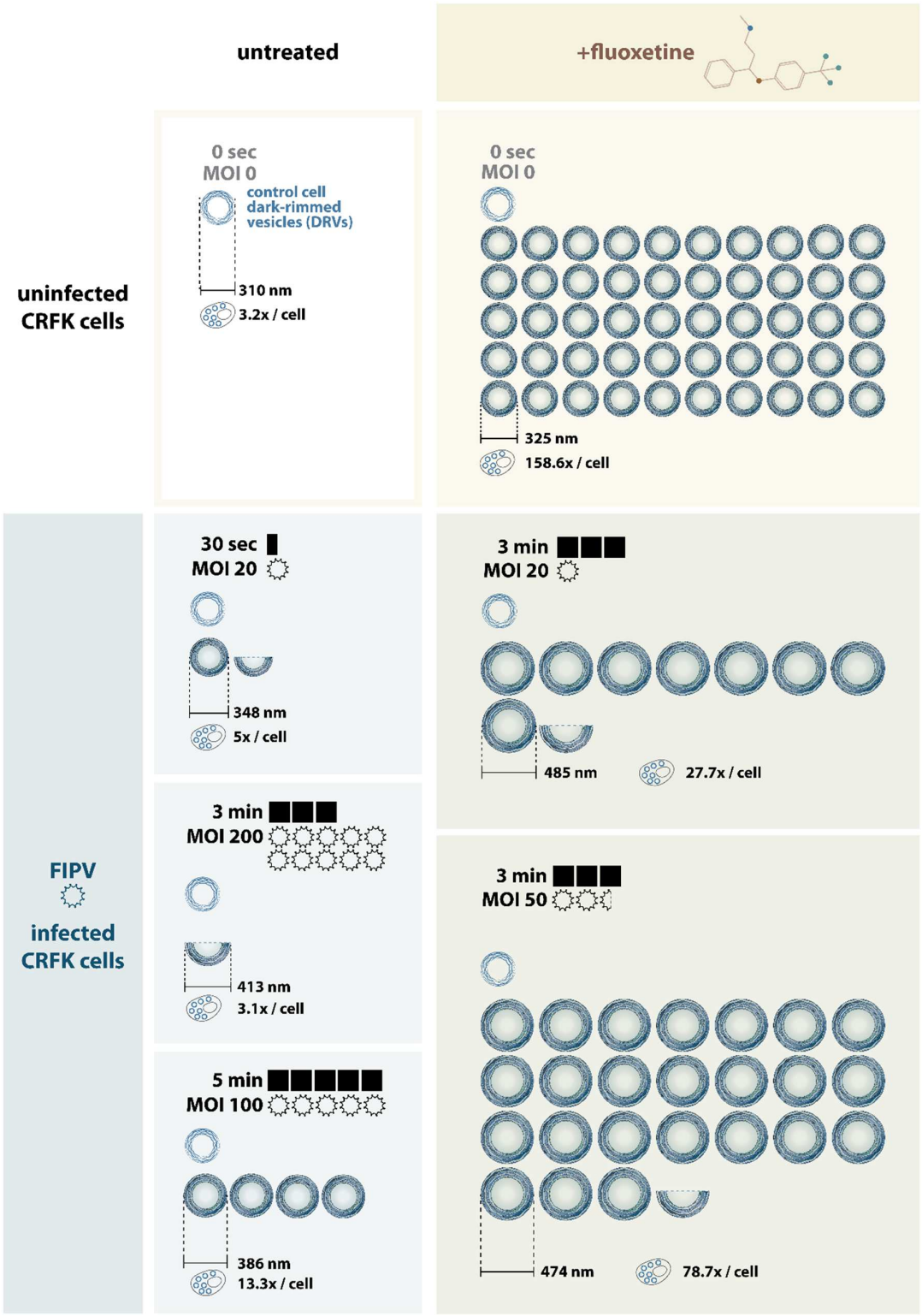

Figure 2-15: Summary of the Experimental Conditions and Results of the FIPV-related Experiments in the CRFK System.

The data presented here support two main modes of viral inhibition, which are described below.

2.6.2.1. Model 1: Inhibition of Lysosomal Escape

Drugs inhibit viruses by impairing viral fusion with the endolysosomal membrane. This model is supported by the endolysosome being the site of the most striking and rapid ultrastructural alterations in the form of DRV size and number in both systems. This suggests a direct involvement of the endolysosome in the viral inhibition caused by the drugs.

In the first model proposed here, CADs, including the three drugs used in this study, impair cathepsin function by increasing the lysosomal pH. This would block replication by preventing the pH-sensitive cathepsin L to proteolytically prime the spike protein for viral fusion with the lysosomal membrane and lysosomal escape. The proteolytic cleavage of spike in the lysosome is the second required priming event for SARS-CoV-2 fusion with the host cell membrane. The first event is mediated by activity of furin in the virus-producing cell[133–135] and the second cleavage can be performed either by cell-surface resident TMPRSS2[135,136] or endolysosomal cathepsin L[135,137] of the newly infected cell[9].

This mechanism of virus inhibition by elevated endolysosomal pH has been proposed for several CADs in the literature[35,38,138], and the involvement of cathepsins in endolysosomal escape has been reported for several coronaviruses, including MERS, SARS-CoV, SARS-CoV-2, and FCoV[29,35,139–143]. The CADs fluoxetine, fluvoxamine, imipramine and others have been reported to elevate lysosomal pH and impair lysosomal function[35,144–148], some of which also inhibit replication of viruses *in vitro*[149–151], including FIPV[32] and SARS-CoV-2[152–156].

2.6.2.2. Model 2: Lipid Accumulation Prevents Host Membrane Remodeling

The drugs alter lipid metabolism and thereby interfere with membrane-dependent steps of the viral replication cycle by making the required lipids unavailable. As viruses, FIPV and SARS-CoV-2 depend on the host cell membrane system for their replication. Not only do newly formed virions require host cell membrane to form their envelopes, but coronaviruses are also known to perform extensive remodeling of the cell membrane system by forming the characteristic double-membrane vesicles as replication organelles. All these steps depend on the mobilization of host cell lipids and therefore it is likely that interference with lipid metabolism could disturb the viral life cycle on at least one level[157,158].

A key observation supporting this model is that the drugs themselves induced DRV formation and that these structures were altered by both viruses. This suggests a direct link between the effects of the drugs and the virus on the cell. The drug-induced DRVs observed in cryo-SXT were

confirmed to be multilamellar structures by TEM analysis. Such lysosome-associated, multilamellar structures are a known hallmark of lipid accumulation in cells, which the drugs can induce by several different mechanisms.

These mechanisms of drug-induced lipid-accumulation are based on the drugs' lysosomotropic behavior, which then interferes with the function of specific lysosomal enzymes that are involved in lipid metabolism. Blockade of these enzymes leads to accumulation of one or several kinds of lipids. For instance, fluoxetine, imipramine, and chloroquine can prevent the degradation of polar lipids by inhibiting their binding to phospholipases, leading to lysosomal accumulation of phospholipids in a process called phospholipidosis[38,154,159–162]. Furthermore, fluvoxamine, fluoxetine, imipramine and hydroxychloroquine are also known to inhibit the lysosomal enzyme acid sphingomyelinase (ASM), thereby blocking the conversion of sphingomyelin to ceramide, which plays a central role in sphingolipid catabolism[163–165]. Lastly, imipramine and U18666A, another CAD family member, inhibit lysosomal cholesterol transporter protein NPC-1, leading to accumulation of cholesterol[166–170].

Individually or cumulatively, these mechanisms could block membrane-dependent processes of viral replication. The inhibition of phospholipases, ASM, and NPC-1 each leads to the formation of lysosome-associated multilamellar structures[163,171–174], which would be observed as dark-rimmed vesicles by cryo-SXT. While their physiological implications are still not fully understood, all of these mechanisms of inhibition have been proposed to be involved in inhibition of SARS-CoV-2[35,36,175–183], FCoV[184] or other viruses[35,129,145,164,167,185,186].

It is highly likely that the DRVs shown in the data of this work consist of more than one type of accumulated lipid. Several CADs, including fluoxetine and imipramine, have been implicated in more than one of the pathways listed above and are therefore probably interfering with viral replication on more than one level. In addition to the data presented in this thesis, this is further supported by the extensive body of literature highlighting the involvement of lipids with SARS-CoV-2 replication. In particular cholesterol has repeatedly been linked to play a role in the life cycle and infectivity of SARS-CoV-2[157,187–192]. However, despite extensive research, specific mechanistical roles which cholesterol and other lipids such as sphingolipids play in relation to infection by SARS-CoV-2 or other coronaviruses are still under debate[157,193] and concrete mechanistical evidence is still lacking[35,36,182,183,192,194]. For instance, while many authors use the lipid raft model to explain a potential cholesterol-mediated organization of ACE2 and other fusion-related factors[188,195–197], other authors suggest a role in fusion dynamics of the virus and host membrane[190,193] or directly challenge the conventional lipid raft model altogether[157,193,198].

This highlights that studying the effects of these drugs is not only relevant for better understanding virus infections, but also membrane biochemistry at a more fundamental level.

2.6.2.3. Cumulative and Cell-Type Dependent Mode of CAD-mediated Inhibition

Both modes of inhibition proposed here, i.e. lysosomal entrapment and lipid dysregulation, are not mutually exclusive. In both cases, functions of the lysosome are impaired by the lysosomotropic behavior of CADs. Inactivation of pH-dependent cathepsin, as well as the different mechanisms of lipid accumulation in lysosomes are the result of impaired lysosome function.

Furthermore, it is also likely that the specific interplay of such pathways is cell-type specific. For instance, the SARS-CoV-2 entry route is believed to be influenced by the cell type-specific expression of TMPRSS2[133,149]. The Vero E6 cell line used in this work has virtually no expression of TMPRSS2[199,200] and favors the endolysosomal route for SARS-CoV-2 internalization instead of fusion at the plasma membrane[149,201]. In such a system, the impact of lysosomal impairment on viral entry will be more significant than in cell lines that are more permissive to direct entry at the plasma membrane, which has been demonstrated for SARS-CoV-2[143,149,153]. In fact, this has been described previously to explain the cell type-specific efficacy of chloroquine and hydroxychloroquine against SARS-CoV-2 *in vitro*[143,153] and why these drugs ultimately failed to convince in clinical studies[39–49]. However, even though the drugs did not succeed in the clinical application against SARS-CoV-2[54], their apparent effects on the cellular and viral pathways make them valuable tools for further studying viral infection and cellular lipid metabolism.

2.6.3. Virus-Induced Particle Clearance Response in Epithelial Cells

The previous sections described models of how the drug-induced DRVs could relate to the viral inhibition. However, this on its own does not explain the changes in DRV size and number that occurred when drug-treated cells were infected with virus or the marked formation of DRVs in presence of SARS-CoV-2 in untreated Vero E6 cells. Both observations strongly suggest a direct, drug-independent cellular response to the presence of viral particles.

Multilamellar structures in epithelial cells are believed to sequester and expel nanoparticles from the cells by secretion as a clearance mechanism against nanoparticles[202–206]. Viruses are not only infectious agents, but also nanoparticles. Therefore, they could stimulate a cellular clearance response in epithelial cells such as the kidney cell lines CRFK and Vero E6 used in this work[207–209]. This mechanism is not mutually exclusive with the two models explaining the drug-induced formation of DRVS and would explain the formation of DRVs in absence of drugs upon infection

viruses. Furthermore, it also matches with the reports of increased numbers of MLBs in studies using gold nanoparticles[202] or carbon nanotubes[203], as well as the sequestration of nanoparticles into MLBs over time[202,204–206]. This hypothesis is further supported by reported accumulation of such organelles in Vero E6 cells infected with SARS-CoV-1 within 15 minutes[210,211] or 6 hours[209]. In the case of SARS-CoV-2, a clear virus-induced accumulation of such multilamellar structures in association with double-membrane vesicles was reported in Vero 81 cells at 24 hpi in comparison to uninfected controls[2]. Furthermore, multilamellar bodies were reported in Vero cells at 24 to 72 hpi but without quantitative assessment in comparison to controls[212–215]. Reports of multilamellar bodies in untreated and uninfected Vero E6 cells[207–209] confirms the observed baseline formation of DRVs shown in this dissertation.

The reports on multilamellar body formation are almost exclusively based on transmission electron micrographs instead of volumetric imaging of large parts of multiple cells. The difficulty of comprehensively sampling and quantifying larger intracellular structures such as DRVs by TEM is a probable cause why MLB formation has been documented but rarely quantified across the literature in the context of SARS-CoV-1 and -2. This very point highlights the ability of cryo-SXT to screen for such structures and to visualize and quantify them comprehensively under varying conditions in absence of an established fluorescent marker.

2.6.4. Interplay of Drug- and Virus-Induced Effects

The drug-induced formation of the DRVs is a sign of impairment of one or several lipid metabolism pathways inside the lysosome and is by that also an indication of impairment of other lysosomal functions, such as the activity of cathepsins. This suggests two possible modes of inhibition, i.e. direct inhibition via impaired cathepsin function and a more systemic blockade of lipid availability to the viral reprogramming of the cell for formation of replication organelles and packaging of new enveloped virions.

The virus-induced formation of DRVs, which was particularly prominent in the case of SARS-CoV-2, is likely a cellular response of epithelial cells for clearance of foreign particles. It is possible that this could have evolved also as an innate cell defense mechanism against viruses. However, considering that the Vero E6 cell line used in this study is commonly used for the investigation of the infection by SARS-CoV-2, it is likely that this mechanism alone is insufficient to effectively prevent infection *in vitro*.

The formation of lysosome-associated multilamellar bodies for particle clearance also requires lipids. It is therefore intuitive that upon cumulative drug-treatment and viral infection, the drug-mediated lipid accumulation in lysosomes and multilamellar bodies formed for particle clearance exhibit a crosstalk as observed in the presented data. The different trends in both systems, i.e. decreased DRV number and increased size in FIPV-infected cells versus increased DRV number and size in SARS-CoV-2-infected drug treated cells compared to drug-only cells could be due to a number of possible factors. Additional experiments will determine to what extent these effects depend on the specific drugs and dosage, the cell lines, as well as the viruses. Each of these could play a role in the size and number of the DRVs formed.

2.6.5. Future Work

The different modes of inhibition can be tested by some key experiments.

Key experiment 1: Track the viral particles during uptake and replication in presence or absence of each of the drugs by fluorescent markers. Fluorescent tagging of membrane or nucleocapsid proteins can be used to track virus particles throughout most of their replication cycle. Accumulation of tagged viruses inside the lysosome would support the hypothesis of impaired fusion. If, however, a later stage of the replication is blocked, tagged proteins would likely accumulate in, for instance, viral secretory vesicles. The results will be an important indication for the stage which is being blocked by the drugs. It should be noted, however, that the use of tagged viruses or antibodies would not cover the entire replication cycle. Upon viral fusion with the host membrane and virion disassembly, additional reporters are required to monitor the progression of viral replication inside the cell, until virus assembly will again provide epitopes for antibody detection. RNA Fluorescence in-situ hybridization (RNA-FISH) experiments could be used to monitor the replication of genomic RNA inside the cells as a quantifiable readout for inhibition of replication.

The results will furthermore provide an important reference for the other experiments. Live-cell fluorescent microscopy at early time points with fluorescently labeled viruses can also help resolve whether the viruses do in fact become sequestered and expelled by a cellular clearance pathway.

Key experiment 2: Morphological analysis of the host cell membrane system by cryo-SXT in presence and absence of drugs to determine inhibited steps of cellular reprogramming. Cryo-SXT can visualize and quantify morphological alterations such as the dark-rimmed vesicles, as

well as the characteristic double-membrane vesicles serving as replication sites for coronaviruses. The blocked or delayed formation of these replication organelles would indicate an early interference with viral entry or host cell membrane remodeling by the virus. This will be an important structural lead as to whether DRV size and number does correlate with formation of the viral replication organelles. Such a finding can clarify further the specific implications of lipid metabolism on viral replication. Alternatively, dose-dependent, drug-induced aberrant morphology of replication organelles would support the hypothesis of viral inhibition by lipid dysregulation.

Complementary experiment 1: Morphological screenings with expansion microscopy to test experimental conditions more broadly and complement cryo-SXT results. Cryo-SXT is most efficient when the experimental conditions are optimized. Many of the effects observed in this work are likely to depend on drug concentration, viral titer, and incubation times. Therefore, a complementary screening tool for morphological alterations would be invaluable. The following chapter describes the expansion microscopy (ExM) technique in detail and proposes its application as a screening tool for cryo-SXT. In the context of the results in this chapter, ExM could be used to optimize the experimental parameters and identify the optimal time points for which cryo-SXT could be most efficiently used. Furthermore, ExM is a very accessible way of testing the different hypotheses in other cell lines by general morphological analysis, before confirming results by cryo-SXT.

Complementary experiment 2: Combine virus tracking and high-resolution ultrastructural context by correlative light and X-ray microscopy (CLXM). Combining cryo-SXT with fluorescently tagged viruses or fluorescent reporters for viral infection allows correlative light and X-ray microscopy (CLXM). This approach will add specificity of fluorescent labeling to the overall ultrastructural context in the cells. This experiment will identify morphological blockades, while also tracking viral particles or the progression of infection inside the cells. Furthermore, screening for infected cells in cryo-SXT will be more efficient with a fluorescent reporter, as has been done previously[106].

Complementary experiment 3: Compare phenotypes from knockdowns with drug treatments. Knockdowns are important tools to dissect the involvement of specific host cell factors and the pathways they mediate, such as, for example, the lipid metabolism. Comparing the phenotype (e.g. viral itinerary and replication in the host cell) resulting from knockdown of host cell factors with the phenotype from drug treatments will clarify the specific contributions of the knockdown targets. Comparison of the effects of knockdowns with those of different doses of the drugs and combination of knockdown and drug treatments will clarify the roles of different pathways in the overall inhibition of virus replication. Interesting targets for knockdowns are acid

sphingomyelinase, phospholipases, the cholesterol transporter NPC-1, as well as cathepsins, and TMPRSS2.

Complementary experiment 4: Quantify the viral infectivity after drug treatment or knockdowns. Since the envelope of coronaviruses is produced by the host cell, its composition is likely to be affected by dysregulation of lipid metabolism in the host cell upon drug treatment or knockdowns. Comparing the viral replication on the RNA-level (e.g. quantitative PCR) in drug-treated host cells and the infectivity of the thereby formed viruses by plaque assay can reveal a possible impact of the drug treatments or knockdowns on infectivity of the virus.

Complementary experiment 5: Probe the activity of cathepsin L and endolysosomal lipid processing enzymes versus the lysosomal pH across drug concentrations. Measuring both parameters simultaneously within cells will show whether the drugs do in fact elevate lysosomal pH and effectively inhibit cathepsin function at the concentrations used in this work. This is crucial to determine the importance of cathepsin function to the observed inhibition, i.e. the validity of the mode of fusion impairment. Also, it will clarify to what extent the inhibition is dependent on elevation of lysosomal pH by the drugs and whether this effect is the same for the three different drugs.

2.7. Conclusion

The work presented in this chapter aimed at studying ultrastructural alterations in mammalian cells caused by infection with FIPV and SARS-CoV-2. Cryo-SXT experiments clearly showed in both virus systems that the DRV formation induced by drugs and the cellular response to coronavirus uptake interact with each other. The rapid change in lysosome-associated DRVs at early time points of infection strongly suggests an important role of lysosomal function in inhibition of the coronaviruses by the drugs. This illustrates a significant strength of cryo-SXT, which directly detected such a striking morphological alteration in cells.

All the tested drugs induced formation of many dark-rimmed vesicles. This suggests drug-induced accumulation of cholesterol, sphingomyelin, or phospholipids, as noted in the literature. Further study will clarify the more specific interactions of lysosomal functions, i.e. lipid metabolism, pH, and activity of cathepsins, with the infection by coronaviruses. Determining the relevance of the proposed modes of interactions will not only be important to better understand the mechanisms of existing and possibly future coronaviruses, but also to advance our understanding of fundamental cell biology.

3. Ultrastructure Expansion Microscopy

3.1. Abstract

Ultrastructure Expansion Microscopy (U-ExM) is a version of ExM, which robustly provides 4 - 4.5x expansion of biological specimens. It can be used to visualize the overall cellular architecture by global NHS-ester stains, or to highlight specific antigens or organelles by antibody or lectin stains. The method requires less time and equipment to be implemented, and thus has the potential to perform initial screenings on cellular ultrastructure under given experimental conditions more efficiently than higher-resolution ultrastructure techniques such as cryo-SXT. However, the extensive sample processing required for U-ExM raises questions on the introduction of artifacts and distortions. Based on the extensive 3D-ultrastructural data collected on Vero E6 and CRFK cells, it was possible to compare the ultrastructural preservation of different organelles in U-ExM and cryo-SXT. It emerged that especially large, easily identifiable organelles such as nucleus, mitochondria and the plasma membrane can be studied very effectively by NHS-ester stains in U-ExM. Complementary use of stable fluorescent probes can also support analysis of Golgi apparatus, ER and other organelles. However, vesicular organelles and especially drug-induced multilamellar organelles were difficult to interpret due to high background, poor anchoring of lipids and occurrence of small structural polymerization defects. While the ongoing development of novel sample preparation procedures and labeling techniques is likely to further advance the application of expansion microscopy, it also highlights the need for rigorous validation of sample preservation and vigilance in the interpretation of ExM data in absence of additional ultrastructural evidence acquired under near-native conditions by techniques such as cryo-SXT. Therefore, U-ExM and cryo-SXT could be used in complement to each other, with cryo-SXT offering structural validation by near-native imaging and U-ExM offering faster, decentralized screening for general ultrastructural alterations.

3.2. Introduction: Analysis of Cellular Ultrastructure by Expansion Microscopy

3.2.1. The Principle of Expansion Microscopy

With all its advantages, conventional fluorescence microscopy is limited by the diffraction of light, such that the resolution is typically limited to 200 nm in XY. Recent years have shown significant technological improvements to overcome that barrier with a series of super-resolution techniques. Generally, these techniques rely on innovations of either the microscope (STED), fluorophore properties (photoactivatable dyes, STED dyes) or computational processing (deconvolution, SRRF). These tools represent significant technological advancements; however, their implementation is not accessible to every laboratory.

Instead of using advanced optics or computational devices, increasing the distance between the points in an isotropic manner is an alternative method to obtaining spatial information at a higher resolution than initially possible. Since the introduction of the concept of Expansion Microscopy (ExM) by the work of Boyden et al. in 2015[216], many variations of this technique have been developed. They share the same basic idea to anchor and embed a fixed biological sample (cell monolayers or tissue) to a swellable polymer matrix which is polymerized throughout the specimen. Once the polymerization is complete, the original sample is homogenized by heat denaturation or enzymatic digestion, while the structural components remain linked to the hydrogel matrix. Once the hydrogel is placed in water, the structural components of the specimen are spatially separated from one another by the swelling of the hydrogel. The spatial separation is characterized by a measurable expansion factor, which can range from four-fold up to 21-fold expansion[216–222], depending on the sample and specific expansion microscopy technique applied.

Expansion microscopy is a very young field, with novel techniques and variations constantly emerging. Many avenues of further technical advancements are being followed, such as 1) optimization of hydrogel chemistry for higher and more reproducible expansion factors and gel consistency, 2) improved retention and labeling efficiency of biomolecules such as proteins, lipids, nucleic acids and glycans and 3) sample preparation for diverse organisms and samples. A series of excellent reviews provide an overview over these questions and developed techniques[223–226].

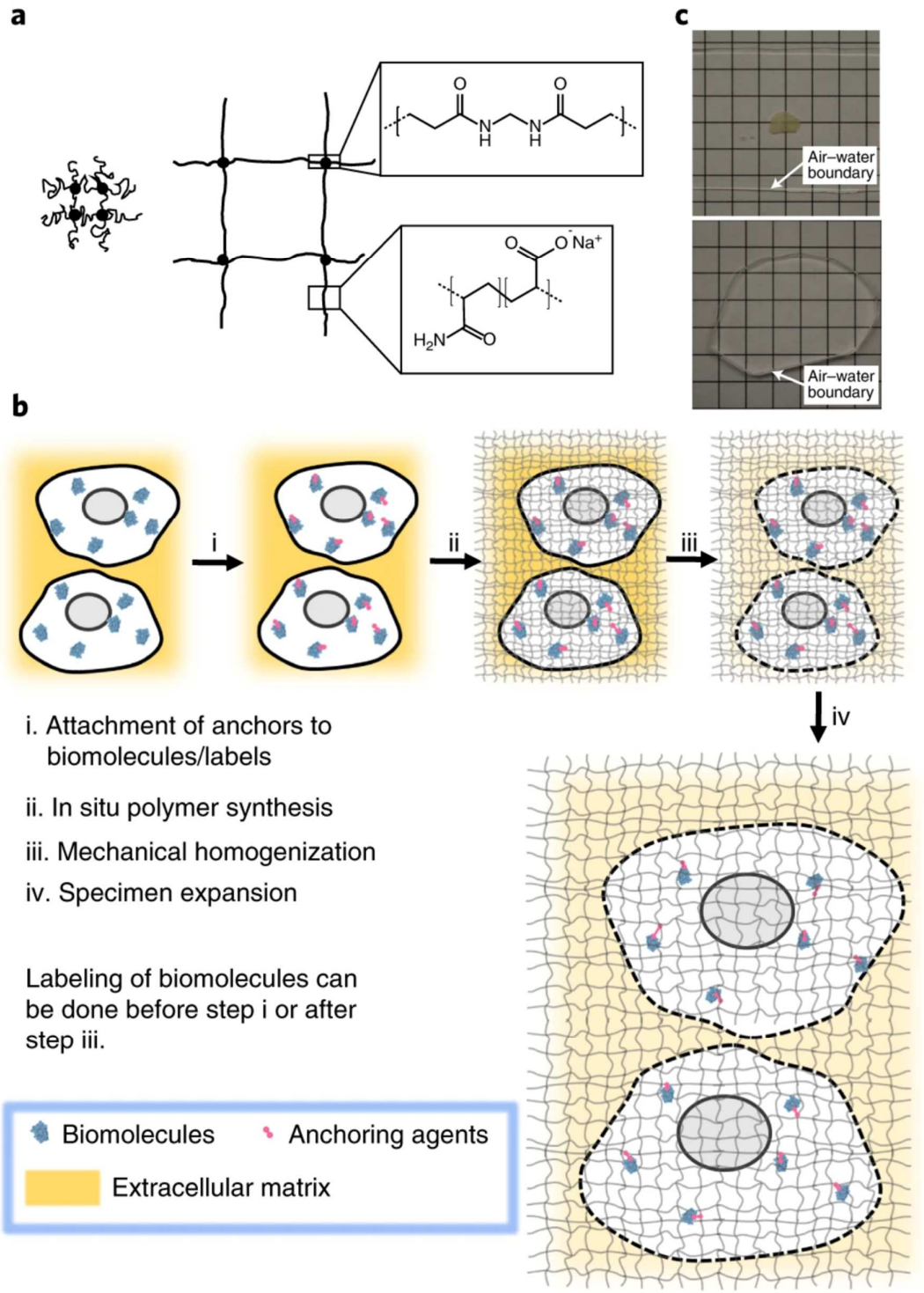

Figure 3-1: Overview of the Expansion Microscopy Principle. A) Schematic of cross-linked poly-electrolyte gel before (left) and after expansion (right). The chemical structures of the N,N'-methylene bisacrylamide crosslinker and the sodium acrylate and acrylamide monomers are shown in the context of the polymer. The immobilization of negatively charged sodium acrylate causes the gel swelling upon removal of counterions. B) General workflow of expansion microscopy. C) Example of a mouse brain slice before (top) and after (bottom) expansion. Figure reprint from Boyden et al., Nat. Met. 2019[225] with permission from Springer Nature.

3.2.2. Advantages and Challenges of Expansion Microscopy

This general concept of expansion microscopy holds several key advantages:

Accessibility and modularity: This technique can be adopted readily by many laboratories, as it uses mostly common reagents and does not require extensive training to be performed. The Ultrastructure Expansion Microscopy protocol (U-ExM)[218] is being routinely used in our lab and taught to undergraduate students who consistently accomplish expansion factors of 4 - 4.5x. Furthermore, ExM does not rely on purchasing sophisticated, super-resolution microscope setups. However, it can be combined with advanced super-resolution techniques to achieve even higher resolution. For instance, expansion microscopy has been used in combination with STED imaging (ExSTED[227]), dSTORM[228] or the super-resolution radial fluctuations approach (ExSRRF[229]). Also, ExM protocols has been shown to be compatible with conventional labeling strategies such as antibody staining or DAPI, as well as global protein stain using fluorophores conjugated to n-hydroxy succinimide (NHS) to resolve the overall cellular structure[220,221].

Throughput: Protocols such as U-ExM can be performed within less than a week from fixation until image acquisition. In addition, the sample can be inspected after each step to follow the preparation success and the same cells can be traced over the course of the entire preparation and imaging. Therefore, it is possible to acquire statistically relevant numbers of datasets in a relatively short amount of time.

Still, there are also several important challenges of the technique:

Sample preservation: The very purpose of microscopy is to detect the original structure in the specimen as accurately as possible. However, the principle of ExM relies on physical expansion of the specimen, the original structure is subject to extensive alteration throughout the sample preparation procedure, i.e. fixation, anchoring, gelation, homogenization, and expansion. All these steps bear the risk of introducing artifacts, which need to be carefully controlled for to ensure that the final structure documented in the data actually represents an accurate and complete depiction of the original structure. The robustness of sample preparation is known to depend critically on the purity of the used chemicals. Especially the varying quality of commercially available sodium acrylate, a key ingredient for many ExM protocols[216,217,219,221,224,230], is a known difficulty in the field[221].

Labeling density: The act of expansion not only increases the distance between fluorophores that would be detected in the microscope, but also dramatically reduces the labeling density. With an expansion factor of four in all three dimensions, the concentration of fluorophores in a given

optical section will be reduced by a factor of 64 after expansion. This leads to a lower signal-to-noise ratio and can complicate detection of structural information. To deal with this, either brighter fluorophores or higher quantities of fluorescent probes may have to be used, potentially increasing the costs of the experiment. In addition, not all fluorescent probes are suitable for use in ExM and might suffer from significant signal loss throughout the sample preparation procedure.

In continuation of the previous chapter, it was important to find a technique which enables visualization of the global ultrastructure of cells as robustly as possible. Much of the research in the field is devoted to addressing these challenges and thus many different protocols have been published, including Magnify[220], Ten-fold Robust Expansion Microscopy[221] (TREX), panExM[222] and U-ExM[218] which also visualize the cellular ultrastructure. Based on previous experience in the lab, U-ExM was selected as the most robust technique, routinely producing consistent expansion factors, gel consistency and structure preservation. The central question of this chapter is whether and to what extent U-ExM could serve as a tool to study cellular ultrastructure either on its own or in complement with other techniques such as cryo-SXT.

To that end, two stains for visualization of the overall cellular ultrastructure were used:

N-hydroxysuccinimide (NHS) esters react with primary amines, such as the N-terminal alpha-amine or lysine side chains of proteins. NHS-derivatives of fluorescent dyes can be covalently bound to proteins under physiological or slightly alkaline pH. This can be used to stain all exposed primary amines of the proteins in the specimen, resulting in a global protein stain. Differences in labeling density between the cytoplasm and organelles or other structures provides the contrast required to visualize the general ultrastructure of the specimen, given that the conjugated dye used is chemically stable enough to survive the sample preparation procedure.

An alternative strategy to NHS-esters is the use of fixable membrane stains. Due to their high carbon content, structures with high lipid content, especially membranes, are the cellular components that typically produce the highest contrast in cells in cryo-SXT and are therefore the clearest hallmark of structural organization of the cell. A successful membrane stain can elucidate the cellular organization in a proper manner. Since most organelles are segregated by a lipid bilayer, a robust membrane stain can serve as an alternative to NHS-ester staining to resolve most of the cellular ultrastructure of a cell. For this approach to work in U-ExM, the membrane dye must be fixable and withstand the sample processing. Also, as with any other fluorescent dye, spectral properties such as brightness and emission spectra play an important role.

3.3. Results

3.3.1. NHS-esters and Fixable Membrane Stains Visualize Global Ultrastructure

Representative NHS-ester and membrane dye stainings of CRFK cells and Vero E6 cells in comparison to images from tomographic reconstructions of chemically fixed and vitrified cells are shown in figures 3-2 and 3-3. Both global staining approaches visualized a remarkable degree of structural information after expansion. Important organelles such as nucleus, mitochondria, the plasma membrane, and even portions of the ER and chromatin substructures can be readily identified in both stainings, as illustrated by the colored insets.

Furthermore, the visualization by U-ExM provided a significantly larger field of view and overall throughput than cryo-SXT. The colored boxes in both figures are equivalent to the 12 x 12 µm field of view in cryo-SXT after correction for the expansion factor. The entire field of view of the confocal spinning disk microscope is shown in the top row, indicating how the entire volume of an expanded cell can be captured in one acquisition very effectively by U-ExM, whereas cryo-SXT would require multiple acquisitions and stitching for such a large field of view.

Among the two staining methods, NHS-ester provided consistently higher quality and was often used as an additional stain to find cells for acquisition of other stains. ATTO® 565 and 647N NHS-ester stainings were used interchangeably during this project, both of which survived the harsh heat denaturation protocol well and provided bright signal. However, as expected, the high protein content of the cytoplasm led to a relatively high amount of background staining.

Multiple different fixable membrane dyes were tested, out of which only a few produced useful results. CellBrite® Fix 640 performed the most robustly and is therefore shown in most of the figures for membrane dyes. mCLING and CellMask™ orange also produced good results but were less robust overall. Lastly, FM™143FX had to be used in high concentrations to produce signal and showed extensive bleed through.

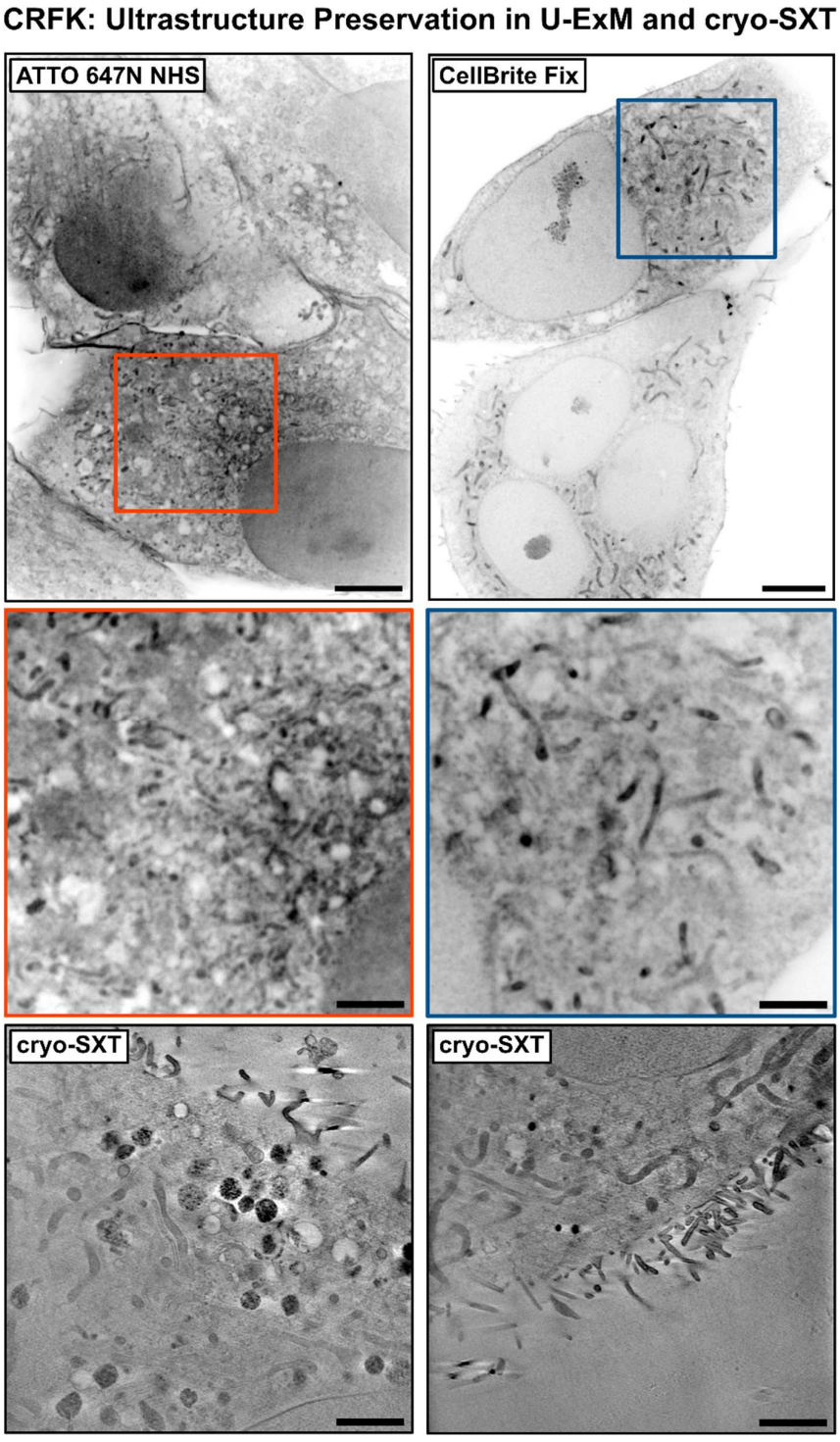

Figure 3-2: Comparison of Structure Preservation and Visualization of CRFK Cells by cryo-SXT and Global NHS-ester or Membrane Stainings in U-ExM. Magnified insets correspond to a field of view of 12 by 12 µm, equivalent to images from two representative cryo-SXT datasets below. Shown are representative minimum Z-projections of 10 consecutive tomographic slices. Scale bars: Top row: 5 µm. Insets and cryo-SXT images: 2 µm.

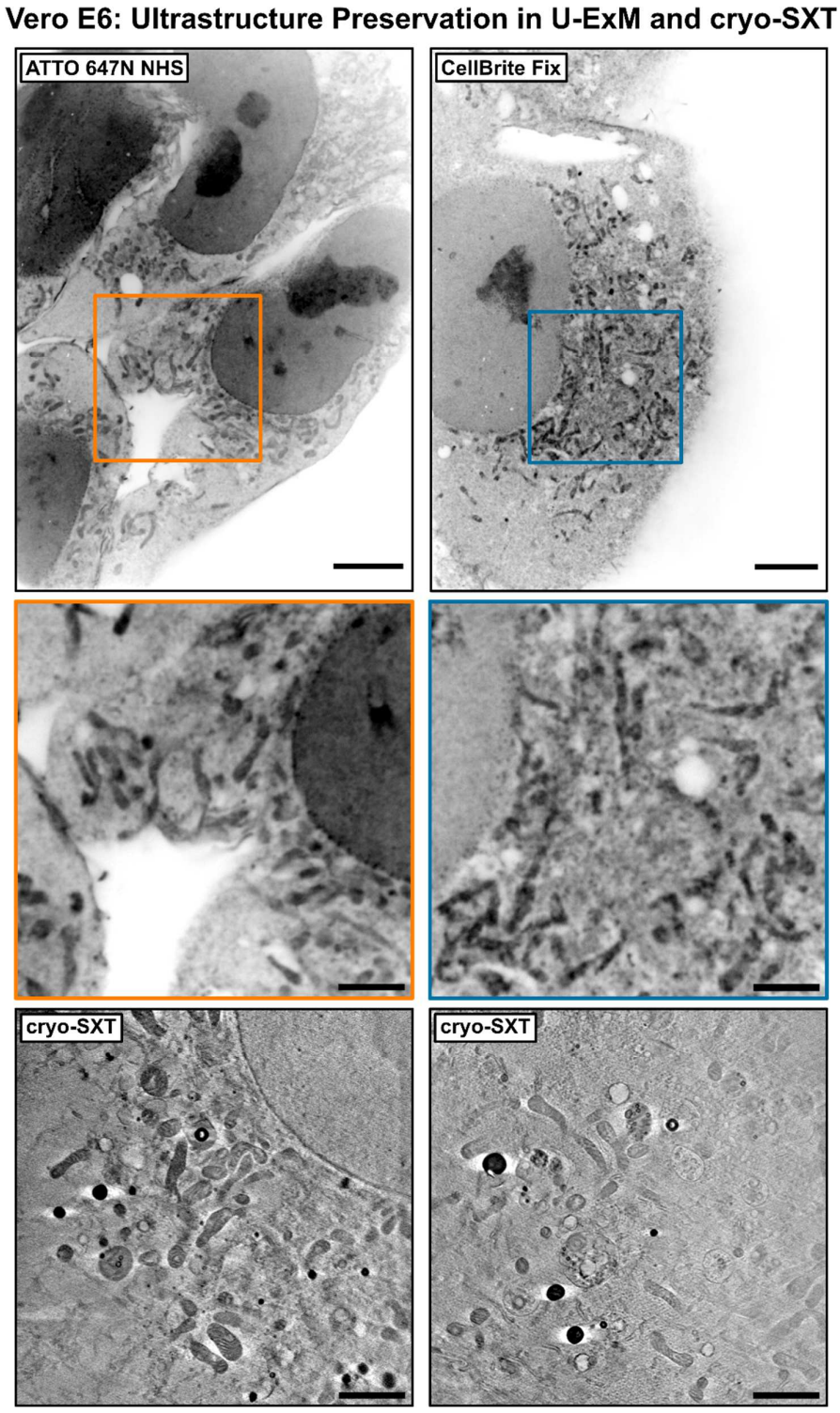

Figure 3-3: Comparison of Structure Preservation and Visualization of Vero E6 Cells by cryo-SXT and Global NHS-ester or Membrane Stainings in U-ExM. Magnified insets correspond to a field of view of 12 by 12 µm, equivalent to images from two representative cryo-SXT datasets below. Shown are representative minimum Z-projections of 10 consecutive tomographic slices. Scale bars: top row: 5 µm. Insets and cryo-SXT images: 2 µm.

3.3.2. Artifacts in cryo-SXT and U-ExM

Before comparing cryo-SXT and U-ExM in more detail regarding their potential for ultrastructural preservation and visualization, it is important to identify their potential sources of artifacts.

3.3.2.1. Fixation Artifacts

Fixation is a mandatory step in any expansion microscopy protocol, including U-ExM. For cryo-SXT, chemical fixation is not technically necessary, but the data showed in this section originated from the work related to the coronavirus project described in **chapter 2**, where they were to be compared to data of chemically fixed infected cells. Therefore, this section here cannot state observations related to artifacts introduced by the act of chemical fixation of cells.

3.3.2.2. Cryo-SXT-specific Artifacts

The technical artifacts that can arise in cryo-SXT were already described in the previous chapter. The most important ones are the missing wedge phenomenon, limited depth of focus, vitrification defects, and irradiation damage. With experience, these artifacts can be identified as such and taken into account during cryo-SXT data interpretation. Tomograms with extensive vitrification defects or irradiation damage were excluded from this work. However, the missing wedge artifact could not be eliminated and was observed, as expected, invariably as missing structural information on the bottom and top of every structure. The limited depth of focus of the X-ray optics decreases the quality of datasets of thicker samples. For this reason, the datasets of CRFK cells show consistently lower detail and contrast than those of Vero E6 cells, which are significantly thinner.

3.3.2.3. Expansion Microscopy-related Artifacts

The extensive sample processing procedure of expansion microscopy has the potential to induce artifacts. By comparing the structural preservation in U-ExM with the extensive data acquired of fixed, untreated CRFK and Vero E6 cells, it was possible to identify several types of such artifacts, which shall be described below (fig. 3-4).

Minor tears in the gel matrix were a commonly observed artifact during the experiments. These defects were at times very difficult to discern from actual cellular features with low labeling density, such as endosomes or smaller vesicles (see figure 3-4, blue arrows). Only very large or irregularly shaped regions with little signal could be clearly identifiable as artifacts. Even samples that showed overall high quality of preservation could still show some of these artifacts (see NHS-ester panels in fig. 3-4).

Especially in membrane stains, patches of stained regions would sometimes be visible in samples (figure 3-4, red arrows). They were easily visible on the plasma membrane and the nuclear envelope. Such features were never observed during this work in cryo-SXT, and they usually accompanied an overall poor structural preservation of the cells. In other cases, a network of such patches was seen across the cytoplasm (see top-right panel in fig. 3-4), in which cases the overall preservation was very poor.

A more subtle artifact was the deformation of mitochondria. In healthy CRFK or Vero E6 cells, the mitochondria would normally be visible as a network of elongated tubular structures with a comparatively high contrast against the remaining cytoplasm (see also fig. 3-7). In some instances, mitochondria appeared rounder with an unstained interior, where there would normally be cristae. This was usually observed in samples that also showed other signs of improper preservation but seemed to be an early indication of incomplete anchoring of the sample (see green arrows, fig. 3-4). Such rounding up of mitochondria was only observed in cryo-SXT in cells that had not been fixed and been subjected to not tightly controlled conditions prior to plunge freezing. An example for this is shown in the X-ray data in figure 3-6.

Lastly, the unequal expansion of organelles and the remainder of the cell was observed as an occasional artifact. Some drastic cases are shown in figure 3-4, highlighted by black arrows. Such detachment occurred in U-ExM on a batch-to-batch basis of the sodium acrylate stock. In cryo-SXT, nuclear blebs have been observed only rarely in much smaller sizes (see fig. 3-6). This artifact is not limited to the nucleus and may also occur with mitochondria or vesicles but did so on a much more subtle basis.

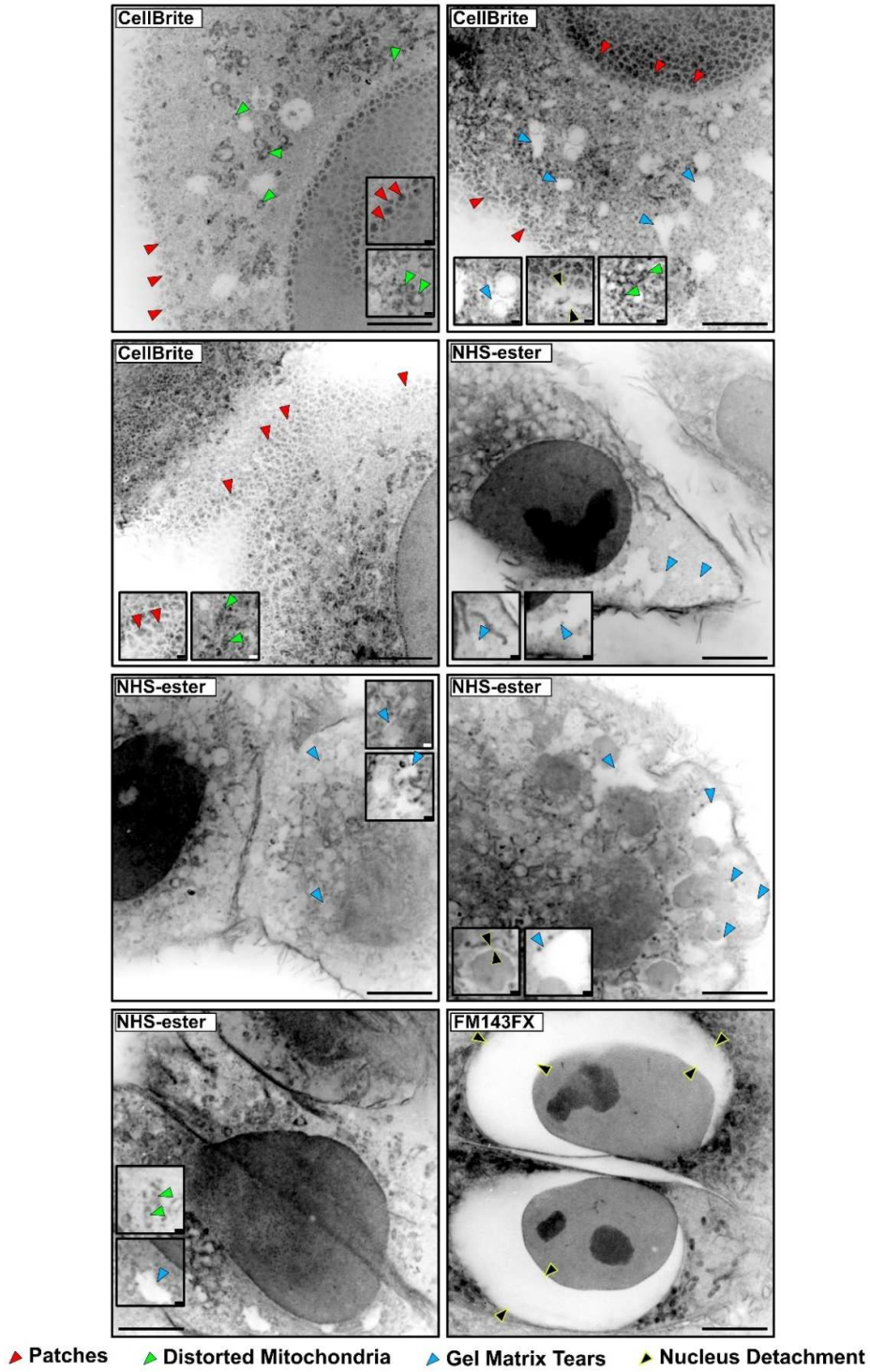

Figure 3-4: Global Stainings Visualize Artifacts in Samples Processed by U-ExM. Especially membrane stains occasionally show patched regions, especially on nuclear membrane and plasma membrane (red arrows). Sometimes, mitochondria appear rounder and with an unstained interior, contrary to the usual elongated structure (green arrows). Unstained, empty regions may arise due to insufficient fixation or anchoring of material, or tears in the gel (blue arrows). Organelles may expand differently than the cytoplasm, leaving a kind of empty halo around them (black arrows). Scalebars: 5 µm large panels, 500 nm small panels.

3.3.3. Ultrastructural Preservation of Different Organelles in cryo-SXT & U-ExM

3.3.3.1. Plasma Membrane

In U-ExM, the plasma membrane could not be visualized at the same level of detail as in cryo-SXT, due to the still lower resolution and the high level of background staining.

Figure 3-5 below illustrates structural details of the plasma membrane as visualized by cryo-SXT and U-ExM. In cryo-SXT, the plasma membrane is clearly visible, and the surface organization of a cell can be seen in detail. However, most mammalian cell types, including CRFK and Vero E6 cells, are larger than the field of view in cryo-SXT, meaning that in most cases, only a part of the plasma membrane can be captured. In the cryo-SXT acquisition shown in fig. 3-5, the focus was placed on the tip of the cell with the intention to visualize fine structures of the cell surface in that region. Towards the left side of the image, contrast and resolution decrease as a consequence of the increased cell thickness and limited depth of focus. However, the finer structure of the cell surface of the thinner parts of the cell (center and right) can be seen in detail. Invaginations in the cell surface (yellow arrows), small vesicles (red arrows) and even membrane blebs with interior substructure (green arrows) can be identified unambiguously. At times, the plasma membrane does not form a clear, dark outline, but the absorption contrast between cytoplasm and extracellular space allows clear distinction. The gold fiducial marks (purple arrows) or other highly absorbing features produce elongated, high-intensity artifacts, which often overshadow other features such as filopodia (figure 3-5, panels b, d), making it at times more difficult to clearly draw outlines (see also discussion in **chapter 4**).

As expected, NHS-ester stains could not visualize the cell outline as clearly as in cryo-SXT. Accordingly, invaginations or endocytic vesicles could not be clearly distinguished. However, larger features such as filopodia, membrane blebs (blue arrows), or large variants of blebs with substructures (green arrows) could be identified clearly and the overall shape of the cell was visualized more globally than what was possible with cryo-SXT, thanks to the substantially larger field of view (see fig. 3-2 and 3-3). Membrane stains such as mCLING offered a better contrast and level of detail than NHS-ester stains, however their staining quality was generally much less consistent that that of NHS-ester stains.

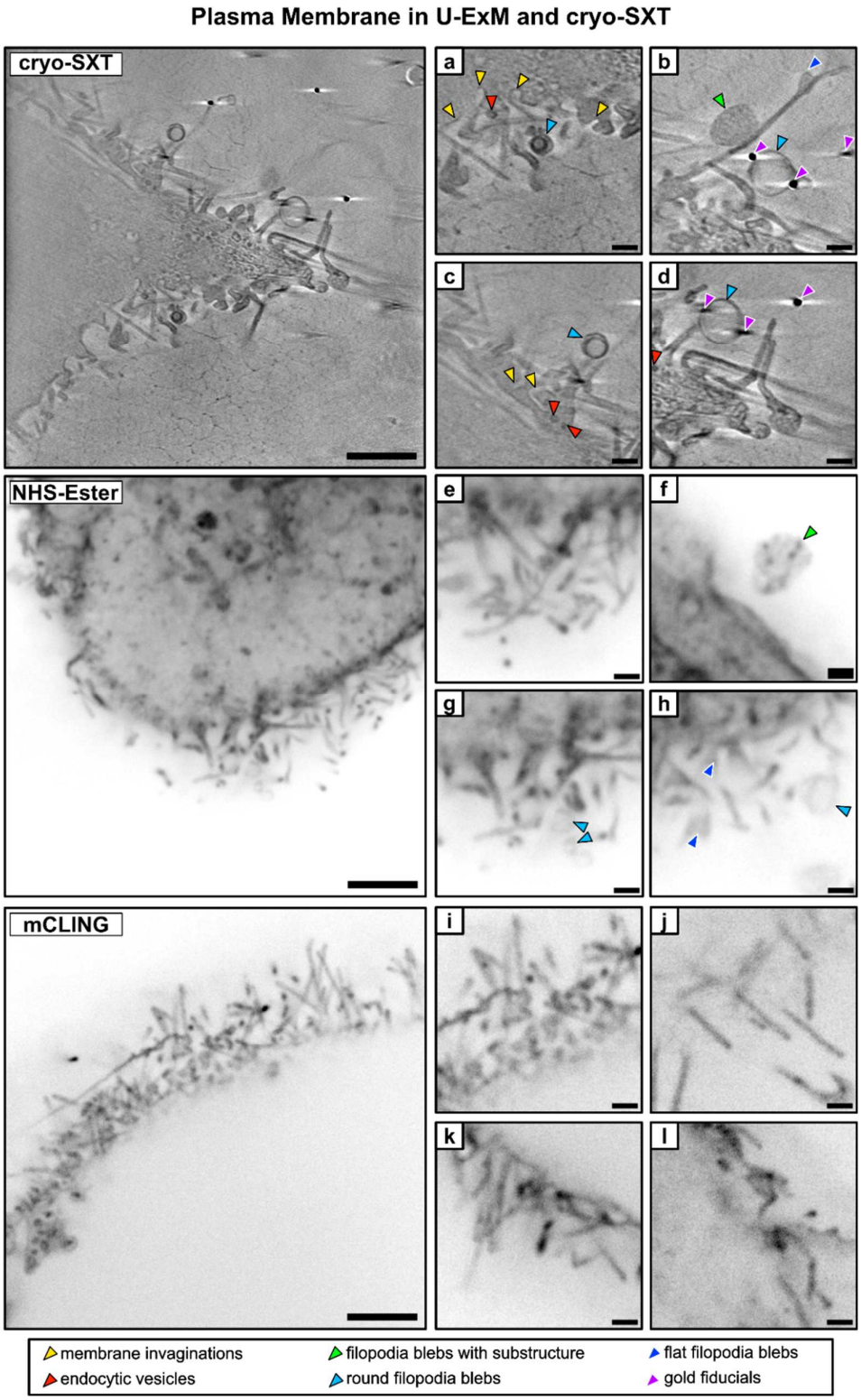

Figure 3-5: Global Stainings with NHS-ester or Fixable Lipid Dyes Effectively Visualize the Plasma Membrane. Cryo-SXT: Shown are representative minimum Z-projections of 10 consecutive tomographic slices. The small panels a-l show magnified areas of either the same datasets shown on the left, or from comparable datasets prepared under the same conditions. Scale bars large panels: 2 µm. Small panels: 500 nm.

3.3.3.2. Nucleus

The nucleus is typically the largest organelle in the cell and can easily be identified and visualized in cryo-SXT. However, its size can also pose a problem, as it can fill most of the field of view in an acquisition. Its high absorption can reduce the contrast of cytoplasmic organelles positioned on its left or right as seen from the tilt axis. The focus of this work was not on the nucleus and its substructure and for this reason, only a part of the nucleus was contained in the X-ray data. However, the dataset shown below in figure 3-6 illustrates a representative example regarding some of the structural features that can be observed in nuclei of CRFK and Vero E6 cells in cryo-SXT. No clear ultrastructural differences between Vero E6 cells and CRFK cells were observed. The most prominent feature of the nucleus in cryo-SXT apart from the nuclear envelope is the nucleolus. In some rare instances, the outer nuclear membrane was detached from the inner membrane, forming membrane blebs. The visualization of such blebs, as well as other structural features such as nuclear membrane channels has been described in detail by McNally et al. for cryo-SXT[90].

In U-ExM, the nucleus and its substructures were visualized effectively by NHS-ester stains, membrane stains and even lectin stains. Interestingly, NHS-ester and membrane stains highlight chromatin substructures that could not be observed in this detail in cryo-SXT (see fig. 3-6, panel b-e). Other features, such as smaller granular chromatin structures or even nuclear membrane channels can also be found in both stainings as well as in cryo-SXT (blue and red arrows in panels b-e). The nuclear membrane channels are especially difficult to efficiently screen for in cryo-SXT or EM. In contrast, they were found several times in U-ExM, due to the higher imaging speed and contrast possible by FM techniques. One example is highlighted by blue arrows in panels d and e.

On top of visualization by global stainings such as NHS-esters and fixable lipid dyes, the nucleus could also be visualized by wheat-germ agglutinin (WGA) staining. In particular the nuclear pore complexes could be observed as punctate patterns on the outline of the nucleus. While such puncta can also be found in NHS-ester and membrane stains (yellow arrows in panel c, d), WGA staining highlights the NPCs very clearly (panels f, g). In comparison, no NPCs could be observed in cryo-SXT data of any cell type throughout the experiments related to this thesis.

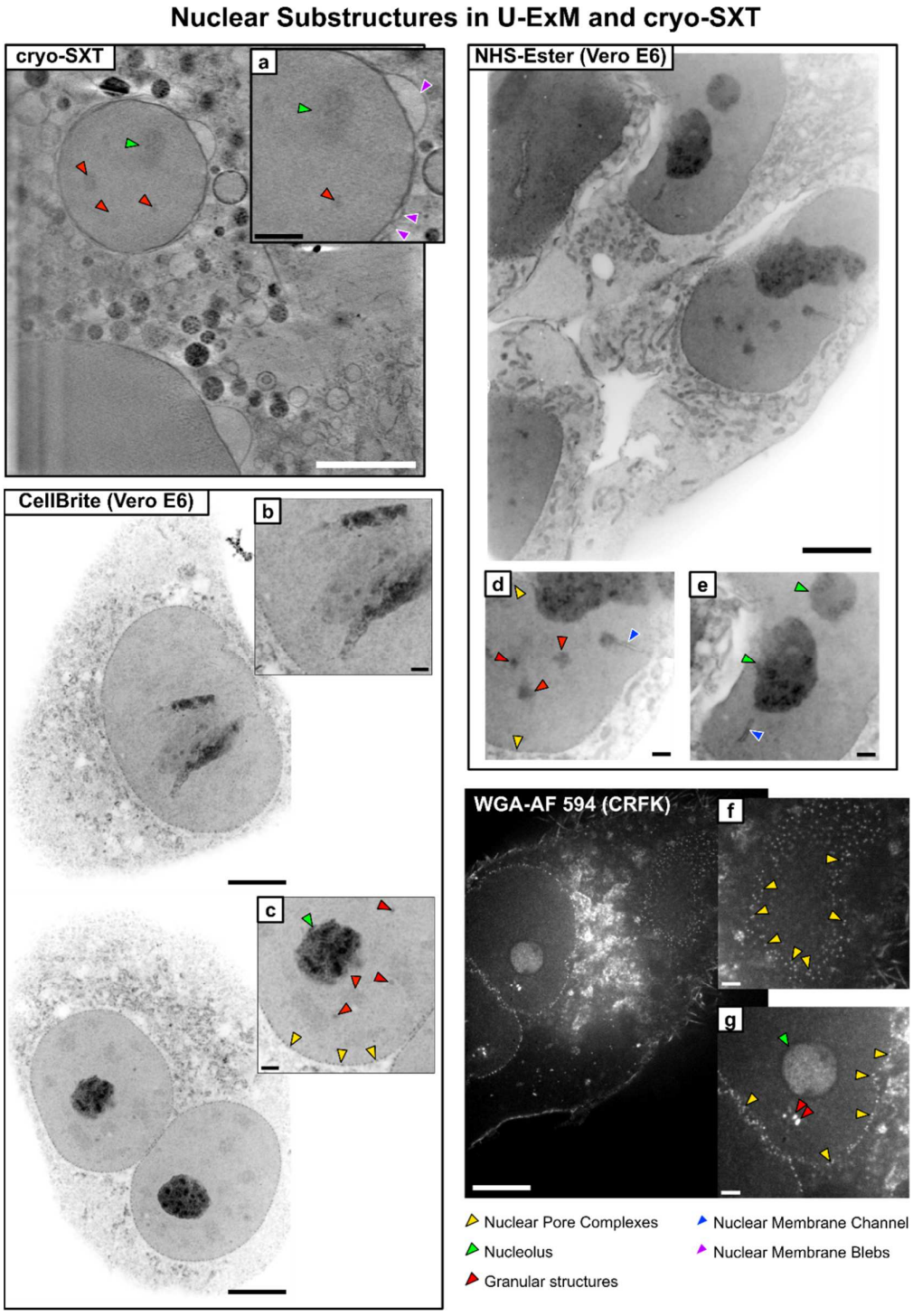

Figure 3-6: Comparison of Substructure Visualization of Nuclear Features in cryo-SXT and U-ExM. Cryo-SXT visualizes the granular substructure in the nucleus, as well as the nucleolus and the nuclear envelope. In CRFK cells, nuclear membrane blebs can also be observed but are overall very rare. The cryo-SXT image is a minimum Z-projections of 10 consecutive tomographic slices. In U-ExM, nuclear substructure is often co-stained, as indicated by the arrows highlighting multiple features. The outline of the nucleus can be inferred based on staining of nuclear pore complexes by WGA-staining, which also stains the nucleolus and other granular structures. Scale bars: large cryo-SXT panel: 3 µm. Large WGA, CellBrite™ and NHS-Ester panels: 5 µm. Small panels: 1 µm.

3.3.3.3. Mitochondria

Mitochondria are easily identifiable in cryo-SXT, thanks to their high absorption and characteristic cristae, which stand out very clearly (yellow arrows in fig. 3-7). Towards top and bottom of mitochondria, the cristae became more difficult to distinguish in cryo-SXT (fig. 3-7, red arrows), which is a consequence of the missing wedge problem.

In U-ExM, NHS-ester stains and membrane stains succeed in visualizing mitochondria, which can usually be clearly identified as such from the other cellular components based on their higher labeling density and their preserved morphology. However, visualization of cristae is not as robust, due to the high background signal of either staining. Examples of various stainings are shown below. No clear difference between mitochondria in CRFK and Vero E6 cells in cryo-SXT or U-ExM was observed.

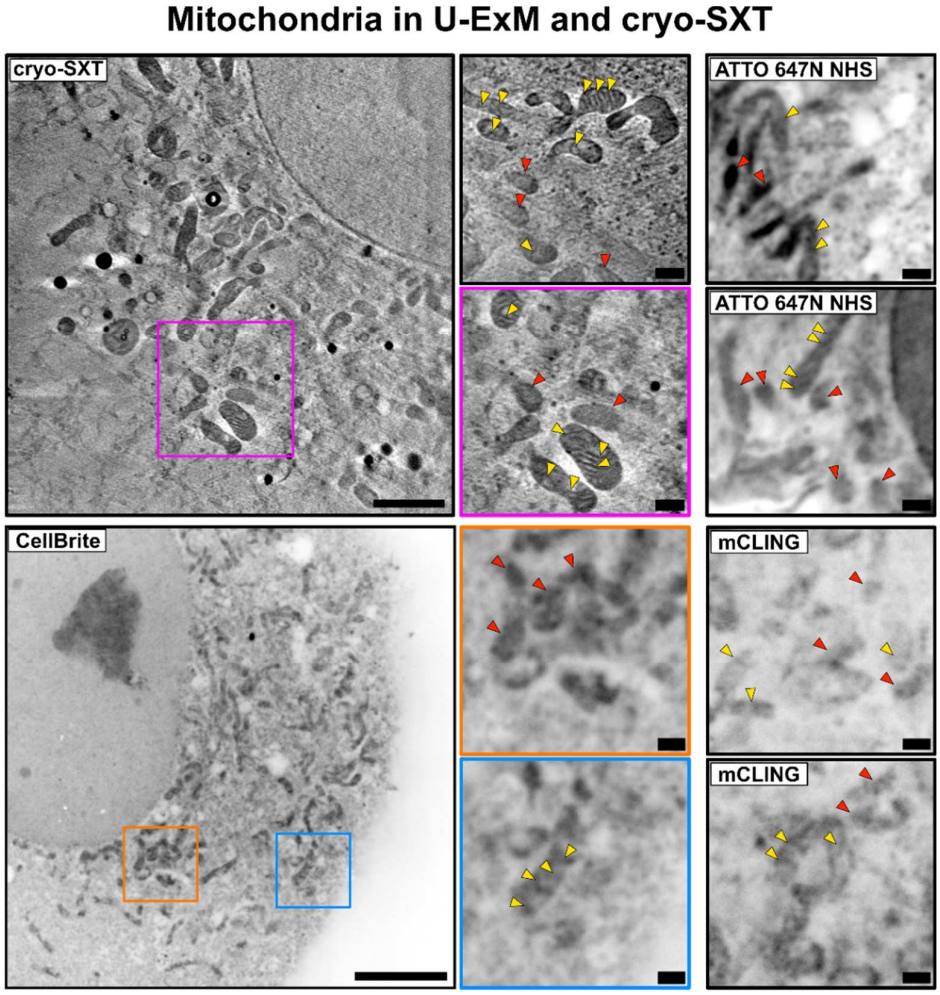

Figure 3-7: Comparison of Mitochondria Visualization in Vero E6 Cells by cryo-SXT and U-ExM. Yellow arrows indicate cristae, red arrows indicate mitochondria without clearly discernable cristae. Shown are representative minimum Z-projections of 10 consecutive tomographic slices. Scale bars: large cryo-SXT panel: 2 µm. Large CellBrite panel: 5 µm. Small panels: 500 nm.

3.3.3.4. Endoplasmic Reticulum

Despite the remarkable extent to which the ER can span across the cell volume, it is surprisingly difficult to fully capture by cryo-SXT. Its fine structure will not be visualized well in data with focus drift or misalignment and even in high-quality datasets, structure representation is often limited to tubular ER. Below are shown examples from CRFK cells (fig. 3-8, panels a-d) and Vero E6 cells (panels e-h), with some ER structures highlighted with arrows: tubular structures (green arrows), flat ER structures (yellow arrows), and parallel structures (red arrows).

In U-ExM, the ER is difficult to clearly discern from other features and overall cytosolic background staining in the cell in global NHS-ester or membrane stains. Only tubular ER structures were clearly identifiable as such in NHS-ester or membrane stainings (panels i, j). Moreover, it could at times be hard to distinguish them with certainty from thin mitochondria, when their cristae were not clearly resolved. Staining with concanavalin A (Con A, panels k, l) allowed more selective visualization of the ER in the cell and turned out to be a more robust proxy for tracing the ER structures in the cellular volume. Stainings with Con A are not limited to ER membranes but also visualized outlines of nucleus and, to a lesser extent, the plasma membrane.

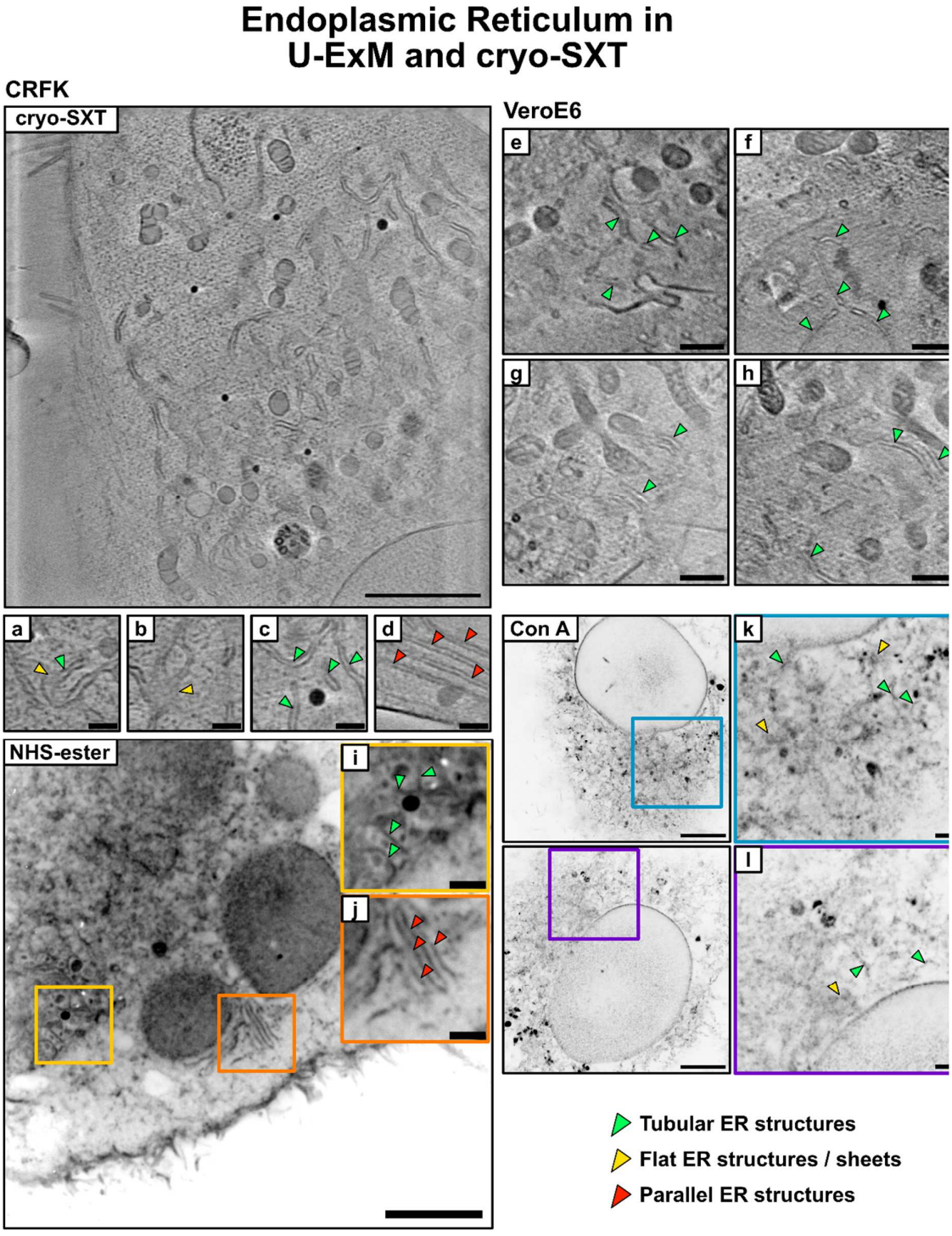

Figure 3-8: The Endoplasmic Reticulum as Visualized by cryo-SXT and U-ExM in Vero E6 and CRFK Cells. Global NHS-ester staining reveals some ER structures as clearly identifiable (highlighted by insets), however the overall structure remains difficult to discern from other organelles. Concanavalin A staining (bottom right) highlighted the structure of the ER much more clearly. Cryo-SXT panels are minimum Z-projections of 10 consecutive tomographic slices. Images on the left half of the figure are from CRFK cells, images on the right half from Vero E6 cells. Scale bars: Large Con A and NHS ester panels: 5 µm. Large cryo-SXT panel: 3 µm. Panels a-d: 500 nm, e-l: 1 µm.

3.3.3.5. Golgi Apparatus

The Golgi apparatus is also a challenging structure for visualization in cryo-SXT, which can only be found in high-quality datasets. Generally, it has been easier to identify the Golgi apparatus in Vero E6 cells than in CRFK cells, due to the lower background of the cytoplasm and flatter shape of the cell. Even in Vero E6 cells, it can still be difficult to discern it clearly from nearby organelles in a crowded region of the cell (see fig. 3-9, panels b, d).

Similarly, it was difficult to identify the Golgi apparatus in NHS-ester or membrane stains, due to the abundance of stained features in its surrounding. Nonetheless, it was possible to visualize the Golgi apparatus in CRFK and Vero E6 cells with WGA conjugated with Alexa® Fluor 594 (panels a, c).

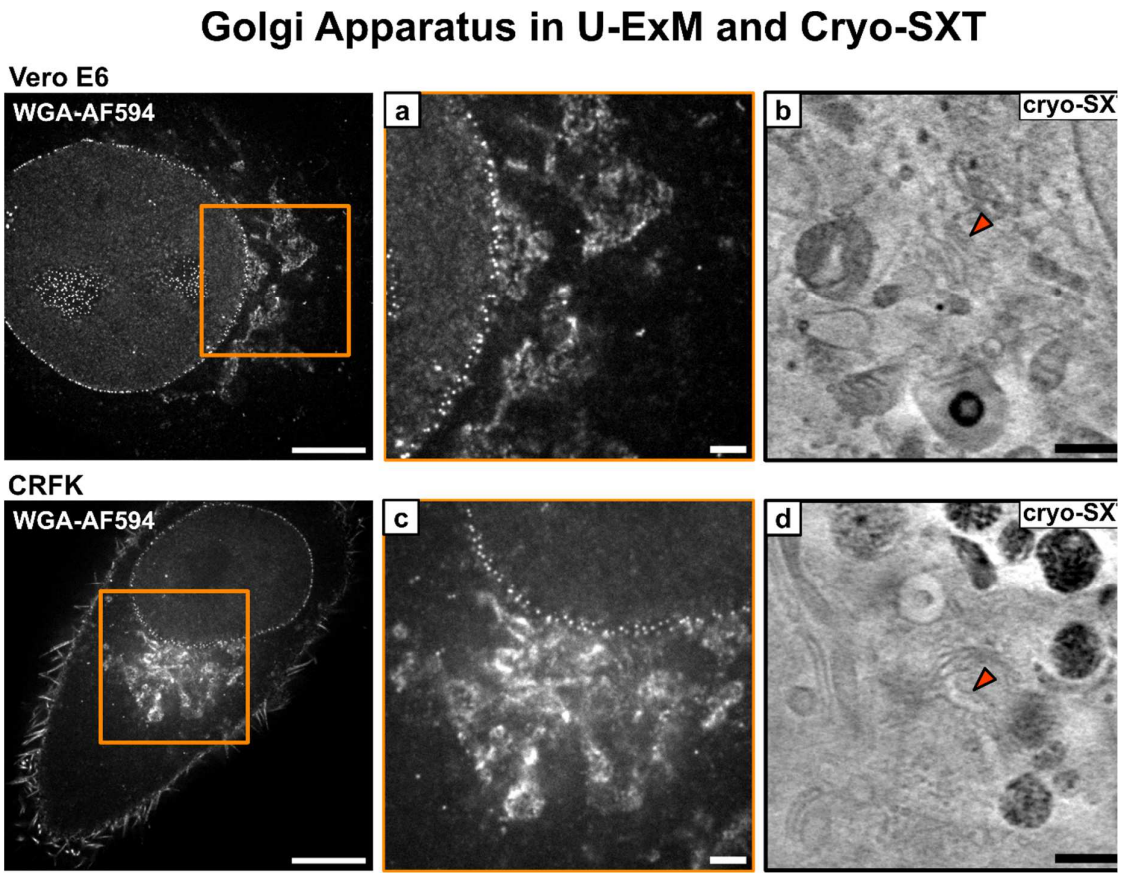

Figure 3-9: Fluorescently Labeled Wheat-Germ Agglutinin Stains Structures of the Golgi Apparatus. Shown are examples from Vero E6 and CRFK cells on the left. The orange boxes highlight the areas shown magnified in the middle column. The right side shows examples of the Golgi apparatus as visualized by cryo-SXT (red arrows). The cryo-SXT panels are minimum Z-projections of 10 consecutive tomographic slices. Scale bars: left panels 5 µm. Panels a-d: 1 µm.

3.3.3.6. Vesicular Structures

Mammalian cells can be filled with a striking variety of vesicular structures: Endosomes, macropinosomes, multivesicular bodies, lysosomes, autophagosomes, lipid droplets and more. In cryo-SXT, the size, substructure and absorption contrast can serve to distinguish and identify the different kinds of organelles as shown in figure 3-10, panels a-q. In NHS-ester and membrane stains in U-ExM, it proved very difficult to distinguish this variety of vesicular structures to the extent that was possible in cryo-SXT.

Lysosomes are readily distinguishable in cryo-SXT based on their high absorption and substructure consisting of several smaller vesicles that could also be similarly stained by ATTO® 647N NHS-ester in U-ExM in both cell types (figure 3-10, panels m-q vs. panels s, v, z). However, in some experiments, this substructure had not been stained or preserved in cells for reasons unknown. Therefore, me and my student Ms. Jasmin El-Khabbaz performed antibody stains for late endosomal/lysosomal markers such as LAMP-1, LAMP-2 or LBPA to complement NHS-ester stains and confirm identification of lysosomes. Unfortunately, despite extensive testing of several antibodies, none produced sufficient signal in expanded samples.

Other vesicular organelles were much harder to identify and distinguish with confidence. For instance, the substructure of multivesicular bodies was clearly visible in cryo-SXT (panels d-g) but could not be revealed in any experiment in U-ExM with either NHS-ester or membrane stains. More generally, substructures of vesicular organelles were often not stained or preserved clearly enough for identification and in most instances, vesicular structures could be seen rather as spherical shapes with less signal than the cytoplasm surrounding them (panels r, u, x), which complicated their specific identification.

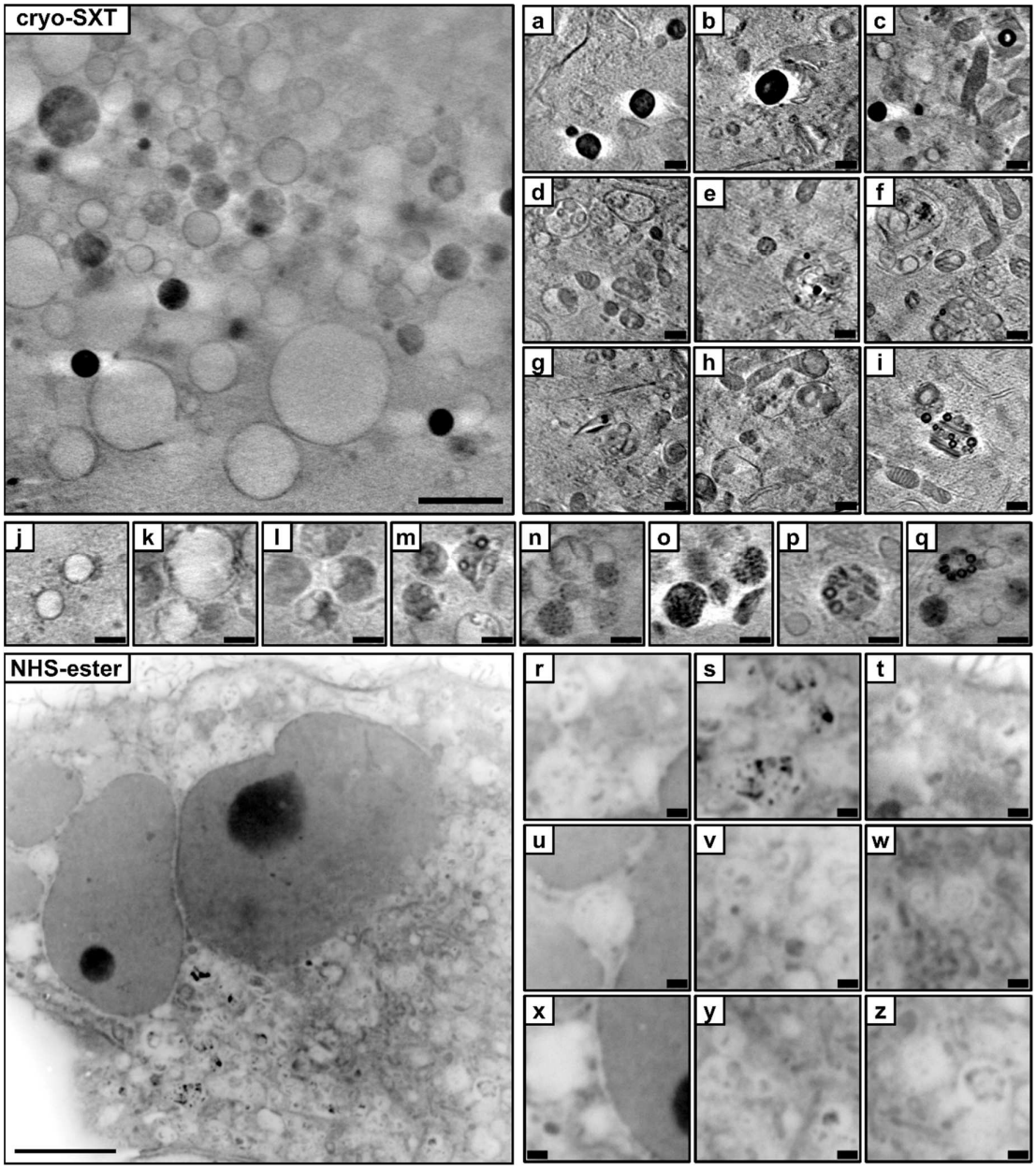

Figure 3-10: Overview of Different Vesicular Structures Visualized by cryo-SXT in CRFK and Vero E6 Cells. Cryo-SXT panels illustrate how different vesicles can be distinguished from one another based on their absorption properties and substructure. The large overview panel on the left was acquired with a 40 nm FZP, all others were acquired with a 25 nm FZP. Panels a-i are from Vero E6 cells, panels j-q from CRFK cells. All cryo-SXT panels are minimum Z-projections of 10 consecutive tomographic slices. Shown below is an example of a CRFK cell expanded by U-ExM and stained with ATTO 647N NHS-ester. Panels r-z show more examples from NHS-ester stained CRFK cells expanded by U-ExM. Scale bars: large cryo-SXT panel: 2 µm. Large NHS-ester panel: 5 µm. All other panels: 500 nm.

The observations of organelle visualization by cryo-SXT and U-ExM are summarized in table 3-1.

Table 3-1: Comparison of the Visualization of Different Organelles in cryo-SXT and U-ExM.

ORGANELLE	CRYO-SXT	U-EXM
PLASMA MEMBRANE	• High structural information content in focus volume • Missing wedge artifacts of nearby fiducials can mask features. • Cell overlaps are challenging.	• With 4.5x expansion factor, the entire cell surface of single cells can be covered in one FOV. • Finer substructures often obscured by high background signal.
NUCLEUS	• May fill entire FOV, limited information of remaining cell. • Heterochromatin, blebs and membrane channels can be visualized, but NPCs and chromatin substructure are more challenging.	• Stained by NHS-ester, lipids, and lectins. • Large FOV enables visualization of nucleus and cell volume without stitching. • NPCs and chromatin substructures can be visualized clearly.
MITOCHONDRIA	• Easily identifiable. Cristae clearly stand out in most datasets. • Mitochondria out of focus can still be identified.	• Mitochondria networks can be visualized clearly by NHS-ester and membrane stains. • Visualization of cristae possible but not as robust as with cryo-SXT.
ENDOPLASMIC RETICULUM	• The full extent of the ER network and its morphology difficult to capture by cryo-SXT. • Tubular structures can be seen in high-quality datasets. Sheets are very rarely visible.	• In NHS-ester and membrane stains, tubular structures can be identified as ER. For finer structures, Con A staining can reveal more detail. • Visualization of the ER network in the entire cell volume possible.
GOLGI APPARATUS	• Requires high sample quality and good alignment for visualization in tomograms. • Difficult to discern in crowded environments.	• Difficult to identify with confidence in NHS-ester or membrane stains. • WGA stains *trans*-Golgi apparatus[231,232]. Other labels could be used in support.
VESICULAR STRUCTURES	• Different classes of vesicles, including lipid droplets, lysosomes and multivesicular bodies are clearly identifiable and visualized at high resolution.	• In the absence of specific markers or preserved substructure, classification of vesicle classes is difficult. • Lipid-dense organelles are rarely preserved.

3.3.4. Visualization of Drug-Induced Ultrastructural Alterations by U-ExM

U-ExM is an attractive route to visualize the DRVs in the cellular volume independently of cryo-SXT. The cryo-SXT results from chapter 2 showed a dramatic structural reorganization of cells upon treatment with cationic amphiphilic drugs and infection with viruses. One central observation was that CRFK cells would form dark-rimmed vesicles upon treatment with the antidepressant drug fluoxetine, and that these organelles would change in size and number upon infection with FIPV. However, the limited access to cryo-SXT also underscores the need for additional, more decentralized ultrastructure screening tools, which could help optimize experimental conditions.

The TEM results shown in chapter 2 confirmed that the DRVs observed by cryo-SXT were in fact endolysosome-associated multilamellar structures. Out of the three drugs that were used for the coronavirus-related work, fluoxetine induced the largest DRVs in CRFK cells after 24 hours treatment. The width of the inner, non-membranous part of the DRVs was usually approximately a third of the total diameter (median 325 nm) and should become discernable upon four-fold expansion by U-ExM. Thus, treating CRFK cells for 24 hours with 10 µM fluoxetine or DMSO as control was the standard condition to test the DRV preservation by U-ExM.

DMSO-treated CRFK cells did not noticeably differ from entirely untreated cells (see fig. 3-11). The occasional occurrence of large vesicular structures was consistent with our observations by cryo-SXT in untreated, fixed cells (fig. 3-10) and the presence of substructure in many of these organelles suggested preservation of actual morphology instead of artifacts (see green arrows fig. 3-11, i-iv). Upon treatment with 10 µM fluoxetine for 24 h, many more of such large vesicles could be observed already under the cell-culture microscope prior to fixation, as well as after U-ExM processing and expansion of NHS-ester-stained cells (see fig. 3-12 A).

Under my supervision, an undergraduate student, Ms. Jasmin El-Khabbaz, optimized the staining of fluoxetine-treated CRFK cells. In drug-treated, NHS-ester-stained cells, she frequently observed high-intensity puncta in NHS-ester-stained cells, which were surrounded by an unstained rim (fig. 3-12 B-D, panels i-iv). Since these structures resembled the DRVs observed by cryo-SXT in size and number, we hypothesized that the NHS-ester had stained the interior of the DRVs and that fixable membrane dyes could stain the multilamellar membrane rim and therefore tested a series of membrane dyes: CellMask™, mCLING, Cellbrite® Fix, and FM™ 143-FX. In all cases, staining the rim of these puncta proved difficult and of all these dyes, Cellbrite® Fix yielded the best results (see fig. 3-13). Still, in rare instances, a stained rim could be observed (fig. 3-13 D), but it was never possible to distinguish individual membrane layers of the multilamellar structures.

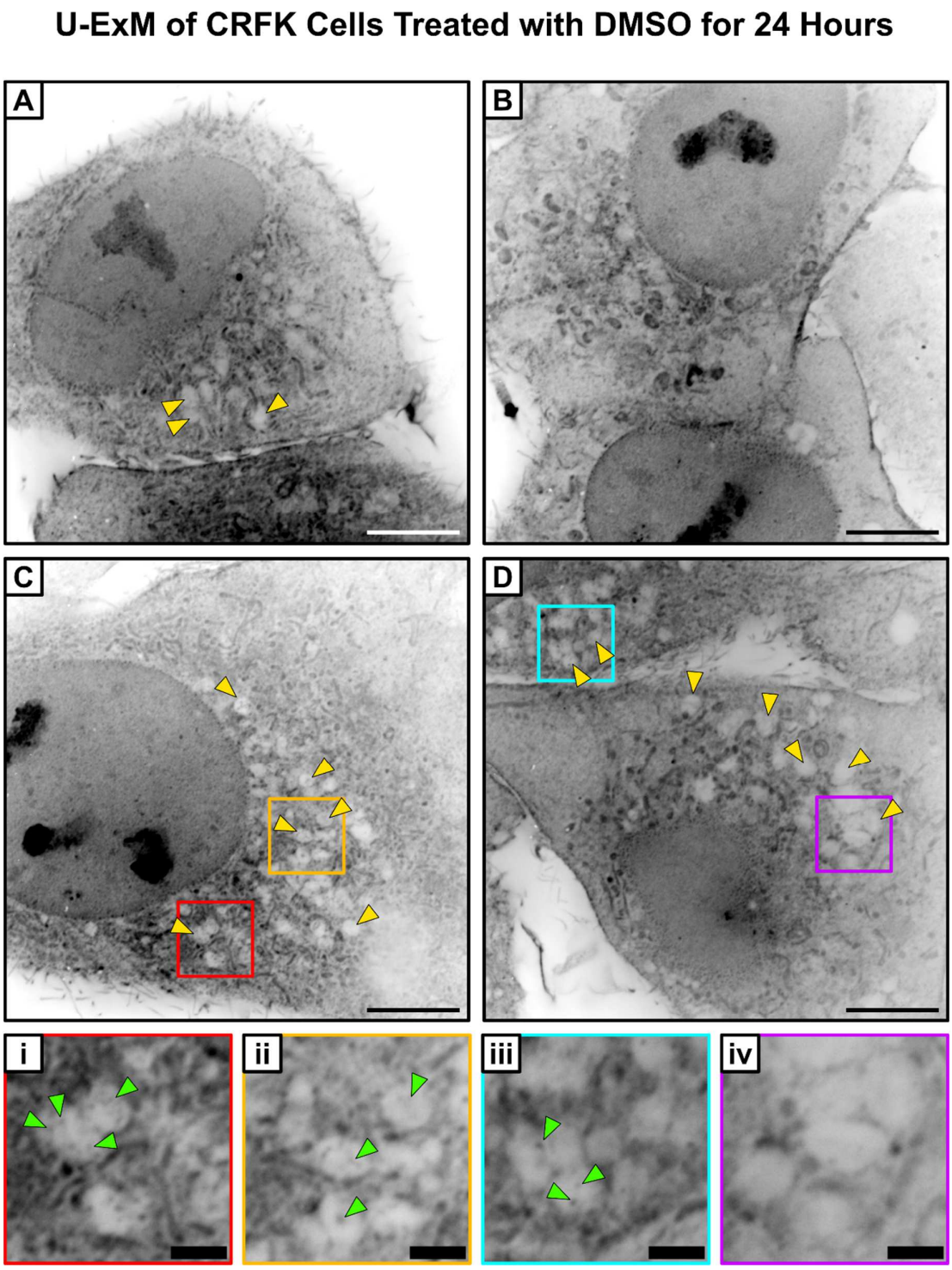

Figure 3-11: U-ExM of DMSO-treated CRFK Cells Stained with ATTO® 647N NHS-ester. Shown are representative examples of CRFK control cells, treated for 24 h with DMSO prior to NHS-ester staining and U-ExM processing. Large vesicles were occasionally observed in these cells (yellow arrows) and often contained a substructure (green arrows). The colored boxes show the areas magnified in i-iv. Scale bars (corrected for 4.8x expansion factor): A-D: 5 µm. i-iv: 1 µm.

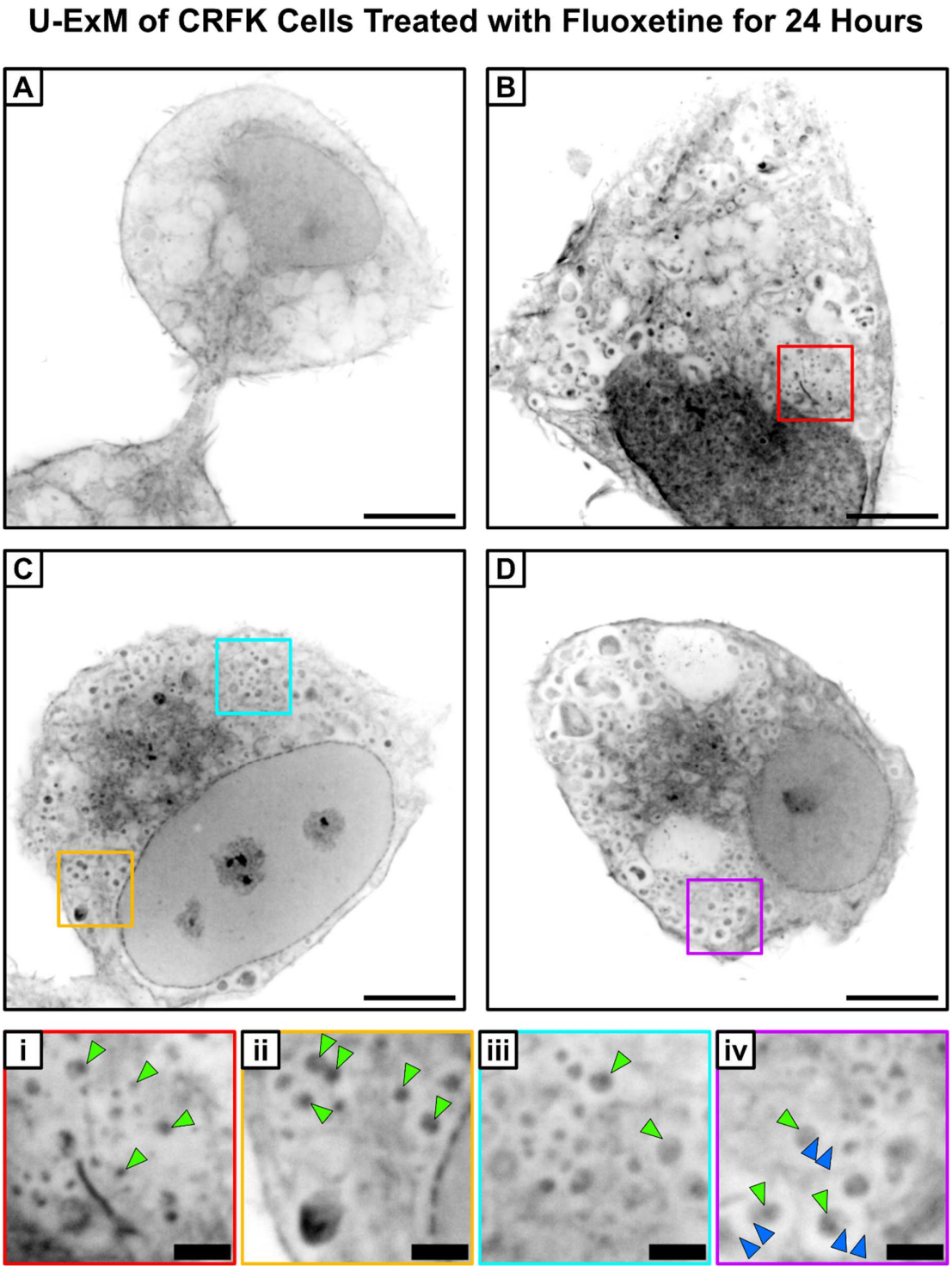

Figure 3-12: U-ExM of CRFK Cells Treated with 10 µM Fluoxetine for 24 h and Stained with ATTO® 647N NHS-ester. NHS-ester staining of fluoxetine-treated cells routinely visualized high-intensity puncta (green arrows) surrounded by a low-intensity rim (blue arrows). The colored boxes show the areas magnified in i-iv. Scale bars (corrected for 4x expansion factor): A-D: 5 µm. i-iv: 1 µm. Data shown in this figure was produced by Ms. Jasmin El-Khabbaz.

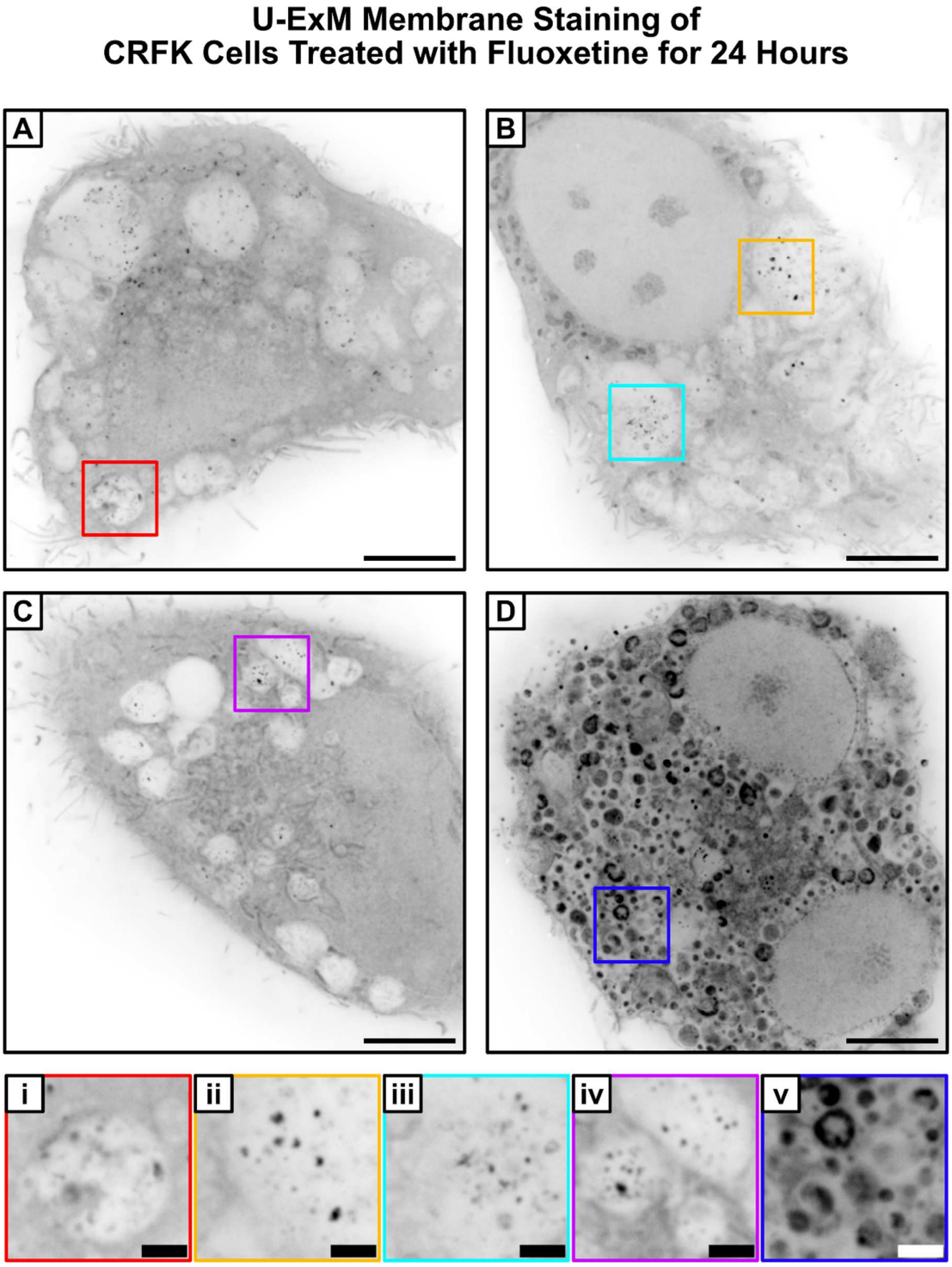

Figure 3-13: U-ExM of CRFK Cells Treated with 10 µM Fluoxetine for 24 h and Stained with CellBrite® Fix 640. Staining with fixable CellBrite® Fix membrane dye provided the most robust membrane stain of all the dyes tested. A-C show representative examples and D shows one of the rare instances of clear preservation of high-intensity rims in a cell from the same specimen. Colored boxes show the areas magnified in i-v. Scale bars (corrected for 4x expansion factor): A-D: 5 µm. i-iv: 1 µm. Data shown in this figure was produced by Ms. Jasmin El-Khabbaz.

3.4. Discussion

The central question of the work related to this chapter was whether ExM could be used interchangeably or complementarily with cryo-SXT to analyze cellular ultrastructure at high resolution. Out of the many ExM variations available, the U-ExM protocol was chosen on the grounds that it was the most robustly performing method established in our laboratory.

The experiments in this chapter were predominantly based on global stains, such as NHS-ester or membrane stains, which revealed a remarkable degree of structural information about the overall cellular architecture in a single channel with a single staining procedure. For example, the nucleus and its substructures, mitochondria and their cristae, and the plasma membrane were effectively visualized using only a confocal spinning disk fluorescence microscope. Even if the resolution does not match the resolution of cryo-SXT, the potential use of U-ExM for the analysis of cellular ultrastructure was clearly illustrated.

Besides the visualization of the cellular architecture, global stains proved to be essential in identifying artifacts in the sample preparation, as was illustrated with several examples. The occurrence of artifacts was the most significant problem in the U-ExM experiments in this work. Some artifacts were easily identified, such as unequal expansion of the cytosol and the nucleus or formation of membrane patches. It is likely that such defects can be managed effectively by a consistently higher quality of sodium acrylate stocks. The more systematic artifacts, such poor preservation of lipid-dense organelles and small polymerization defects will need to be considered during any experimental design and analysis. While tandem pre- and post-expansion imaging if often used to control for anisotropic expansion or distortions[216,221,222,233,234], it is important to note that diffraction-limited, pre-expansion imaging of global stains will not be sufficient to identify such small artifacts. Without additional, specific markers, it will likely be impossible to distinguish small cellular features from small artifacts.

However, for detailed ultrastructural analysis by U-ExM, relying exclusively on global stains may prove insufficient. The global stains consistently produced a high degree of background staining, which was to the clear disadvantage of small cellular features, especially in more densely packed cellular regions. At times the substructure of stained organelles (e.g. cristae in mitochondria) could not be discerned clearly from the high background. The contrast and organelle substructures are important hallmarks for identification of organelles or artifacts. The difficulties therein became especially clear in the case of vesicular structures, which could often not be clearly distinguished from gel defects with confidence in neither NHS-ester nor membrane stains.

Therefore, it is prudent to combine global staining with specific labeling against structures of interest.

In U-ExM, complementing a global stain with more specific ones such as Con A, WGA or antibodies could add specificity to the contextual information provided by global stains. Combining multiple stains in the same sample to visualize several kinds of organelles alongside each other can, in principle, be performed relatively straightforwardly in ExM[224], provided that the fluorescent labels applied can withstand the ExM sample preparation[224,230]. On the one hand, this latter point is not trivial, as antibodies that provide clean staining in regular immunofluorescence may not be suitable for staining in U-ExM, which is a known problem in the field[235,236]. This was also observed repeatedly during our attempts to stain lysosomal structures with antibodies in U-ExM. In combination with the high quantities of antibody needed for staining a gel, extensive antibody optimization for U-ExM can turn into a costly undertaking. On the other hand, if successful, such combinatorial use of global and specific staining procedures can be useful assets to test hypotheses, that would otherwise require correlative techniques with significantly lower throughput and higher technological requirements such as correlative light and electron or X-ray microscopy (CLEM or CLXM, respectively). However, ultrastructural findings based on U-ExM will require further validation by high-resolution microscopy techniques that do not rely on the denaturation and physical alterations of the original structure. The formation of artifacts in U-ExM documented in this thesis further illustrates the benefit of near-native 3D imaging offered by cryo-SXT.

These considerations strongly suggest a potential use of U-ExM as an accessible screening tool for general ultrastructural alterations under given experimental conditions. The formation of artifacts and the difficulty to accurately visualize lipid-rich organelles are important caveats of the technique, which can be addressed effectively by near-native imaging in cryo-SXT. This point was illustrated by CRFK cells treated with the antidepressant drug fluoxetine. The experiments described in chapter 2 showed formation of lysosome-associated multilamellar bodies upon treatment with this or related drugs. Additional ultrastructural experiments were needed to investigate a potential link of these ultrastructural alterations and the observed antiviral effect of these structurally related drugs. Fluoxetine-treated CRFK cells were the best-characterized and simplest system to test preservation of these multilamellar, dark-rimmed vesicles by U-ExM.

NHS-ester staining of drug-treated versus control cells did show a clear change in cellular morphology. High-intensity puncta surrounded by an unstained rim could be observed much more frequently and in higher numbers than in DMSO-treated control cells. The size and

abundance of these organelles matched the DRVs that were observed in cryo-SXT in fluoxetine-treated, uninfected cells (see previous chapter). The puncta stained by NHS-ester are likely the hardly absorbing inner part of the DRVs and the unstained rim in the U-ExM data would be the equivalent to the stacked membranes forming the dark rim of the DRVs observed in cryo-SXT. To test this assumption, a series of fixable membrane dyes were used in an attempt to stain the membrane layers of the DRVs. Unfortunately, despite extensive testing of different fixation and staining protocols, these membrane layers proved very challenging to stain robustly and only in rare instances could stained rims be preserved in U-ExM. It appears that the original multilamellar structure is difficult to anchor properly to the hydrogel matrix, such that the containing lipids are washed out during the heat denaturation step. This would also explain why lipid droplets were practically never observed in any staining performed in my work, even if they were clearly visible in cryo-SXT.

It is also remarkable that the ATTO® 647N dye used for the NHS-ester staining could enter and stain the inner part of the DRVs but did not stain any space between the membrane sheets, where for instance membrane proteins could be present. It is possible that the membrane sheets are packed too densely for accumulation of protein in sufficient amounts for labeling or effective cross-linking.

Since the membrane rim of these drug-induced organelles could not be robustly preserved by U-ExM, nor by TREX or Magnify by me or my colleague Dr. Chethana, it was not possible to extract precise information on the size of these organelles in comparison to the results by cryo-SXT. However, NHS-ester staining of fluoxetine-treated CRFK cells did clearly show the formation of organelles induced by the drug, as it was observed in cryo-SXT and TEM analysis. This clearly underlines a benefit of U-ExM as a readily implemented technique, which can be used to visualize general ultrastructural alterations in cells. Even if the full extent and detail of the drug-induced alterations could not be visualized in this case, such information can already be useful in further characterizing and optimizing the experimental system.

Taken together, the results of this and the previous chapter illustrate several strengths and weaknesses of each technique, which suggest a complementary use of both. Table 3-2 summarizes a comparison of both techniques based on the experience accumulated during the work related to this thesis using both techniques. Several key points are highlighted below.

Table 3-2: Comparison of cryo-SXT and U-ExM Regarding Their Performance Under Important Experimental Aspects.

	CRYO-SXT	EXM (U-EXM)
SIZE LIMITATION	• < 15 µm, single cells, monolayers.	• Cultured cells, tissues, small organisms[220,223,234]. • Working distance of microscope.
SAMPLE PROCESSING	• Vitrification. • Possible: chemical fixation.	• Required: fixation, anchoring, gelation, denaturation, expansion, staining.
FIELD OF VIEW	• 25 nm FZP: 12 x 12 µm (sub-region of a cell).	• With 4.5x expansion factor usually one entire cell.
ACQUISITION SPEED	• 30 - 60 min per tomogram.	• Depending on no. of channels, < 5 min.
ARTIFACTS	• Missing wedge. • Limited depth of focus.	• Uneven expansion across the sample. • Embedding artifacts (lipid anchoring) • Tears in gel.
CONTRAST GENERATION	• Intrinsic absorption contrast. • Correlative microscopy possible[55,102].	• Possible combination of multiple labels: NHS-ester, membrane dyes, specific stains (e.g. antibodies, lectins)[220,221,237].
STRUCTURES EFFECTIVELY VISUALIZED	• Any carbon-dense structure. • Fine details of 3D-organization of cytosol or plasma membrane. • Mitochondria. • Differentiations of subclasses of vesicular structures.	• Overall morphology of the cellular volume in 3D. • ER, nucleus substructures. • Cytoskeleton[218,237,238].
CHALLENGING STRUCTURES	• ER sheets, Golgi apparatus, cytoskeleton.	• Small vesicular structures • Lipid-dense organelles such as lipid droplets or MLBs.
PITFALLS	• Observation of rare morphologies can be misleading due to limited throughput and low statistical power.	• Artifacts through sample processing. • Careful monitoring of artifacts necessary. • Unstained or unpreserved features will be missed.

Cryo-SXT:

Central **advantages** of cryo-SXT are its ability to produce high-resolution 3D ultrastructural data under near-native conditions with minimal sample processing. The occurring artifacts such as missing wedge or irradiation damage are well-known and readily identifiable, meaning that the data can be interpreted with high confidence. Even small organelles can be distinguished from another based on their morphology and absorption properties.

The major **disadvantage** of cryo-SXT is that fact that it is still a highly centralized technique, meaning that time at the microscope is the most limiting factor and does not allow acquisition of extensive pools of data. A relatively small field of view of 12 x 12 µm (with a 25 nm FZP) often forces users to prioritize cellular sub-regions of interest and further limits the throughput of the technique. With such limited time and throughput, it is difficult to optimize an experimental system or to quantify rare observations in a statistically meaningful way with cryo-SXT alone.

U-ExM:

Key **advantages** of U-ExM and other ExM techniques are their versatility, accessibility, and low technical requirements. The sample handling itself and the preparation procedures do not require extensive training or experience and, importantly, the data acquisition can be performed on microscopy equipment available in-house at many life sciences institutions. Therefore, image acquisitions can be performed very independently and with much higher throughput, which can help to efficiently optimize experimental conditions. As shown in this chapter, staining with NHS-esters can already reveal a significant amount of ultrastructural detail for cells. Combination with more specific labels such as antibodies can help to study specific structures in the context of the global cellular ultrastructure. Another advantage is, that ExM is not limited to thin samples the way cryo-SXT currently is. In fact, a variety of ExM protocols have been implemented for use in complex samples such as tissues[217,220,239] or whole multicellular organisms[234], both of which are currently not possible to image by cryo-SXT.

The most important **disadvantage** of ExM is the extensive sample processing, which, as the results in this chapter show, can lead to the formation of many artifacts. The puncta surrounded by an unstained rim observed in drug-treated, expanded CRFK cells are an example of the difficulty of interpreting U-ExM data on their own. In absence of membrane stains of the multilamellar structures, it is difficult to determine the nature of these structures in absence of additional ultrastructural information acquired by, for instance, cryo-SXT and TEM. Tracing formation of such artifacts may be possible during the sample preparation process, but will also

be hindered by the diffraction limit, especially for small organelles. While future developments in the field will certainly improve structure preservation further, it is highly likely that ultrastructural findings will need to be validated by another technique under near-native conditions, such as cryo-SXT. A second difficulty in ExM is to accurately determine whether the entire sample has actually been expanded homogenously throughout the process. Researchers in the field use pre- and post-expansion imaging[216,240], distortion maps[219,221,230] and nano-rulers[233] as strategies to determine this. Another important tool would be to know accurately the spatial dimensions of multiple organelles. The application of cryo-SXT for this problem was demonstrated with the sizes of dark-rimmed vesicles in chapter 2. The following chapter addresses this issue again with filopodia.

3.5. Conclusion

The key limitations of cryo-SXT are its very limited throughput and access and its key strengths are the intrinsically high contrast and minimal structural invasiveness of sample preparation by vitrification. While *a priori* knowledge of occurring, ultrastructural alterations is not strictly necessary in cryo-SXT, it can still be an important contribution to use the limited beamtime more efficiently. The better characterized the biological conditions are for any acquisition, the more the potential of cryo-SXT can be harnessed to elucidate cellular ultrastructure. Such *a priori* knowledge could be acquired independently of centralized facilities like synchrotrons by using U-ExM. U-ExM itself is versatile enough to combine multiple staining techniques in the same sample and thereby highlighting particular features of interest, while also enabling visualization of the overall morphology of the cell by more global stains such as NHS-ester or membrane stains. This technique can provide faster imaging of larger numbers and volumes of cells, aiding researchers to characterize optimal sample preparation conditions and the frequency and variety of major ultrastructural changes that might occur under any given condition. However, while doing so, it is crucial to be aware of structural artifacts that may be introduced during sample preparation, leading to loss of structural information, as was shown in detail for vesicular structures. Inversely, this is also the reason why users of U-ExM and other existing and emerging ExM protocols must be critical about the structural preservation in their samples and validate any ultrastructural findings by complementary techniques, such as cryo-SXT.

These findings suggest, that the cryo-SXT community can benefit from the emergence of ExM techniques by collecting more quantitative *a priori* structural information and that the ExM community can benefit from cryo-SXT by using the extensive ultrastructural information from near-native conditions to validate and improve their technique developments and biological findings.

4. Automated Segmentation of cryo-SXT Data by Deep Learning

4.1. Abstract

Cryo-SXT as a technique allows high-resolution and quantitative 3D-visualization of cellular structures under near-native conditions at the nanoscale. However, the depth of detail contained in the tomographic data must be extracted for quantitative analysis. Data segmentation is a major bottleneck in the field, where segmenting a single dataset poses a significant time investment for the users. While manual and semi-automatic tools are available, fully automated segmentation pipelines suitable for cryo-SXT data have not been implemented. In this work, we developed a convolutional neural network (CNN) for rapid and robust fully automated segmentation of cryo-SXT data. Using semi-supervised deep learning, a CNN was trained to fully segment new and complex cryo-SXT datasets from vitrified mammalian cells within 20 minutes or less, while producing only minimal false positive labels. This enables on-the-fly data processing during the experimental time at synchrotron facilities and allows users to begin data analysis already while at the beamline.

4.2. Introduction

One central idea of volumetric microscopy approaches of biological specimens is to extract the maximum amount of accurate ultrastructural information at the highest possible resolution. Significant technological advances have been made on the instrumentation and automation for volumetric imaging, leading to higher and higher resolution, throughput, and accessible volumes. However, this wealth of visualized information also needs to be processed and analyzed to extract quantifiable data and to reach verifiable conclusions. Due to their high degree of complexity, extracting quantifiable data from large volumetric datasets of biological specimens is very challenging and has been the subject of ongoing efforts for automation.

The current bottleneck in data analysis for cryo-SXT is image segmentation, a process where the pixels (or voxels) of a dataset are assigned to labels, thus identifying them as being part of one structure or another. Manually segmenting a complex dataset is a highly time-consuming task, leading to a significant interest in automating this process. The ongoing, rapid development of artificial intelligence across disciplines has also found applications in cell biology and has already had significant impact on image processing and image segmentation of EM and fluorescence microscopy images[66,241–243]. Also, significant progress was made in segmenting cryo-SXT datasets through the development of tools such as Contour[244] or SuRVoS[245,246], which still rely on expert user input to perform segmentation tasks. Thus, there is still a need for an efficient, fully

automated deep learning platform suitable for cryo-SXT. As part of this dissertation, I collaborated with researchers from the informatics department at Freie Universität Berlin to establish a deep learning pipeline dedicated to the fully automated segmentation of cryo-SXT data from vitrified mammalian tissue culture cells.

4.3. Results

The goal of this project was to develop a convolutional neural network that can automatically segment tomograms obtained by cryo-SXT microscopes. For this work, I collaborated with Dr. Mohsen Sadeghi, who, based on my feedback, designed the network architecture, image augmentation and training pipelines with data that I produced as a microscopist at the synchrotron facility.

The network uses an augmented version of a U-Net architecture in combination with an unsupervised autoencoder to perform two-headed, semi-supervised learning. The design is illustrated in figure 4-1. The software has been made available on GitHub and is described in more detail in our publication[105]. The CNN recognizes cellular features, especially membranous outlines of organelles, and produces a stack of binary maps of labeled pixels as an output. This stack can then be imported into another image analysis software such as FIJI[247] or Microscopy Image Browser[248] for further editing or analysis. It can also be used to produce a surface reconstruction for inspection of 3D objects. The code can be operated from a python console and its performance speed per image slice does not, much unlike manual segmentation, depend on the complexity of the datasets themselves, but only on the hardware and its supporting drivers. For instance, using a NVIDIA GeForce RTX 2070 SUPER with CUDA version 11.8 and CuDNN version 8.6, the segmentation speed is approximately 2 seconds per image slice, meaning that this software can operate efficiently on consumer-grade hardware and segment a full cryo-soft X-ray tomogram within 20 minutes or less. By comparison, manually segmenting a whole cryo-SXT dataset of a mammalian cell can easily require several days or weeks, depending on the complexity of the image data.

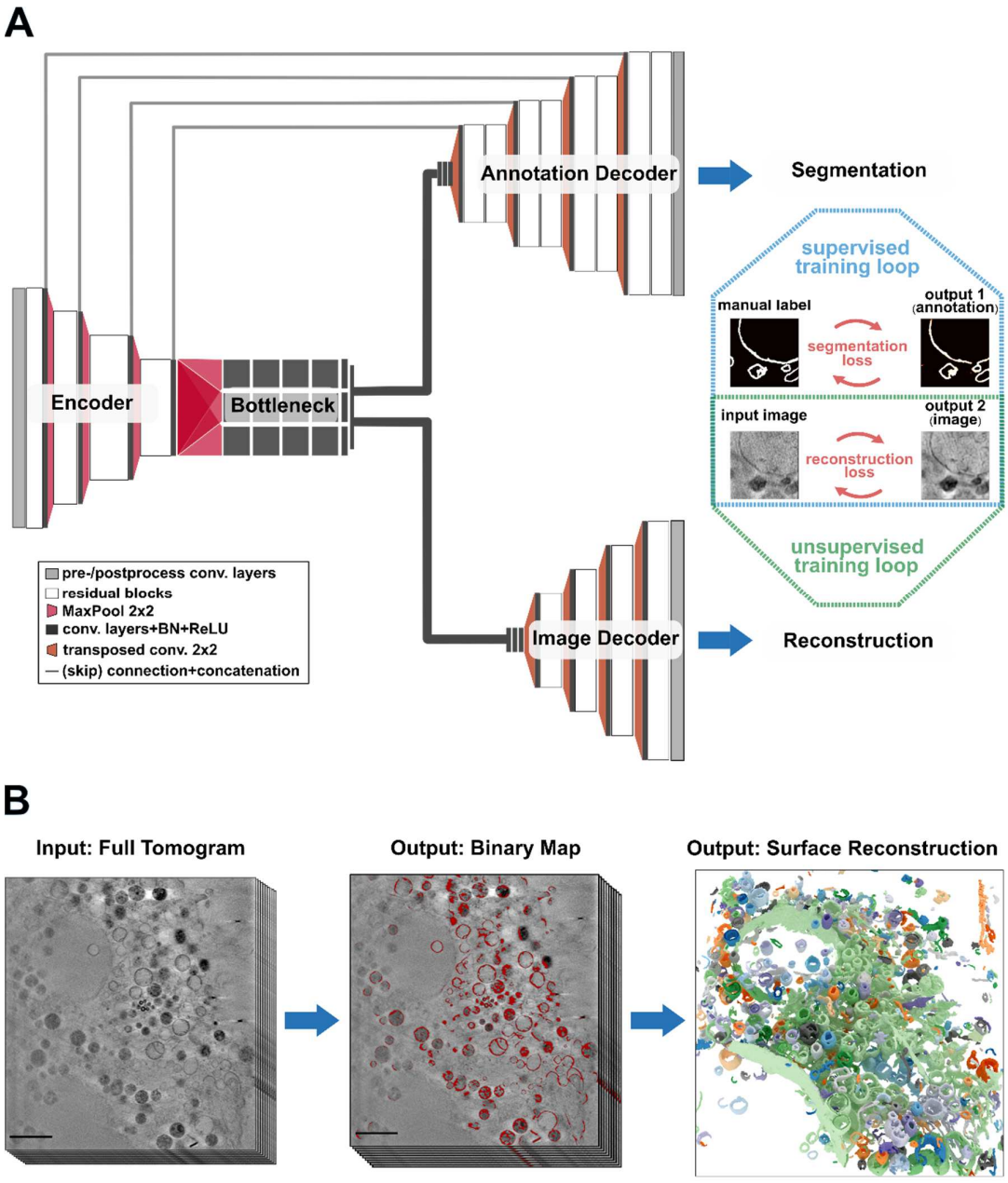

Figure 4-1: Schematic of the Convolutional Neural Network's Architecture, Training Procedure and Output Generation. A) The network is a U-Net based, two-headed autoencoder structure. The annotation decoder path produces binary label maps of the input data as automated segmentation. Annotated training data support the supervised learning of this path. The image decoder path reconstructs input data and is also trained in an unsupervised fashion. Both training routines are used iteratively to train the network in a semi-supervised fashion on annotated and unannotated training data. B) A full tomogram is a stack of several hundred input slices. The automated segmentation pathway of the CNN produces a corresponding stack of binary labels (shown as red overlay), which can also be used to produce a 3D surface reconstruction of the segmentation (shown here in random colors).

The network was designed to accommodate these particular challenges inherent to the cryo-SXT data:

Data scarcity: The access to cryo-SXT is mostly via synchrotron facilities, which significantly restricts the overall throughput of data collection. This in turn limits the amount of data available for training and testing of the neural network. The largest pool of homogeneous data available for this project were tomograms of untreated CRFK cells, which we repurposed for the training and testing procedure.

Contrast: Producing consistent levels of contrast across the datasets used for training of the neural network is challenging, since the parameters influencing the contrast can vary. The contrast in the data depends on the thickness of the specimen itself, i.e. the region of the cell, as well as the thickness of the ice left on top of the specimen after blotting during plunge-freezing. Especially the ice thickness was subject to significant variety, since the samples were prepared by manual plunge-freezing. The overall contrast can be improved to an extent by increasing the exposure during the acquisition or by acquiring more tilt images for reconstruction. However, this poses a risk of damaging the original structure by inducing irradiation damage. Therefore, each acquisition is a trade-off between irradiation dose and attainable contrast and a certain degree of variation in contrast has to be accepted.

Missing wedge artifact: The missing wedge artifact was explained in more detail above (see fig. 2-1 C). All the data shown in this dissertation were acquired at BESSY II, using cells grown on TEM grids. A consequence of this artifact relevant for this deep learning project is that the membranous outline on the top and bottom of a structure will not be clearly visible in the tomographic reconstruction. In these cases, it is impossible to accurately trace the outline even for a human user. This problem is illustrated in figure 4-2 D, where parts of the mitochondria are beginning to be blurry (see orange box). In the interest of robustness, the network was trained conservatively, such that only clearly distinct features would be traced for the training labels.

Depth of focus: Another important factor for the quality of the data is the depth of focus of the microscope. All the data used for this project were acquired using a 25 nm Fresnel zone plate, which has a depth of focus of approximately 1.5 µm. This means that even in a perfect dataset, not the entirety of the cellular volume would be in focus, leading to features outside the focus volume appearing differently than those in focus. An example for this can be seen in fig. 4-2, where the outline of the nucleus is becoming too blurry to be traced, even for a human user. Training a neural network on too ambiguous labels would produce only erratic results.

4.3.1. Training Procedure

The network was trained in a two-step semi-supervised fashion.

For supervised learning, 79 pairs of manually annotated, full frame (1324 x 1284 pixels) 2D image slices from one tomogram with their respective binary masks were used. These pairs were used to optimize the image annotation branch and the image reconstruction branch of the network. The image annotation branch predicts the manual labels as closely as possible, while the image reconstruction path learns how to reproduce the input images as accurately as possible.

The unsupervised learning then uses a large number of unannotated slices from 17 different tomograms to force the autoencoder to generalize, thus improving transferability to new datasets. In this step, weights for the segmentation decoder in the image annotation branch were frozen and only the image reconstruction path was updated. The pool of 513 raw, unannotated slices used for this step was increased by data augmentation, i.e. 90° rotations and reflections of randomly cropped sub-images.

Both training steps were performed iteratively, until convergence was satisfactory, i.e. when input tomogram slices could be restored accurately, as well as segmentation labels where provided.

In the beginning of the project, training conditions had to be optimized. Initial attempts at training with small tiles of 128 x 128 pixels did not result in sufficient recognition of relevant features over noise. Therefore, larger tiles with 256 x 256 pixels were used.

A second point was that the algorithm used for the tomographic reconstructions plays an important role in the contrast and noise in the tomographic reconstruction, which is not only important for accurate manual labeling of the training data, but also for deep learning. We experimented with training the network on tiles from weighted backprojection and simultaneous iterative reconstruction technique (SIRT[249]) in various numbers of iterations. Tomograms with 20 iterations of SIRT suppressed noise quite effectively but tended to produce more pronounced streaking artifacts on the sides of carbon-dense features. However, these were general observations, which can vary between datasets based on the experimental parameters, such as sample thickness, tilt range *et cetera*. Ultimately, the network was trained on pairs of slices and labels of a tomogram prepared with 50 iterations of SIRT and unannotated slices of 17 tomograms with 20 or 30 iterations of SIRT.

More details on the training procedure and design of the CNN are explained in our publication[105].

4.3.2. Performance

In order to assess the segmentation quality provided by the convolutional neural network, three representative cryo-soft X-ray tomograms that were not part of the training data were selected. Their automatic labels produced by the network were inspected and classified into the categories "correct labels" for correctly placed labels, "false positives" for labels that did not refer to actual structural information and "artifacts" for labels placed on image features that were actually tomographic reconstruction artifacts. Where the CNN failed to annotate cellular features, separate labels were added by manual segmentation. Quantifying the pixels across these different categories in a total of 59 slices, showed that an average of 69.8% of the annotated pixels (s.d. = 10.4) were true positives and 27.7% (s.d. = 10.8) still had to be manually added. Only 1.3 % (s.d. = 2.2) and 1.2 % (s.d. = 2.1) belonged to the false positive or reconstruction artifacts categories (fig. 4-2).

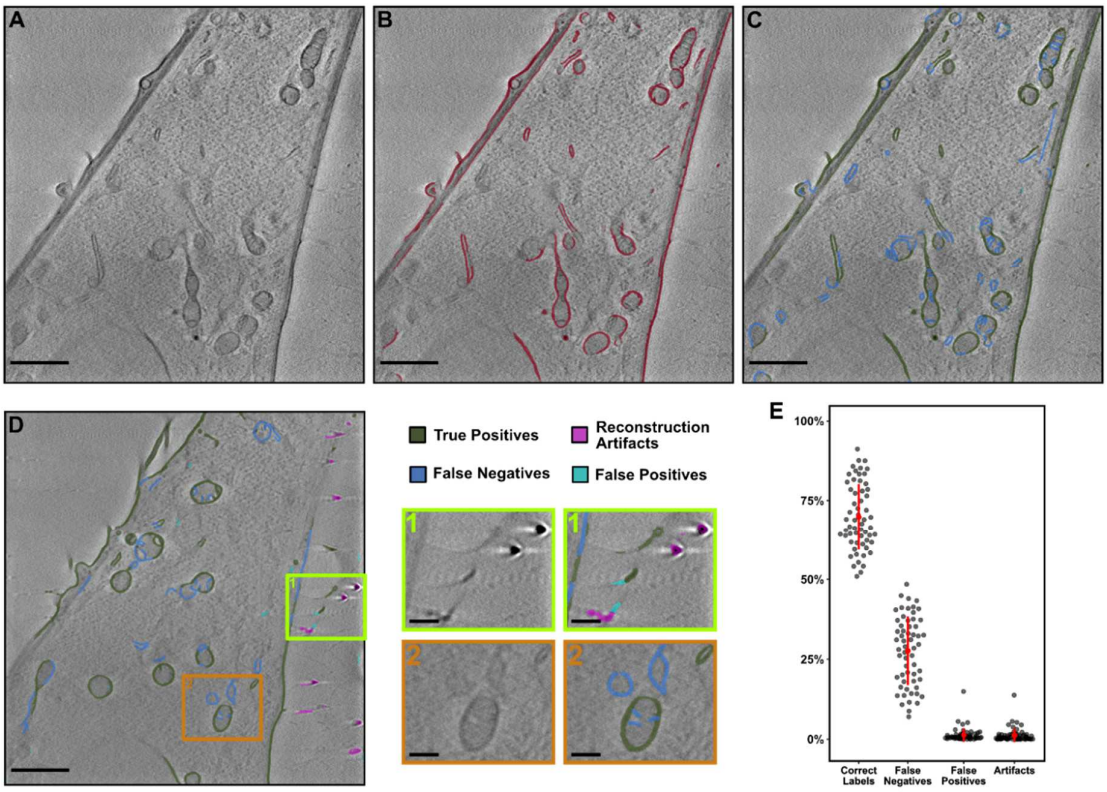

Figure 4-2: Evaluating CNN Label Quality and Robustness. A) A representative 2D slice of one of the three tomograms analyzed. B) Overlay of the binary map of automatically produced labels (red) with the same slice. C) The binary labels were categorized into correct (true positive) or false labels (reconstruction artifacts or false positives). Morphological features that should have been labeled were manually added by a human expert user and the pixels classified as false negatives. D) Another slice of the dataset highlights instances of false positives and reconstruction artifacts. E) Quantification of pixels in each category. Red dots refer to the mean percentage and the red bars indicate the standard deviation. Scale bars: A-D: 2 µm. Insets: 1 µm.

To test the performance also in a more independent way, 100 slices of a sample tomogram of a CRFK cell were manually segmented in a blinded fashion, i.e. without knowledge of the automatically generated labels. A time budget of 20 hours was allowed for the manual segmentation of these slices. Upon completion, the manually and automatically produced labels were compared. A representative example slice is illustrated in fig. 4-3.

Unlike the training data, this dataset contained a minor degree of freeze damage, as indicated by the presence of small precipitates, giving the cytosol a more granular appearance than usual in this cell type (see fig. 4-3 F). The CNN successfully ignored most of such features. On the other hand, it recognized cytoskeletal features (fig. 4-3 E), which were also underrepresented in the training data. The highest difference was with the nuclear envelope, which tends to have a more blurred appearance and is partially difficult to trace even for a human expert user (see lower right corner in fig. 4-3 B vs. C). Overall, both labels are in good agreement.

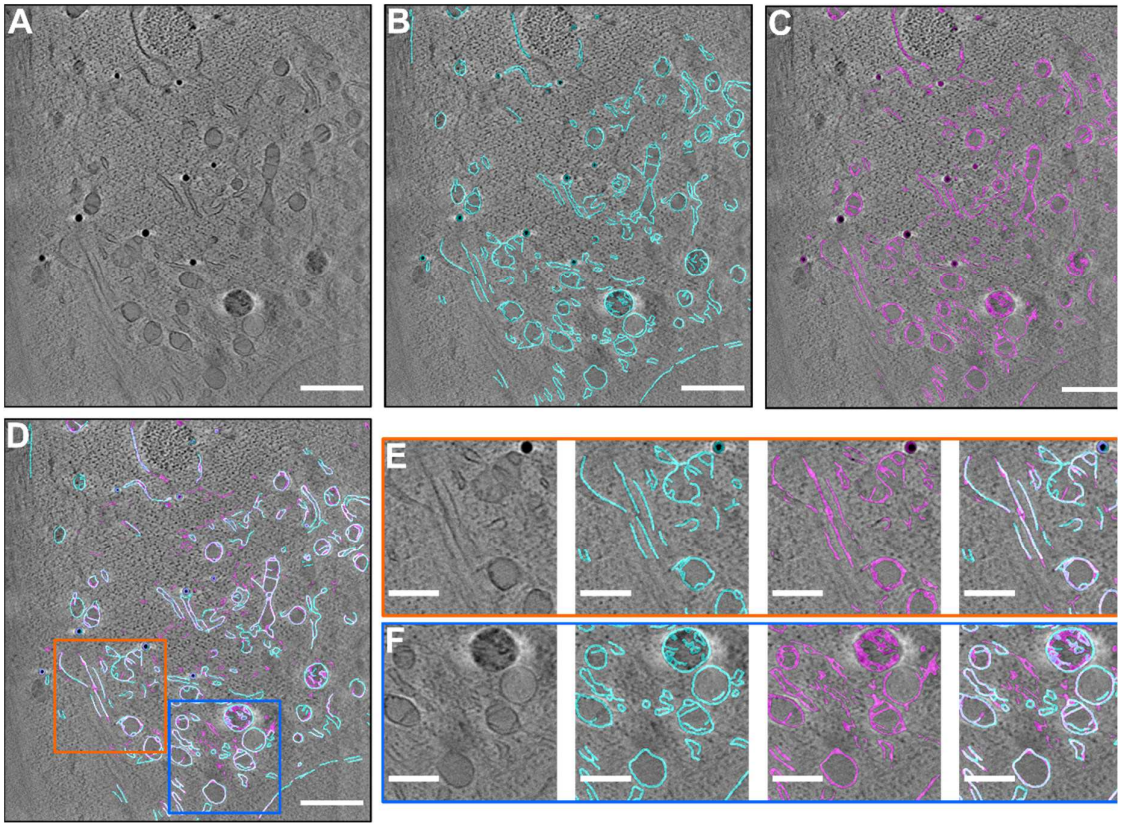

Figure 4-3: Comparison of Automated Segmentation and Blinded Manual Segmentation of the Same Slices of a Sample Dataset of CRFK Cells. A) shows a representative slice of the dataset. B) and C) show overlays with manual labels (cyan, B) or CNN-generated labels (magenta, C). D) shows both labels overlaid with the sample slice. Orange and blue boxes denote the areas highlighted in E and F. Scale bars: large panels: 2 µm. Small panels: 1 µm.

4.3.3. Transferability

For the broader application of this network, it is also important to test the performance of the network on data acquired at other cryo-TXM microscopes (fig. 4-4). For that, data acquired by Dr. Burcu Kepsutlu at the ALBA synchrotron during her PhD thesis project and raw data provided by the Harkiolaki group at Diamond Light Source were used. Both datasets could be automatically segmented by the CNN with quality comparable to the data acquired at the TXM at BESSY II. This illustrates the robustness of the CNN and potential for broader use at other synchrotron facilities.

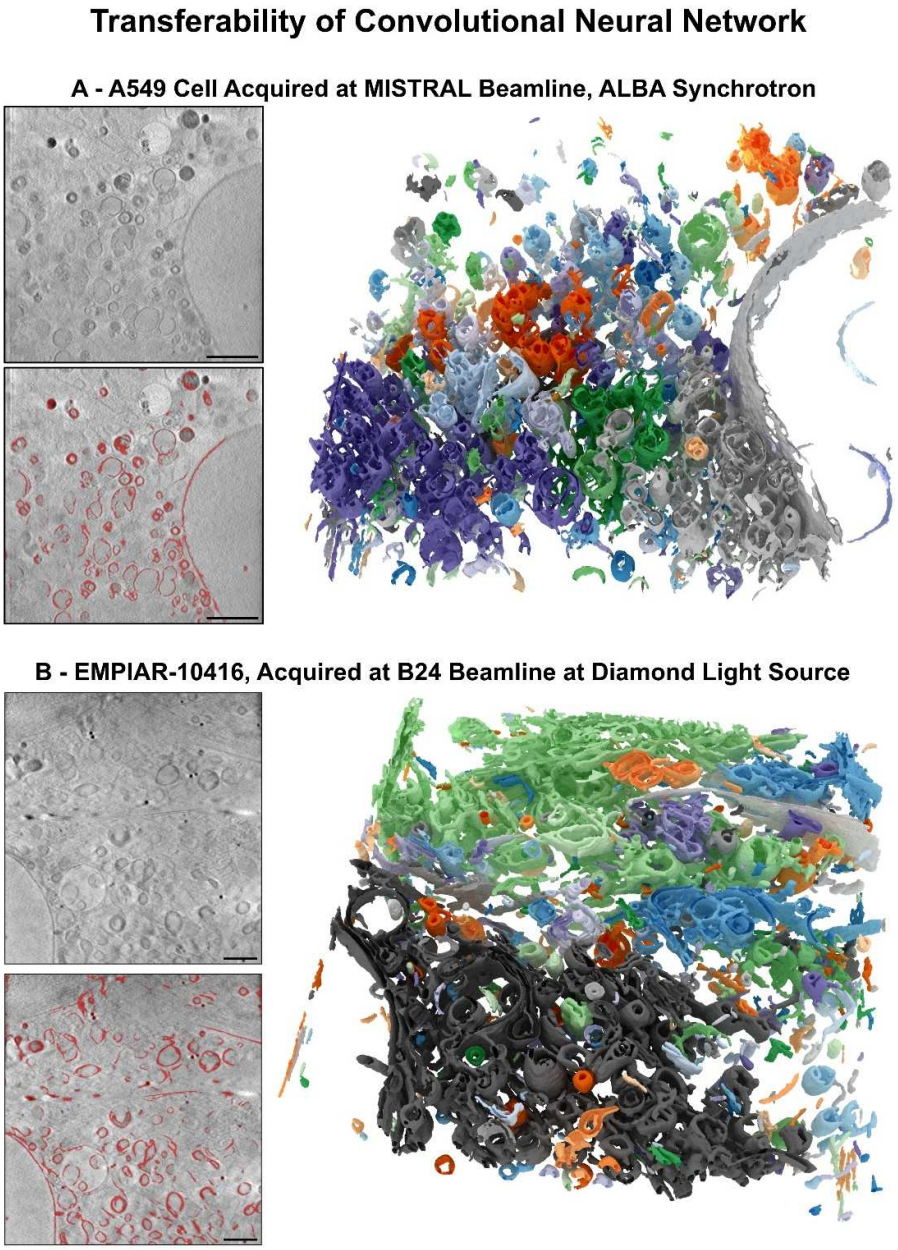

Figure 4-4: The CNN Automatically Segments Data Acquired at Other Synchrotron Facilities. The data shown in A were produced by Dr. Burcu Kepsutlu Çakmak at the MISTRAL beamline at ALBA synchrotron. The data shown in B are tomographic reconstruction of raw data provided by Harkiolaki et al., related to their publication[101] and deposited data under EMPIAR-10416. Scale bars: 2 µm.

4.3.4. Extracting Quantitative Morphological Information from CNN Labels

One of the main reasons for segmenting cryo-SXT tomograms is to extract the ultrastructural information contained in the image data and to quantify them. To illustrate the potential of the CNN for this purpose, three representative tomograms of CRFK cells were selected for automated segmentation and the structural information for a total of 59 filopodia was extracted.

Since filopodia are extensions of the plasma membrane and would thus be connected to the rest of the cell surface upon 3D segmentation, these labels had to be separated from those of the plasma membrane and ensure continuity, i.e. that the object labels would not be interrupted by reconstruction artifacts of nearby fiducial marks. Then, using the object analysis tools in the Microscopy Image Browser[248], morphological parameters were quantified (fig. 4-5).

According to their spatial orientation in the 3D-dataset, the filopodia showed a relatively diverse first (i.e. longest) axis length of their cross sections and perimeter. Depending on whether the filopodia were more parallel or horizontal to the Z axis (see blue and green versus yellow and purple filopodia in fig. 4-5), the first axis length would change. The second axis length of the filopodia cross sections was much more consistent with 132 ± 28 nm. In addition to these 2D-parameters, 3D-parameters were also extracted from the data. As expected, the average volume ($2.2 \cdot 107 \pm 1.7 \cdot 107$ nm³) and surface area ($6.1 \cdot 105 \pm 3.6 \cdot 105$ nm²) of the filopodia varied, as did their overall length (966 ± 394 nm). The relatively consistent surface area to volume ratio (30.2 ± 5.3 μm^{-1}) on the other hand is indicative of a consistent shape of the filopodia in the population (fig. 4-5 B).

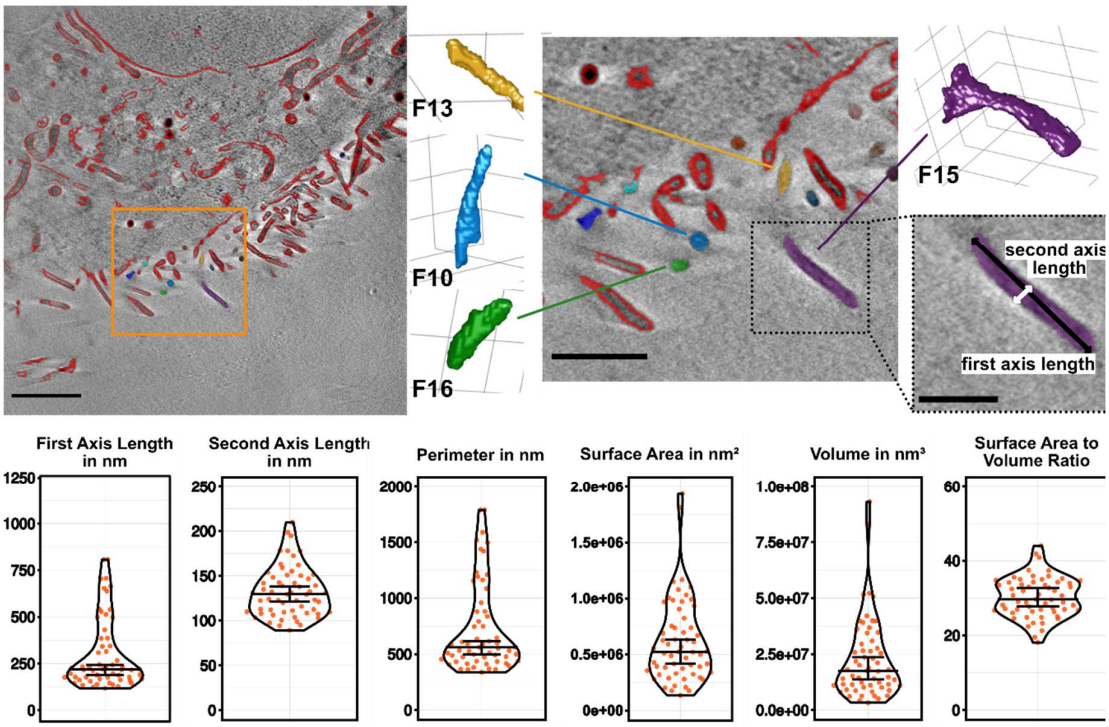

Figure 4-5: Using CNN-generated Labels for Quantification of Morphological Parameters of Filopodia in CRFK Cells. On top, the overlay is shown of the automatically produced labels (red) with the corresponding slice of a tomographic reconstruction of a CRFK cell. The panel on the right shows a magnified view of the area highlighted with the orange box. The colored regions correspond to automatically annotated labels of filopodia, which are seen as cross-section in this slice and as 3D-rendering on the sides. Note how the orientation of the filopodium in space dictates the shape of the cross-section, as illustrated specifically for the purple filopodium (F15). Below, a series of quantifications of morphological parameters are shown. First axis length, second axis length and perimeter describe the 2D cross-sections. Surface area, volume and surface area to volume ratio correspond to the 3D-analysis of the filopodium. Microscopy Image Browser[248] was used for analysis. Plots were created using Plots of Data[130].

4.4. Discussion

The segmentation task of cryo-SXT data is a major bottleneck in the field of cryo-SXT. The more complex the datasets are, the more time-consuming this task becomes, such that researchers could easily require weeks for a full segmentation of a single dataset of a mammalian cell. To address this problem, we developed a convolutional neural network, which was designed to provide rapid, robust, and fully automated segmentation of cryo-SXT tomograms.

Cryo-SXT data are challenging subjects for deep learning applications for several reasons: It is difficult to acquire sufficiently large quantities of training data due to the highly centralized access to this imaging technique. Even on high-quality datasets, the contrast may vary based on acquisition parameters, cell type, acquired region of the cell, as well as thickness of the ice layer after plunge freezing. For higher consistency of the data, we used exclusively data from CRFK cells acquired in the periplasmic region, as it was the largest pool of uniform data available to us. These cells are relatively thick in comparison to, for instance, Vero E6 cells, and exhibit higher cytoplasmic density. This is reflected in the data by higher background and more noticeable artifacts from limited depth of focus and missing wedge. Our data augmentation pipeline and the architecture of the CNN were designed to mitigate these challenges. The transferability of the CNN to data acquired of different cell types and at different synchrotrons indicates success in this regard.

The performance of the network was assessed by evaluating and complementing its segmentation labels (fig. 4-2) and comparing it to manual labels created by a blinded expert user (fig. 4-3). It emerged that our network performs robustly in terms of low false positives and also hardly labels missing wedge artifacts created by fiducial marks during tomographic reconstruction. In addition, it recognized features such as cytoskeleton (fig. 4-3), even though those were not part of the annotated training data. On the other hand, minor freeze damage in the data was successfully excluded as well (fig. 4-3). Still, it is clear that the overall performance of the network could be improved further by training it with additional data. However, it should also be noted that this analysis was performed with a single user for the manual segmentations and it is known that there may be significant discrepancies between manual segmentations produced by independent individuals[250].

An important strength of cryo-SXT is its ability to visualize the ultrastructure of biological specimens such as mammalian cells. The interior of such cells tends to be not only highly complex but also very interconnected. While this is an exciting field of research for cell biology, it also poses a significant challenge for the segmentation and classification of features visualized in cryo-

SXT tomograms. The organelle features being in close proximity or direct contact with another also means that for quantitative analysis of, for example, organelle size and distribution, objects will have to be separated from another. This problem was illustrated by filopodia, which protrude from the plasma membrane but are functionally different entities and had to be separated by manual segmentation prior to quantitative analysis (fig. 4-5). This problem could be addressed by developing an organelle classifier, which uses, for instance, the different contrasts of organelles (such as mitochondria, nucleus, lysosomes) to sort the automatic labels into subgroups for each organelle type. However, such a project requires extensive training for each organelle class and thus significantly more training data than what could be produced over the course of this project.

On the other hand, this CNN can fully segment ultrastructural features within 20 minutes or less on a consumer-grade GPU, regardless of the structural complexity of the image data. This means that users can perform on-the-fly segmentation of their tomographic reconstructions while at the beamline, which not only dramatically shortens the time for quantitative analysis but also enables more efficient decision making for better use of the beamtime at the synchrotron facility. The availability of the code and relatively low hardware requirements also mean that users can use this segmentation tool independently of large computational clusters and further improve the network by retraining it with their own data as needed.

5. Conclusions

The work related to this dissertation was mostly carried out during the COVID-19 pandemic, which was, among many other things, an example of how scientists from across disciplines could work together to understand and combat a potent viral pathogen infecting humans and animals across the globe. To achieve this, various microscopy techniques have been used individually or in combination to elucidate the structure-function relationships during infections by SARS-CoV-2, other viruses, or virus-like particles.

In the first part of this work, cryo-soft X-ray microscopy was used in combination with electron microscopy to investigate ultrastructural alterations induced by viral infection in presence or absence of FDA-approved cationic amphiphilic drugs, which had previously shown to exert antiviral effects against SARS-CoV-2 *in vitro*[35–37,119]. High-resolution cryo-SXT imaging enabled the observation and quantification of changes in the formation of dark-rimmed vesicles induced by SARS-CoV-2 in Vero E6 cells and by CAD family members fluoxetine and fluvoxamine in CRFK and Vero E6 cells. The number and size of these drug-induced multilamellar organelles changed rapidly in presence of FIPV (in CRFK cells) or SARS-CoV-2, which strongly suggests a link between the DRV formation and the mechanism of inhibition exerted by the drugs. One possible mechanism could be the inhibition of pH-sensitive cathepsin function, which is required for the lysosomal escape of coronaviruses undergoing the 'late' endolysosomal pathway. Drug-induced elevation of lysosomal pH could lead to lysosomal entrapment of virus particles in this model. In a second, not mutually exclusive model, the drug treatment interferes with lipid metabolism inside the lysosomes, leading to accumulation of lipids that are then no longer available to form replication organelles or envelopes for new virus particles during the replication cycle.

On the one hand, while these two proposed mechanisms could not be tested more conclusively during this project, this work highlighted significant benefits of cryo-SXT. This technique can serve to 1) directly visualize virus particle binding to cells, 2) observe and 3) quantify three-dimensional ultrastructural alterations induced by environmental factors, while also 4) not requiring extensive, artifact-inducing sample processing. Here, cryo-SXT proved once more to be a powerful tool to address such essential questions in virology and basic cell biology.

On the other hand, it also became evident that this technique could benefit significantly from *a priori* optimization of experimental parameters by means of a higher-throughput ultrastructure technique which operates independently of synchrotron facilities. Therefore, the second part of this work focused on Ultrastructure Expansion Microscopy. A side-by-side comparison of images from U-ExM and cryo-SXT showed that U-ExM can visualize a significant amount of structural

information just by using global stains such as NHS-ester or membrane stains. While the attainable resolution and sample preservation did not match what can be routinely accomplished by cryo-SXT, the resulting structural information is sufficient for general visualizations of cellular morphology and ultrastructural alterations. Since such global stains can in principle be combined with more specific stains, U-ExM has furthermore the potential to combine contextual ultrastructural information with specific localizations of target molecules or organelles, which would otherwise require much more complex correlative workflows such as CLEM or CLXM.

However, while the low technical requirements of this technique make it very accessible to laboratories, the extensive sample processing has significant potential to introduce artifacts into the specimen. Knowledge of such artifacts is crucial for users of U-ExM and other existing and emerging ExM protocols, which also highlights the key advantage of using near-native volume imaging techniques such as cryo-SXT to validate protocols and experimental findings. The extensive insight into the ultrastructure of CRFK and Vero E6 cells by cryo-SXT was used to identify such artifacts in U-ExM, such as loss of multilamellar or lipid-dense structures, unequal expansion of cytoplasm and organelles, and polymerization defects.

The complementary use of cryo-SXT and U-ExM was illustrated by the drug-induced formation of lipid-dense, multilamellar DRVs. These organelles can be clearly visualized and quantified by cryo-SXT. However, the limited throughput and access of synchrotron-based cryo-SXT posed a bottleneck in optimizing the experimental parameters such as drug concentration and incubation time under which these structures would form. While U-ExM experiments failed to visualize clearly the membranous ring of the DRVs, the NHS-ester stains clearly showed significant cellular alterations induced by the drugs. Still, the concrete interpretation of these changes would have been impossible in U-ExM without cryo-SXT or other complementary methods. Thus, U-ExM could be invaluable as a screening tool for ultrastructural analysis to empirically determine optimum experimental conditions. These conditions can then be analyzed in more detail and accuracy by techniques such as cryo-SXT. This approach will make cryo-SXT more accessible and efficient for researchers.

To further increase the efficiency of cryo-SXT was the aim of the last part of this work. This was accomplished by automating the segmentation of tomographic datasets, which poses a central bottleneck in cryo-SXT. With only a few datasets, a convolutional neural network was trained by means of semi-supervised deep learning. The CNN automatically segments even highly complex datasets of mammalian cells within less than twenty minutes, while producing only minimal artifacts or false positives. The application of this network was illustrated by quantification of

filopodia. Moreover, the transferability of the CNN to the transmission X-ray microscopes operated at other synchrotron facilities was shown. Based on the provided code and documentation, users can freely use the software to perform segmentation or even further refine the training using their own data.

Taken together, this work has illustrated how cryo-SXT can be used in combination with other techniques such as U-ExM to visualize changes in the cellular ultrastructure caused by environmental factors such as treatment with drugs or infection with viruses. However, it also underlined many avenues for future study and development:

Coronavirus infection: The data collected in this work points to alterations in lipid metabolism as a potential mechanism by which the replication cycle of FIPV and SARS-CoV-2 could be inhibited. Firstly, extending the range of experimental conditions, such as time points of infection, drug concentrations etc., as well as tracing viral uptake and replication by fluorescent markers will be important experiments to further test this hypothesis. Secondly, *in vitro* experiments with cell monolayers alone are not sufficient to fully elucidate the mechanism of action of a drug against viral infection since they cannot account for more systemic effects such as, for example, the role of the immune system. For instance, fluoxetine and fluvoxamine are believed to exert anti-inflammatory effects[251–254] and have been proposed to act through agonism to the sigma-1 receptor[255]. Such effects have been proposed to reduce mortality in cases of hyperinflammation, such as the cytokine storm occurring in COVID-19 patients[52,251,256,257]. More complex models will be required to determine the importance of the morphological alterations observed on the single-cell level in the context of a tissue or whole organism for disease progression and clinical outcome.

Expansion Microscopy: The continuous emergence of new ExM protocols is likely to not only lead to increased expansion factors and improved labeling of important target molecules[240,258–260], but also to improved structure preservation and reduction of artifacts[237]. For that, rigorous testing and comparison with comprehensive ultrastructural data acquired under near-native conditions is a crucial step. The performance of many ExM techniques is often benchmarked using only a few organelles or macromolecular assemblies, such as microtubules[218,221,230,237,240,261], synapses[216,217,219,221], or mitochondria[218,237]. However, for adequate application and interpretation of each technique, knowledge of unpreserved structures or possible artifacts is crucial. For high-accuracy analysis, a combination of cryo-SXT and ExM would be an invaluable tool. For instance, samples could be vitrified and imagined by cryo-SXT and then processed for ExM, using a

procedure such as cryo-ExM[237]. Analysis of such data allows not only to characterize formation of artifacts through ExM processing but will also help to address pressing biological questions.

Cryo-SXT: Accessibility to the technique posed a central bottleneck of this work. With cryo-SXT being still predominantly synchrotron-based, the overall throughput of data in the field is still limited, which consequently also limits the scope of the studies that can be performed. It affected the number of time points and controls that could be used in the coronavirus experiments (chapter 2) and also the number of datasets available for the deep learning (chapter 4). This challenge has been recognized in the field and the workflows at the synchrotron facilities are being increasingly automated[55,101,262]. Moreover, the development of laboratory-based cryo-SXT microscopes[263,264] will be a crucial means to provide broader access and decentralization to this technique, which would also further accelerate the process of innovation. A widened community could collaborate even more effectively to tackle present limitations such as, for example, the size limit of samples that can currently be visualized by cryo-SXT. The implementation of focused ion-beam technology in cryo-SXT could allow accessing larger, more complex and physiologically relevant specimens, for instance by producing lamella for cryo-SXT from high-pressure frozen samples, similarly to cryo-FIB lift-out techniques being already used for electron tomography[65,265]. Harnessing the full potential of cryo-SXT by microscopy of tissue samples has tremendous potential to further advance our understanding of physiologically relevant processes, including, but absolutely not limited to, viral infections, inflammation, and many more.

6. Materials and Methods

Table 6-1: List of Reagents Used in This Work.

Reagent	Manufacturer	Cat. Number	Stock Concentration
100 nm Gold Nanoparticles	Aldrich	753688	Citrate Buffer, OD=1
2% N,N'-methylenbisacrylamide (BIS)	Sigma	M1533	2%
40% Acrylamide, sterile filtered	Sigma	A4058	40%
Sodium Acrylate, 97% purity	Sigma-Aldrich	408220	38% w/v
DMEM 1x, +4.5 g/l D-Glucose	Gibco	31053-028	
100x Penicillin/Streptomycin	Sigma-Aldrich	P4333	10,000 U/ml penicillin, 10 mg/ml streptomycin
GlutaMAX 100x	Gibco	35050-061	
Fetal Calf Serum, heat-inactivated	Gibco	A3840001	
0.25% Trypsin / EDTA	Gibco	25200-072	
Saponin	Roth	9622.1	
SDS	Sigma-Aldrich	75746	
Tris, >99.9%	Roth	5429.3	
EDTA, >99%	Roth	X986.2	
Tween 20	Roth	9127.1	
DMSO, LC-MS grade, >99.7%	Thermo Scientific	85190	
APS	Roth	9592	10%
TEMED, 99% purity	Roth	2367.3	
Fluoxetine Hydrochloride	Sigma	F132-50MG	5 mM in DMSO
Imipramine Hydrochloride	Sigma	I7379-25G	20 mM in H_2O
Fluvoxamine Maleate	Tocris	1033	10 mM in DMSO
Horse Serum	Gibco	16050-130	
Goat Serum	Gibco	16210-064	
16% Paraformaldehyde, EM grade	EMS	15710	
50% Glutaraldehyde, EM grade	EMS	16316	
NaCl	Carl Roth	3957	5 M

5

Table 6-2: List of Dyes Used in This Work.

Dye Name	Manufacturer	Stock concentration	Dilution
CellMask™ Orange	Invitrogen, C10045	5 mg/ml in DMSO	1:100
ATTO® 647N NHS-Ester	ATTO-TEC, AD 647N-35	0.5 mg/ml DMSO	1:300
ATTO® 565 NHS-Ester	ATTO-TEC, AD 565-35	0.5 mg/ml DMSO	1:300
mCLING ATTO 647N	Synpatic Systems, 710 006AT1	0.5 nmol H_2O	1:100
CellBrite® Fix 640	BIOTIUM, 30089A	1 vial in 70 µl DMSO	1:100
FM™ 1-43FX	Invitrogen, F35355	1 mg/ml in DMSO	1:300
Concanavalin A ATTO® 565	Manually labeled in lab	300 µg/ml in PBS	1:300
WGA Alexa Fluor® 594	Invitrogen, W11262	1 g/l in PBS	1:300

Table 6-3: List of Working Solutions Used in This Work.

Solution	Contents
10x PBS	1.37 M NaCl
	27 mM KCl
	100 mM Na_2HPO_4
	18 mM KH_2PO_4
	pH 7.4
Anchoring solution	100 µl 40% acrylamide
(for 4 ml)	175 µl 16% PFA
	3725 µl 1x PBS
Monomer solution	0.5 ml 38% w/v sodium acrylate
(1 ml in 90 µl aliquots)	0.25 ml 40% acrylamide
	50 µl 2% BIS
	100 µl 10x PBS
Denaturation solution	4 ml 500 mM Tris pH 9
(for 40 ml)	1.6 ml 5 M NaCl
	34.4 ml MQ water
	2.3 g SDS pellets
Quenching Solution	50 mM NH_4Cl in PBS
U-ExM Fixative	4% paraformaldehyde
(Prepared fresh)	0.2% glutaraldehyde in PBS

5

Methods

Cell culture

Crandell-Rees Feline Kidney (CRFK) and Vero E6 cell lines were kindly provided by the lab of Benedikt Kaufer PhD at the department of veterinary medicine at Freie Universität Berlin.

Cells were cultivated in a humidified 37 °C incubator at 5 % CO_2 in DMEM (CRFK cells) or MEM (Vero E6 cells), supplemented with 10 U/ml penicillin, 10 µg/ml streptomycin, 10 % heat-inactivated fetal bovine serum, and 2 mM glutamine. Cells were passaged 2-3x per week by trypsination and subsequent dilution 1:6 (CRFK cells) or 1:4 (Vero E6 cells). Regular tests were conducted to exclude mycoplasma contamination.

Cell Seeding for cryo-SXT

Cryo-SXT: R 2/2 Au G200F1 finder grids or Au-HZB-2 grids (Quantifoil Micro Tools GmbH, Germany) were cleaned for 30 s in a Diener Zepto plasma cleaner (Diener Electronic, Germany) at maximum power. Then, the grids were sterilized in 80 % ethanol and placed into wells of a 12-well-plate and washed with sterile 1x PBS to remove any residual ethanol. The cells were then trypsinized from their original culture, counted and diluted in fresh medium. The diluted cell suspension was then carefully pipetted on top of the grids using a 200 µl pipet to reach the desired cell count for the experiment. The well-plates were gently shaken to mix the cell suspensions in the wells and ensure more homogenous attachment to the grid surface.

Infection with Feline Coronavirus (FIPV) for cryo-SXT or TEM

Feline infectious peritonitis virus (ATCC® VR990 ™) WSU 791146 from ATCC was propagated, purified, and quantitated by plaque assay by Chuanxiong Nie in the lab of Benedikt Kaufer, at the department of veterinary medicine at Freie Universität Berlin.

For the experiments with MOI of 100 and 200, CRFK cells were seeded the day before to reach a confluency of 80% on the grids on the day of the experiment. The cells were then washed with PBS and placed on ice for 15 minutes for initial cooling. Then, the virus stock ($1.2 * 10^8$ pfu/ml) was diluted to reach an estimated multiplicity of infection of 100 or 200, respectively, and added to the cells. The multiplicity of infection was determined based on the estimated cell count and the determined virus titer of the prepared stocks. The cells were then placed for another 15 minutes on ice, before being placed in the incubator for the designated time of infection (3 or 5 minutes). Then, the cells were briefly washed once with PBS and fixed for at least 30 minutes with 1 % glutaraldehyde in PBS.

For the other experiments, cells were seeded two days before to allow for the 24 h treatment with drugs, i.e. 10 µM fluoxetine, 10 µM or 30 µM imipramine. After the drug-treatment, all cells were washed with pre-chilled PBS and placed on ice for one minute. The virus stock was diluted to reach the indicated MOI and added to the wells. The well plates were then left another 10 minutes on ice, before being moved to the 37 °C incubator for the designated time of infection, after which all cells were briefly washed with PBS and fixed with 1 % glutaraldehyde in PBS for 2 hours. Cells prepared for TEM analysis were fixed for 2 h with 2 % glutaraldehyde in PBS.

Infection of Vero E6 cells with SARS-CoV-2 for cryo-SXT

SARS-CoV-2 BavPat 1/2020 isolate was stored, propagated, purified and quantified in the BSL-3 facility in the laboratory of Benedikt Kaufer, PhD.

On the first day of the experiment, 300 µl suspension of Vero E6 cells from a 90 % confluent T75 flask were seeded on plasma-cleaned TEM finder grids in 12-well plates. The following day, the medium of all wells was exchanged with fresh medium, with or without 10 µM final concentration of fluvoxamine for 24 hours treatment. On the day of the virus infection, the cells were transferred to the BSL-3 environment. The virus stock was vortexed for 60 seconds, then spun down at maximum speed in a cooling centrifuge for 30 min. Then, the virus stock was diluted to a final titer of 10^7 pfu/ml in either medium or medium containing 10 µM fluvoxamine. For uninfected controls, the same volume of PBS was used instead of virus stock. All cells were first pre-cooled by washing them with chilled, sterile 1x PBS and placing them on chilled gel-packs for 5 minutes. Then, the medium in each well was then exchanged with 500 µl of fresh medium with or without drug or virus. The plates were then left to incubate on chilled gel packs for another 10 minutes to allow virus attachment to the cells for synchronous uptake. Then, the plates were placed in the 37 °C incubator for 3 or 5 minutes. After the time of infection, all wells were washed briefly with 1 ml chilled PBS and then fixed for 30 min with 1 ml of 1 % glutaraldehyde in PBS at room temperature. After this first fixation, all cells had to be fixed for another 24 hours with fresh 4 % paraformaldehyde in PBS prior to release from the BSL-3 environment and plunge-freezing.

The work in the BSL-3 environment was performed by Dr. Jakob Trimpert and his staff.

Cryo-SXT sample preparation, data acquisition, and reconstruction

Unless otherwise specified, all material used in this work was chemically fixed. While it is not technically necessary for cryo-SXT, this was required to conform with the biosafety regulations at BESSY II for infected material. Uninfected cells were also fixed to ensure comparability with the infected cells.

Prior to vitrification, all grids were screened using a cell culture microscope to assess their overall quality regarding grid integrity and cell density. 7 µl of a suspension of 100 nm AuNPs were pipetted directly on top of the grids. The grids were then manually blotted and plunged into liquid ethane using a custom-made plunger. Specimen passing also the second quality control after vitrification were then transferred into cryo-EM grid boxes for storage in liquid nitrogen until use.

Data collection was performed at the U41-TXM beamline at the BESSY II synchrotron facility. All data were acquired at 510 eV energy under vacuum and cryo-conditions. For TEM grids, the standard tilt range of ± 60° was used. HZB-II grids allowed for a larger tilt range with ± 65°. For CRFK cells, the standard tilt increment was 1° and for Vero E6 cell samples 0.5°. The exposure was set based on the thickness of the ice and the cells. All presented data were acquired with a 25 nm Fresnel zone plate objective, unless otherwise specifically mentioned.

The collected data were reconstructed in IMOD v. 4.11.11[266], using the 100 nm gold fiducial marks for tracking and alignment. Reconstructions were calculated using the simultaneous iterative reconstruction technique (SIRT[249]) for 20 or 30 iterations.

Manual Segmentation of DRVs in cryo-SXT tomograms

For morphological analysis of the DRVs, datasets were manually segmented using the brush and interpolation tools in Microscopy Image Browser v. 2.84[248]. To be included in the analysis, each dark-rimmed vesicle was required to have a distinct lumen, in order to be distinguished from lipid droplets. Objects with any axis length below 10 pixels were filtered out. In addition, those DRVs that were not fully covered by the image stack were also excluded. Morphological parameters were calculated using an isotropic voxel size of 9.8 nm.

Ultrastructure Expansion Microscopy

Cell seeding: 12 mm coverslips were sterilized in ethanol before transferring to the cell culture bench. The coverslips were then placed into the wells, leaning on the well walls to allow effective washing with PBS on both sides to remove remaining ethanol. The freshly prepared cell suspension was counted and a volume corresponding to 50.000-70.000 cells per well was added to each well. The final volume per well was topped up with fresh medium to reach 1 ml per well.

Drug treatment: CRFK cells were treated with 10 µM fluoxetine or the equivalent volume of DMSO (2 µl) diluted in 1 ml medium per well for 24 hours. Vero E6 cells were treated with 10 µM fluvoxamine or the equivalent volume DMSO (1 µl) diluted in 1 ml medium per well for 24 hours.

First fixation: After the drug treatment, the cells were washed once with 1 ml 1x PBS and then fixed for 30 minutes with freshly prepared, pre-warmed PBS containing 4 % PFA and

0.2 % glutaraldehyde. After fixation, the samples were washed three times with 1x PBS and then quenched with 50 mM NH_4Cl for 30 minutes, after which they were washed again three times with PBS.

Staining and second fixation: The samples were placed upside down on 40 µl of staining solution and incubated for 2 h or overnight in a humid chamber at 37 °C in the dark and then washed three times for 10 minutes each in 1x PBS on a shaker set to 150 rpm. After the fixation, samples were washed once for 10 minutes with 1x PBS and fixed again with 4 % PFA, 0.2 % glutaraldehyde in PBS for 30 minutes.

Anchoring: Samples were placed in 500 µl anchoring solution for overnight incubation in the dark at room temperature.

Gelation: The monomer solution was prepared the previous evening and stored at -20 °C in 90 µl aliquots. The lid of a 12-well plate was covered with parafilm and placed on chilled metal blocks embedded in ice and left to equilibrate for half an hour. Then, 5 µl of TEMED were added to a 90 µl aliquot of monomer solution. 45 µl of this solution were removed after pipetting up and down at least 30 times and then mixed with a droplet of 2.5 µl APS on the parafilm. Then, a sample was taken from its well-plate, residual anchoring solution carefully removed with a tissue and placed upside down onto the gelation mix. Once all samples were prepared, the batch was placed at 4 °C in the dark for 1 hour for gelation.

Denaturation: Denaturation buffer was freshly prepared for each experiment. After gelation, the samples were incubated with 3 ml denaturation buffer in a 6-well plate for 15 minutes and then transferred to 15 ml falcon tubes containing 5 ml denaturation buffer. The denaturation was performed by incubation at 95 °C for one hour.

Expansion: After heat denaturation, the volume in the falcon tubes was topped up with 1x PBS and then the whole liquid decanted, leaving the gel inside the tube. The gel was then washed at least three times for 30 minutes with 1x PBS. After the last washing step, buffer and gel were poured into 10 cm Petri dishes and deionized water was added to dilute the PBS. After 30 minutes incubation under gentle shaking, the solution was decanted and replaced with deionized water, then placed again on the shaker for 30 minutes incubation. This step was repeated two more times at least, until the diameter of the gel no longer increased.

The gel expansion factor was determined by dividing the gel diameter after expansion by the diameter of the 12 mm coverslips.

Spinning Disk Confocal Microscopy

Data acquisition was performed on an inverted confocal microscope with the following components: IX71, 60×/NA 1.42 oil objective, CSU-X1 Yokogawa spinning disk, iLas2 FRAP system (Gataca Systems),

ORCA Flash 4.0LT CMOS camera (Hamamatsu). Exposure time and laser power were matched for the acquisition of comparable data (e.g. drug-treated versus controls). Image analysis was performed using FIJI[247].

Convolutional Neural Network Training

The CNN was trained on 79 pairs of raw 1324 × 1284 pixel slices from a single tomogram of a CRFK cell and their corresponding binary labels produced by manual segmentation in MIB[248]. 513 unannotated slices from 17 other tomograms from CRFK cells were used for semi-supervised training. For those, no manual labels were produced. The training data were divided into 256 x 256 pixel images or image/label pairs and augmented by applying random 90° rotations and vertical or horizontal reflections. Further details of the training procedure are explained in our publication[105].

Segmentation Quality Evaluation

Three representative cryo-SXT datasets of CRFK cells that had not been used for training or validation were selected and automatically segmented by the CNN. A human expert user then inspected the segmentation result of 59 randomly selected slices. The automatically generated labels were divided into categories of *true positives*, *false positives*, and *reconstruction artifacts*. Missing annotations were added separately by manual segmentation, where a cellular feature could be accurately traced with a 4-pixel wide brush tool. These manually added labels formed the category of *false negatives*. The evaluation scored the number of pixels in each category for each slice versus the total amount of pixels across all categories.

Filopodia Analysis

Sixty filopodia from three different, fully segmented tomograms from CRFK cells were selected for analysis. The criteria were, that they were entirely captured by the volume of the tomogram, i.e. not protruding beyond the field of view in any direction and that they were not interrupted by the streaking artifacts caused by the 100 nm gold fiducial markers added to the sample during plunge-freezing. Each filopodium was individually inspected for possible overlaps or discontinuities of the labels, which were carefully edited by manual segmentation. Since the filopodia are part of the plasma membrane, their labels had to be manually separated at the base of the filopodia by manual segmentation. This process of inspection and editing took approximately two hours per tomogram. Using the quantification tool integrated in the Microscopy Image Browser, 2D and 3D data were extracted and calculated, assuming isotropic voxels of 9.8 nm. The 2D quantification for each filopodium consists of mean and standard deviation of all 2D objects (i.e. cross-sections) of that filopodium. The 3D quantification of axes lengths is based on a fitted ellipsoid around the 3D object of the respective filopodium.

Lists of Figures and Tables

Figures:

Tables

Acknowledgements

First, I thank my supervisors for their continuous support throughout this work. Helge Ewers for giving me the freedom to pursue my own projects and interests. Gerd Schneider for his initiative and his incredible patience explaining physics to me. James McNally for investing much of his time discussing hypotheses, plans, and how to improve my writing.

Many thanks go to the staff of the HZB U41 TXM group, who lent their support to me and my project: Stephan Werner, Christoph Pratsch, Peter Guttmann, and Stefan Rehbein. Special thanks to Stephan Werner, who patiently taught me the use of the X-ray microscope and was always ready to solve even the most unexpected problems.

Also, I thank the members of the Ewers Lab at Freie Universität Berlin who created a supportive environment for my work, even during the times of the pandemic. Special thanks go to Kita Schmidt, Chethana, and Raluca Groza for fruitful discussions and support, as well as to Nadja Hümpfer who shared her extensive experience in Expansion Microscopy with me. Many thanks also to my student Jasmin El-Khabbaz for her practical help and many good questions.

This work was also significantly supported by the work of my collaborators: Chuanxiong Nie, Kunio Nagashima, Jakob Trimpert, Mohsen Sadeghi, Susanne Kaufer, and Benedikt Kaufer.

Thanks to those who dedicated their time to read this work and gave their feedback: Gesine Goldammer, Lara Kämmerer, Jasmin El-Khabbaz, Bas van Bommel, Jia Hui Li, and Raluca Groza. Special thanks to James McNally, who helped me to better distill my ideas and put them on paper.

The graphical abstract and the illustrations shown in figures 2-14 and 2-15 were created by Ioana Weber (https://ioana-weber.info/).

I am also very grateful to my former and current mentors for taking the time to hear me out, giving advice, and telling me things I needed to hear. Sutapa, Jia, Ori, and Rainer.

This work would have never been completed without the support of my friends along the way. Mariana, Vincent, Linda, Maggy, Ines, Joy, Jia, Jia, Jana, Gesine, Toni, Ayk, Nina, Nadav, Lara, Tomás, Sana, Ann, Paulina, Regine.

Lastly, I want to thank my family. Christina, Susanne, Ute, Monika, Günter, and Thomas.

References

1. Sheahan, B. J. & Donnelly, W. J. C. Enzyme histochemical and ultrastructural alterations in the brains of Friesian calves with GM1 gangliosidosis. *Acta Neuropathol. (Berl.)* **30**, 73–84 (1974).

2. Eymieux, S. *et al.* Ultrastructural modifications induced by SARS-CoV-2 in Vero cells: a kinetic analysis of viral factory formation, viral particle morphogenesis and virion release. *Cell. Mol. Life Sci.* **78**, 3565–3576 (2021).

3. Gorbalenya, A. E. *et al.* The species Severe acute respiratory syndrome-related coronavirus: classifying 2019-nCoV and naming it SARS-CoV-2. *Nat. Microbiol.* **5**, 536–544 (2020).

4. Masters, P. S. The Molecular Biology of Coronaviruses. *Adv. Virus Res.* **66**, 193–292 (2006).

5. Fehr, A. R. & Perlman, S. Coronaviruses: An Overview of Their Replication and Pathogenesis. *Coronaviruses* **1282**, 1–23 (2015).

6. Cui, J., Li, F. & Shi, Z.-L. Origin and evolution of pathogenic coronaviruses. *Nat. Rev. Microbiol.* **17**, 181–192 (2019).

7. Corman, V. M., Muth, D., Niemeyer, D. & Drosten, C. Hosts and Sources of Endemic Human Coronaviruses. *Adv. Virus Res.* **100**, 163–188 (2018).

8. V'kovski, P., Kratzel, A., Steiner, S., Stalder, H. & Thiel, V. Coronavirus biology and replication: implications for SARS-CoV-2. *Nat. Rev. Microbiol.* **19**, 155–170 (2021).

9. Jackson, C. B., Farzan, M., Chen, B. & Choe, H. Mechanisms of SARS-CoV-2 entry into cells. *Nat. Rev. Mol. Cell Biol.* **23**, 3–20 (2022).

10. Drosten, C. *et al.* Identification of a Novel Coronavirus in Patients with Severe Acute Respiratory Syndrome. *N. Engl. J. Med.* **348**, 1967–1976 (2003).

11. Zaki, A. M., van Boheemen, S., Bestebroer, T. M., Osterhaus, A. D. M. E. & Fouchier, R. A. M. Isolation of a Novel Coronavirus from a Man with Pneumonia in Saudi Arabia. *N. Engl. J. Med.* **367**, 1814–1820 (2012).

12. de Wit, E., van Doremalen, N., Falzarano, D. & Munster, V. J. SARS and MERS: recent insights into emerging coronaviruses. *Nat. Rev. Microbiol.* **14**, 523–534 (2016).

13. Hu, B., Guo, H., Zhou, P. & Shi, Z.-L. Characteristics of SARS-CoV-2 and COVID-19. *Nat. Rev. Microbiol.* **19**, 141–154 (2021).

14. Wolff, G., Melia, C. E., Snijder, E. J. & Bárcena, M. Double-Membrane Vesicles as Platforms for Viral Replication. *Trends Microbiol.* **28**, 1022–1033 (2020).

15. Cortese, M. *et al.* Integrative Imaging Reveals SARS-CoV-2-Induced Reshaping of Subcellular Morphologies. *Cell Host Microbe* **28**, 853-866.e5 (2020).

16. Roingeard, P. *et al.* The double-membrane vesicle (DMV): a virus-induced organelle dedicated to the replication of SARS-CoV-2 and other positive-sense single-stranded RNA viruses. *Cell. Mol. Life Sci.* **79**, 425 (2022).

17. Knoops, K. *et al.* SARS-Coronavirus Replication Is Supported by a Reticulovesicular Network of Modified Endoplasmic Reticulum. *PLoS Biol.* **6**, e226 (2008).

18. Mendonça, L. *et al.* Correlative multi-scale cryo-imaging unveils SARS-CoV-2 assembly and egress. *Nat. Commun.* **12**, 4629 (2021).

19. Wolff, G. *et al.* A molecular pore spans the double membrane of the coronavirus replication organelle. *Science* **369**, 1395–1398 (2020).

20. Klein, S. *et al.* SARS-CoV-2 structure and replication characterized by in situ cryo-electron tomography. *Nat. Commun.* **11**, 5885 (2020).

21. Hardenbrook, N. J. & Zhang, P. A structural view of the SARS-CoV-2 virus and its assembly. *Curr. Opin. Virol.* **52**, 123–134 (2022).

22. Dandekar, A. A. & Perlman, S. Immunopathogenesis of coronavirus infections: implications for SARS. *Nat. Rev. Immunol.* **5**, 917–927 (2005).

23. Kipar, A. & Meli, M. L. Feline Infectious Peritonitis: Still an Enigma? *Vet. Pathol.* **51**, 505–526 (2014).

24. Ng, S. W., Selvarajah, G. T., Cheah, Y. K., Mustaffa Kamal, F. & Omar, A. R. Cellular Metabolic Profiling of CrFK Cells Infected with Feline Infectious Peritonitis Virus Using Phenotype Microarrays. *Pathogens* **9**, 412 (2020).

25. Desmarets, L. M. *et al.* Establishment of feline intestinal epithelial cell cultures for the propagation and study of feline enteric coronaviruses. *Vet. Res.* **44**, 71 (2013).

26. Belouzard, S., Millet, J. K., Licitra, B. N. & Whittaker, G. R. Mechanisms of Coronavirus Cell Entry Mediated by the Viral Spike Protein. *Viruses* **4**, 1011–1033 (2012).

27. Vennema, H., Poland, A., Foley, J. & Pedersen, N. C. Feline Infectious Peritonitis Viruses Arise by Mutation from Endemic Feline Enteric Coronaviruses. *Virology* **243**, 150–157 (1998).

28. Tresnan, D. B., Levis, R. & Holmes, K. V. Feline aminopeptidase N serves as a receptor for feline, canine, porcine, and human coronaviruses in serogroup I. *J. Virol.* **70**, 8669–8674 (1996).

29. Regan, A. D., Shraybman, R., Cohen, R. D. & Whittaker, G. R. Differential role for low pH and cathepsin-mediated cleavage of the viral spike protein during entry of serotype II feline coronaviruses. *Vet. Microbiol.* **132**, 235–248 (2008).

30. Regan, A. D., Ousterout, D. G. & Whittaker, G. R. Feline Lectin Activity Is Critical for the Cellular Entry of Feline Infectious Peritonitis Virus. *J. Virol.* **84**, 7917–7921 (2010).

31. Malbon, A. J. *et al.* Feline Infectious Peritonitis as a Systemic Inflammatory Disease: Contribution of Liver and Heart to the Pathogenesis. *Viruses* **11**, 1144 (2019).

32. Takano, T. *et al.* Analysis of the mechanism of antibody-dependent enhancement of feline infectious peritonitis virus infection: aminopeptidase N is not important and a process of acidification of the endosome is necessary. *J. Gen. Virol.* **89**, 1025–1029 (2008).

33. Graham, R. L. & Baric, R. S. SARS-CoV-2: Combating Coronavirus Emergence. *Immunity* **52**, 734–736 (2020).

34. Lamers, M. M. & Haagmans, B. L. SARS-CoV-2 pathogenesis. *Nat. Rev. Microbiol.* **20**, 270–284 (2022).

35. Schloer, S. *et al.* Targeting the endolysosomal host-SARS-CoV-2 interface by clinically licensed functional inhibitors of acid sphingomyelinase (FIASMA) including the antidepressant fluoxetine. *Emerg. Microbes Infect.* **9**, 2245–2255 (2020).

36. Carpinteiro, A. *et al.* Pharmacological Inhibition of Acid Sphingomyelinase Prevents Uptake of SARS-CoV-2 by Epithelial Cells. *Cell Rep. Med.* **1**, 100142 (2020).

37. Zimniak, M. *et al.* The serotonin reuptake inhibitor Fluoxetine inhibits SARS-CoV-2 in human lung tissue. *Sci. Rep.* **11**, 5890 (2021).

38. Breiden, B. & Sandhoff, K. Emerging mechanisms of drug-induced phospholipidosis. *Biol. Chem.* **401**, 31–46 (2020).

39. Self, W. H. *et al.* Effect of Hydroxychloroquine on Clinical Status at 14 Days in Hospitalized Patients With COVID-19: A Randomized Clinical Trial. *JAMA* **324**, 2165–2176 (2020).

40. Aljadeed, R. The Rise and Fall of Hydroxychloroquine and Chloroquine in COVID-19. *J. Pharm. Pract.* **35**, 971–978 (2022).

41. Boulware, D. R. *et al.* A Randomized Trial of Hydroxychloroquine as Postexposure Prophylaxis for Covid-19. *N. Engl. J. Med.* **383**, 517–525 (2020).

42. Cavalcanti, A. B. *et al.* Hydroxychloroquine with or without Azithromycin in Mild-to-Moderate Covid-19. *N. Engl. J. Med.* **383**, 2041–2052 (2020).

43. Effect of Hydroxychloroquine in Hospitalized Patients with Covid-19. *N. Engl. J. Med.* **383**, 2030–2040 (2020).

44. Molina, J. M. *et al.* No evidence of rapid antiviral clearance or clinical benefit with the combination of hydroxychloroquine and azithromycin in patients with severe COVID-19 infection. *Med. Mal. Infect.* **50**, 384 (2020).

45. Geleris, J. *et al.* Observational Study of Hydroxychloroquine in Hospitalized Patients with Covid-19. *N. Engl. J. Med.* **382**, 2411–2418 (2020).

46. Casey, J. D. *et al.* Rationale and Design of ORCHID: A Randomized Placebo-controlled Clinical Trial of Hydroxychloroquine for Adults Hospitalized with COVID-19. *Ann. Am. Thorac. Soc.* **17**, 1144–1153 (2020).

47. Repurposed Antiviral Drugs for Covid-19 — Interim WHO Solidarity Trial Results. *N. Engl. J. Med.* **384**, 497–511 (2021).

48. Avezum, Á. *et al.* Hydroxychloroquine versus placebo in the treatment of non-hospitalised patients with COVID-19 (COPE – Coalition V): A double-blind, multicentre, randomised, controlled trial. *Lancet Reg. Health - Am.* **11**, 100243 (2022).

49. Schwartz, I. S., Boulware, D. R. & Lee, T. C. Hydroxychloroquine for COVID19: The curtains close on a comedy of errors. *Lancet Reg. Health – Am.* **11**, (2022).

50. Seftel, D. & Boulware, D. R. Prospective Cohort of Fluvoxamine for Early Treatment of Coronavirus Disease 19. *Open Forum Infect. Dis.* **8**, ofab050 (2021).

51. Reis, G. *et al.* Effect of early treatment with fluvoxamine on risk of emergency care and hospitalisation among patients with COVID-19: the TOGETHER randomised, platform clinical trial. *Lancet Glob. Health* **10**, e42–e51 (2022).

52. Lenze, E. J. *et al.* Fluvoxamine vs Placebo and Clinical Deterioration in Outpatients With Symptomatic COVID-19. *JAMA* **324**, 2292–2300 (2020).

53. COVID-19 Treatment Guidelines Panel. Coronavirus Disease 2019 (COVID-19) Treatment Guidelines. National Institutes of Health. https://www.covid19treatmentguidelines.nih.gov/. Accessed Jan. 26th 2024. (2024).

54. Therapeutics and COVID-19: living guideline, 13 January 2023. Geneva: World Health Organization; 2023 (WHO / 2019-nCoV/therapeutics/2023.1). (2023).

55. Okolo, C. A. *et al.* Sample preparation strategies for efficient correlation of 3D SIM and soft X-ray tomography data at cryogenic temperatures. *Nat. Protoc.* **16**, 2851–2885 (2021).

56. Schneider, G. *et al.* Three-dimensional cellular ultrastructure resolved by X-ray microscopy. *Nat. Methods* **7**, 985–987 (2010).

57. Garriga, D. *et al.* Imaging of Virus-Infected Cells with Soft X-ray Tomography. *Viruses* **13**, 2109 (2021).

58. Mollenhauer, H. H. Artifacts caused by dehydration and epoxy embedding in transmission electron microscopy. *Microsc. Res. Tech.* **26**, 496–512 (1993).

59. Studer, D., Humbel, B. M. & Chiquet, M. Electron microscopy of high pressure frozen samples: bridging the gap between cellular ultrastructure and atomic resolution. *Histochem. Cell Biol.* **130**, 877–889 (2008).

60. Wisse, E. *et al.* Fixation methods for electron microscopy of human and other liver. *World J. Gastroenterol. WJG* **16**, 2851–2866 (2010).

61. Kuwajima, M., Mendenhall, J. M., Lindsey, L. F. & Harris, K. M. Automated Transmission-Mode Scanning Electron Microscopy (tSEM) for Large Volume Analysis at Nanoscale Resolution. *PLoS ONE* **8**, e59573 (2013).

62. White, J. G., Southgate, E., Thomson, J. N. & Brenner, S. The structure of the nervous system of the nematode Caenorhabditis elegans. *Philos. Trans. R. Soc. Lond. B. Biol. Sci.* **314**, 1–340 (1986).

63. Dubochet, J. & McDowall, A. W. VITRIFICATION OF PURE WATER FOR ELECTRON MICROSCOPY. *J. Microsc.* **124**, 3–4 (1981).

64. Shimoni & Müller. On optimizing high-pressure freezing: from heat transfer theory to a new microbiopsy device. *J. Microsc.* **192**, 236–247 (1998).

65. Schaffer, M. *et al.* A cryo-FIB lift-out technique enables molecular-resolution cryo-ET within native Caenorhabditis elegans tissue. *Nat. Methods* **16**, 757–762 (2019).

66. Heinrich, L. *et al.* Whole-cell organelle segmentation in volume electron microscopy. *Nature* **599**, 141–146 (2021).

67. Zachs, T. *et al.* Fully automated, sequential focused ion beam milling for cryo-electron tomography. *eLife* **9**, e52286 (2020).

68. Berger, C. *et al.* Cryo-electron tomography on focused ion beam lamellae transforms structural cell biology. *Nat. Methods* **20**, 499–511 (2023).

69. Britz, S. *et al.* Structural Analysis of the Caenorhabditis elegans Dauer Larval Anterior Sensilla by Focused Ion Beam-Scanning Electron Microscopy. *Front. Neuroanat.* **15**, (2021).

70. Nguyen, H. B. *et al.* Methodological Improvements With Conductive Materials for Volume Imaging of Neural Circuits by Electron Microscopy. *Front. Neural Circuits* **12**, (2018).

71. McDonald, K. L. Out with the old and in with the new: rapid specimen preparation procedures for electron microscopy of sectioned biological material. *Protoplasma* **251**, 429–448 (2014).

72. Xu, C. S. *et al.* Enhanced FIB-SEM systems for large-volume 3D imaging. *eLife* **6**, e25916 (2017).

73. Xu, C. S. *et al.* An open-access volume electron microscopy atlas of whole cells and tissues. *Nature* **599**, 147–151 (2021).

74. Bayguinov, P. O., Fisher, M. R. & Fitzpatrick, J. A. J. Assaying three-dimensional cellular architecture using X-ray tomographic and correlated imaging approaches. *J. Biol. Chem.* **295**, 15782–15793 (2020).

75. Schermelleh, L. *et al.* Super-resolution microscopy demystified. *Nat. Cell Biol.* **21**, 72–84 (2019).

76. Honda, K., Takaki, T. & Kang, D. Recent advances in electron microscopy for the diagnosis and research of glomerular diseases. *Kidney Res. Clin. Pract.* **42**, 155–165 (2023).

77. Cheville, N. F. & Stasko, J. Techniques in electron microscopy of animal tissue. *Vet. Pathol.* **51**, 28–41 (2014).

78. Harris, K. M. *et al.* Uniform Serial Sectioning for Transmission Electron Microscopy. *J. Neurosci.* **26**, 12101–12103 (2006).

79. Hong, Y., Song, Y., Zhang, Z. & Li, S. Cryo-Electron Tomography: The Resolution Revolution and a Surge of In Situ Virological Discoveries. *Annu. Rev. Biophys.* **52**, 339–360 (2023).

80. Eisenstein, F. *et al.* Parallel cryo electron tomography on in situ lamellae. *Nat. Methods* **20**, 131–138 (2023).

81. Briggs, J. A. Structural biology in situ—the potential of subtomogram averaging. *Curr. Opin. Struct. Biol.* **23**, 261–267 (2013).

82. Yahav, T., Maimon, T., Grossman, E., Dahan, I. & Medalia, O. Cryo-electron tomography: gaining insight into cellular processes by structural approaches. *Curr. Opin. Struct. Biol.* **21**, 670–677 (2011).

83. Zimmermann, L. & Chlanda, P. Cryo-electron tomography of viral infection — from applications to biosafety. *Curr. Opin. Virol.* **61**, 101338 (2023).

84. Harapin, J., Eibauer, M. & Medalia, O. Structural Analysis of Supramolecular Assemblies by Cryo-Electron Tomography. *Structure* **21**, 1522–1530 (2013).

85. Lam, V. & Villa, E. Practical Approaches for Cryo-FIB Milling and Applications for Cellular Cryo-Electron Tomography. in *cryoEM: Methods and Protocols* (eds. Gonen, T. & Nannenga, B. L.) 49–82 (Springer US, New York, NY, 2021). doi:10.1007/978-1-0716-0966-8_3.

86. Peck, J. V., Fay, J. F. & Strauss, J. D. High-speed high-resolution data collection on a 200 keV cryo-TEM. *IUCrJ* **9**, 243–252 (2022).

87. Baena, V. *et al.* FIB-SEM as a Volume Electron Microscopy Approach to Study Cellular Architectures in SARS-CoV-2 and Other Viral Infections: A Practical Primer for a Virologist. *Viruses* **13**, 611 (2021).

88. Vidavsky, N. *et al.* Cryo-FIB-SEM serial milling and block face imaging: Large volume structural analysis of biological tissues preserved close to their native state. *J. Struct. Biol.* **196**, 487–495 (2016).

89. Wang, S. *et al.* CryoFIB milling large tissue samples for cryo-electron tomography. *Sci. Rep.* **13**, 5879 (2023).

90. Müller, W. G. *et al.* Towards an atlas of mammalian cell ultrastructure by cryo soft X-ray tomography. *J. Struct. Biol.* **177**, 179–192 (2012).

91. Groen, J., Conesa, J. J., Valcárcel, R. & Pereiro, E. The cellular landscape by cryo soft X-ray tomography. *Biophys. Rev.* **11**, 611–619 (2019).

92. Carzaniga, R., Domart, M.-C., Collinson, L. M. & Duke, E. Cryo-soft X-ray tomography: a journey into the world of the native-state cell. *Protoplasma* **251**, 449–458 (2014).

93. Schneider, G. Cryo X-ray microscopy with high spatial resolution in amplitude and phase contrast. *Ultramicroscopy* **75**, 85–104 (1998).

94. Thompson, R. F., Walker, M., Siebert, C. A., Muench, S. P. & Ranson, N. A. An introduction to sample preparation and imaging by cryo-electron microscopy for structural biology. *Methods* **100**, 3–15 (2016).

95. Iancu, C. V. *et al.* Electron cryotomography sample preparation using the Vitrobot. *Nat. Protoc.* **1**, 2813–2819 (2006).

96. Mastronarde, D. N. Dual-Axis Tomography: An Approach with Alignment Methods That Preserve Resolution. *J. Struct. Biol.* **120**, 343–352 (1997).

97. Valcárcel, R. *et al.* New Holder for Dual-Axis Cryo Soft X-Ray Tomography of Cells at the Mistral Beamline. in 427–429 (JACOW Publishing, Geneva, Switzerland, 2018). doi:10.18429/JACoW-MEDSI2018-THPH43.

98. Larabell, C. A. & Le Gros, M. A. X-ray Tomography Generates 3-D Reconstructions of the Yeast, Saccharomyces cerevisiae, at 60-nm Resolution. *Mol. Biol. Cell* **15**, 957–962 (2004).

99. Weiß, D. *et al.* Computed tomography of cryogenic biological specimens based on X-ray microscopic images. *Ultramicroscopy* **84**, 185–197 (2000).

100. Sherman, S. *et al.* Resolving new ultrastructural features of cytokinetic abscission with soft-X-ray cryo-tomography. *Sci. Rep.* **6**, 27629 (2016).

101. Kounatidis, I. *et al.* 3D Correlative Cryo-Structured Illumination Fluorescence and Soft X-ray Microscopy Elucidates Reovirus Intracellular Release Pathway. *Cell* **182**, 515-530.e17 (2020).

102. Duke, E. M. H. *et al.* Imaging endosomes and autophagosomes in whole mammalian cells using correlative cryo-fluorescence and cryo-soft X-ray microscopy (cryo-CLXM). *Ultramicroscopy* **143**, 77–87 (2014).

103. Chichón, F. J. *et al.* Cryo X-ray nano-tomography of vaccinia virus infected cells. *J. Struct. Biol.* **177**, 202–211 (2012).

104. Kepsutlu, B. *et al.* Cells Undergo Major Changes in the Quantity of Cytoplasmic Organelles after Uptake of Gold Nanoparticles with Biologically Relevant Surface Coatings. *ACS Nano* **14**, 2248–2264 (2020).

105. Dyhr, M. C. A. *et al.* 3D surface reconstruction of cellular cryo-soft X-ray microscopy tomograms using semisupervised deep learning. *Proc. Natl. Acad. Sci.* **120**, e2209938120 (2023).

106. Castro, V., Pérez-Berna, A. J., Calvo, G., Pereiro, E. & Gastaminza, P. Three-Dimensional Remodeling of SARS-CoV2-Infected Cells Revealed by Cryogenic Soft X-ray Tomography. *ACS Nano* (2023) doi:10.1021/acsnano.3c07265.

107. Hummel, E. *et al.* 3D Ultrastructural Organization of Whole Chlamydomonas reinhardtii Cells Studied by Nanoscale Soft X-Ray Tomography. *PLoS ONE* **7**, e53293 (2012).

108. Gal, A. *et al.* Native-state imaging of calcifying and noncalcifying microalgae reveals similarities in their calcium storage organelles. *Proc. Natl. Acad. Sci. U. S. A.* **115**, 11000–11005 (2018).

109. Uchida, M. *et al.* Quantitative Analysis of Yeast Internal Architecture using Soft X-ray Tomography. *Yeast Chichester Engl.* **28**, 227–236 (2011).

110. Kapishnikov, S. *et al.* Unraveling heme detoxification in the malaria parasite by in situ correlative X-ray fluorescence microscopy and soft X-ray tomography. *Sci. Rep.* **7**, 7610 (2017).

111. Otón, J. *et al.* XTEND: Extending the depth of field in cryo soft X-ray tomography. *Sci. Rep.* **7**, 45808 (2017).

112. Conesa, J. J. *et al.* Four-Dimensional Characterization of the Babesia divergens Asexual Life Cycle, from the Trophozoite to the Multiparasite Stage. *mSphere* **5**, e00928-20 (2020).

113. Harkiolaki, M. *et al.* Cryo-soft X-ray tomography: using soft X-rays to explore the ultrastructure of whole cells. *Emerg. Top. Life Sci.* **2**, 81–92 (2018).

114. Loconte, V. *et al.* Using soft X-ray tomography for rapid whole-cell quantitative imaging of SARS-CoV-2-infected cells. *Cell Rep. Methods* **1**, 100117 (2021).

115. Nahas, K. L. *et al.* Near-native state imaging by cryo-soft-X-ray tomography reveals remodelling of multiple cellular organelles during HSV-1 infection. *PLOS Pathog.* **18**, e1010629 (2022).

116. Perez-Berna, A. J. *et al.* Monitoring reversion of hepatitis C virus-induced cellular alterations by direct-acting antivirals using cryo soft X-ray tomography and infrared microscopy. *Acta Crystallogr. Sect. Struct. Biol.* **77**, 1365–1377 (2021).

117. Phillips, P. *et al.* Single Cell Cryo-Soft X-ray Tomography Shows That Each Chlamydia Trachomatis Inclusion Is a Unique Community of Bacteria. *Life* **11**, 842 (2021).

118. Chen, C. Z. *et al.* Drug Repurposing Screen for Compounds Inhibiting the Cytopathic Effect of SARS-CoV-2. *Front. Pharmacol.* **11**, 592737 (2021).

119. Schloer, S. *et al.* Drug synergy of combinatory treatment with remdesivir and the repurposed drugs fluoxetine and itraconazole effectively impairs SARS-CoV-2 infection in vitro. *Br. J. Pharmacol.* **178**, 2339–2350 (2021).

120. Baumeister, W., Grimm, R. & Walz, J. Electron tomography of molecules and cells. *Trends Cell Biol.* **9**, 81–85 (1999).

121. Koning, R. I., Koster, A. J. & Sharp, T. H. Advances in cryo-electron tomography for biology and medicine. *Ann. Anat. - Anat. Anz.* **217**, 82–96 (2018).

122. Alburquerque-González, B. *et al.* New role of the antidepressant imipramine as a Fascin1 inhibitor in colorectal cancer cells. *Exp. Mol. Med.* **52**, 281–292 (2020).

123. Lin, H. *et al.* Identification of novel macropinocytosis inhibitors using a rational screen of Food and Drug Administration-approved drugs. *Br. J. Pharmacol.* **175**, 3640–3655 (2018).

124. Mercer, J. & Helenius, A. Virus entry by macropinocytosis. *Nat. Cell Biol.* **11**, 510–520 (2009).

125. Mercer, J. & Helenius, A. Vaccinia Virus Uses Macropinocytosis and Apoptotic Mimicry to Enter Host Cells. *Science* **320**, 531–535 (2008).

126. Amstutz, B. *et al.* Subversion of CtBP1-controlled macropinocytosis by human adenovirus serotype 3. *EMBO J.* **27**, 956–969 (2008).

127. Bauherr, S. *et al.* Macropinocytosis and Clathrin-Dependent Endocytosis Play Pivotal Roles for the Infectious Entry of Puumala Virus. *J. Virol.* **94**, 10.1128/jvi.00184-20 (2020).

128. Zhang, Y.-Y. *et al.* SARS-CoV-2 hijacks macropinocytosis to facilitate its entry and promote viral spike–mediated cell-to-cell fusion. *J. Biol. Chem.* **298**, 102511 (2022).

129. Wichit, S. *et al.* Imipramine Inhibits Chikungunya Virus Replication in Human Skin Fibroblasts through Interference with Intracellular Cholesterol Trafficking. *Sci. Rep.* **7**, 3145 (2017).

130. Postma, M. & Goedhart, J. PlotsOfData—A web app for visualizing data together with their summaries. *PLOS Biol.* **17**, e3000202 (2019).

131. Capua-Shenkar, J. *et al.* Examining atherosclerotic lesions in three dimensions at the nanometer scale with cryo-FIB-SEM. *Proc. Natl. Acad. Sci.* **119**, e2205475119 (2022).

132. Baumer, Y., Mehta, N. N., Dey, A. K., Powell-Wiley, T. M. & Boisvert, W. A. Cholesterol crystals and atherosclerosis. *Eur. Heart J.* **41**, 2236–2239 (2020).

133. Hoffmann, M., Kleine-Weber, H. & Pöhlmann, S. A Multibasic Cleavage Site in the Spike Protein of SARS-CoV-2 Is Essential for Infection of Human Lung Cells. *Mol. Cell* **78**, 779-784.e5 (2020).

134. Walls, A. C. *et al.* Structure, Function, and Antigenicity of the SARS-CoV-2 Spike Glycoprotein. *Cell* **181**, 281-292.e6 (2020).

135. Shang, J. *et al.* Cell entry mechanisms of SARS-CoV-2. *Proc. Natl. Acad. Sci. U. S. A.* **117**, 11727–11734 (2020).

136. Hoffmann, M. *et al.* SARS-CoV-2 Cell Entry Depends on ACE2 and TMPRSS2 and Is Blocked by a Clinically Proven Protease Inhibitor. *Cell* **181**, 271-280.e8 (2020).

137. Zhao, M.-M. *et al.* Cathepsin L plays a key role in SARS-CoV-2 infection in humans and humanized mice and is a promising target for new drug development. *Signal Transduct. Target. Ther.* **6**, 1–12 (2021).

138. Wheeler, S. & Sillence, D. J. Niemann–Pick type C disease: cellular pathology and pharmacotherapy. *J. Neurochem.* **153**, 674–692 (2020).

139. Simmons, G. *et al.* Inhibitors of cathepsin L prevent severe acute respiratory syndrome coronavirus entry. *Proc. Natl. Acad. Sci.* **102**, 11876–11881 (2005).

140. Kleine-Weber, H., Elzayat, M. T., Hoffmann, M. & Pöhlmann, S. Functional analysis of potential cleavage sites in the MERS-coronavirus spike protein. *Sci. Rep.* **8**, 16597 (2018).

141. Gierer, S. *et al.* The Spike Protein of the Emerging Betacoronavirus EMC Uses a Novel Coronavirus Receptor for Entry, Can Be Activated by TMPRSS2, and Is Targeted by Neutralizing Antibodies. *J. Virol.* **87**, 5502–5511 (2013).

142. Qian, Z., Dominguez, S. R. & Holmes, K. V. Role of the Spike Glycoprotein of Human Middle East Respiratory Syndrome Coronavirus (MERS-CoV) in Virus Entry and Syncytia Formation. *PLOS ONE* **8**, e76469 (2013).

143. Ou, T. *et al.* Hydroxychloroquine-mediated inhibition of SARS-CoV-2 entry is attenuated by TMPRSS2. *PLoS Pathog.* **17**, e1009212 (2021).

144. Schmitz, G. & Müller, G. Structure and function of lamellar bodies, lipid-protein complexes involved in storage and secretion of cellular lipids. *J. Lipid Res.* **32**, 1539–1570 (1991).

145. Kendall, R. L. & Holian, A. Cholesterol-dependent molecular mechanisms contribute to cationic amphiphilic drugs' prevention of silica-induced inflammation. *Eur. J. Cell Biol.* **102**, 151310 (2023).

146. Mackenzie, A. H. Pharmacologic actions of 4-aminoquinoline compounds. *Am. J. Med.* **75**, 5–10 (1983).

147. Ohkuma, S. & Poole, B. Fluorescence probe measurement of the intralysosomal pH in living cells and the perturbation of pH by various agents. *Proc. Natl. Acad. Sci. U. S. A.* **75**, 3327–3331 (1978).

148. Schrezenmeier, E. & Dörner, T. Mechanisms of action of hydroxychloroquine and chloroquine: implications for rheumatology. *Nat. Rev. Rheumatol.* **16**, 155–166 (2020).

149. Koch, J. *et al.* TMPRSS2 expression dictates the entry route used by SARS-CoV-2 to infect host cells. *EMBO J.* **40**, e107821 (2021).

150. Wang, H. *et al.* SARS coronavirus entry into host cells through a novel clathrin- and caveolae-independent endocytic pathway. *Cell Res.* **18**, 290–301 (2008).

151. Rolain, J.-M., Colson, P. & Raoult, D. Recycling of chloroquine and its hydroxyl analogue to face bacterial, fungal and viral infections in the 21st century. *Int. J. Antimicrob. Agents* **30**, 297–308 (2007).

152. Shang, C. *et al.* Inhibitors of endosomal acidification suppress SARS-CoV-2 replication and relieve viral pneumonia in hACE2 transgenic mice. *Virol. J.* **18**, 46 (2021).

153. Hoffmann, M. *et al.* Chloroquine does not inhibit infection of human lung cells with SARS-CoV-2. *Nature* **585**, 588–590 (2020).

154. Wang, M. *et al.* Remdesivir and chloroquine effectively inhibit the recently emerged novel coronavirus (2019-nCoV) in vitro. *Cell Res.* **30**, 269–271 (2020).

155. Yao, X. *et al.* In Vitro Antiviral Activity and Projection of Optimized Dosing Design of Hydroxychloroquine for the Treatment of Severe Acute Respiratory Syndrome Coronavirus 2 (SARS-CoV-2). *Clin. Infect. Dis.* **71**, 732–739 (2020).

156. Liu, J. *et al.* Hydroxychloroquine, a less toxic derivative of chloroquine, is effective in inhibiting SARS-CoV-2 infection in vitro. *Cell Discov.* **6**, 1–4 (2020).

157. Barrantes, F. J. The constellation of cholesterol-dependent processes associated with SARS-CoV-2 infection. *Prog. Lipid Res.* **87**, 101166 (2022).

158. Baggen, J., Vanstreels, E., Jansen, S. & Daelemans, D. Cellular host factors for SARS-CoV-2 infection. *Nat. Microbiol.* **6**, 1219–1232 (2021).

159. Xia, Z. *et al.* Antidepressant-induced lipidosis with special reference to tricyclic compounds. *Prog. Neurobiol.* **60**, 501–512 (2000).

160. Bik, E. *et al.* Raman and fluorescence imaging of phospholipidosis induced by cationic amphiphilic drugs in endothelial cells. *Biochim. Biophys. Acta BBA - Mol. Cell Res.* **1869**, 119186 (2022).

161. Lüllmann, H., Lüllmann-Rauch, R. & Wassermann, O. Lipidosis induced by amphiphilic cationic drugs. *Biochem. Pharmacol.* **27**, 1103–1108 (1978).

162. Weston, S. *et al.* Broad Anti-coronavirus Activity of Food and Drug Administration-Approved Drugs against SARS-CoV-2 In Vitro and SARS-CoV In Vivo. *J. Virol.* **94**, e01218-20 (2020).

163. Breiden, B. & Sandhoff, K. Acid Sphingomyelinase, a Lysosomal and Secretory Phospholipase C, Is Key for Cellular Phospholipid Catabolism. *Int. J. Mol. Sci.* **22**, 9001 (2021).

164. Kornhuber, J. *et al.* Identification of New Functional Inhibitors of Acid Sphingomyelinase Using a Structure−Property−Activity Relation Model. *J. Med. Chem.* **51**, 219–237 (2008).

165. Kornhuber, J. *et al.* Identification of Novel Functional Inhibitors of Acid Sphingomyelinase. *PLoS ONE* **6**, e23852 (2011).

166. Lafourcade, C., Sobo, K., Kieffer-Jaquinod, S., Garin, J. & van der Goot, F. G. Regulation of the V-ATPase along the Endocytic Pathway Occurs through Reversible Subunit Association and Membrane Localization. *PLoS ONE* **3**, e2758 (2008).

167. Kummer, S. *et al.* Pharmacologically induced endolysosomal cholesterol imbalance through clinically licensed drugs itraconazole and fluoxetine impairs Ebola virus infection in vitro. *Emerg. Microbes Infect.* **11**, 195–207.

168. Lu, F. *et al.* Identification of NPC1 as the target of U18666A, an inhibitor of lysosomal cholesterol export and Ebola infection. *eLife* **4**, e12177 (2015).

169. Roff, C. F. *et al.* Type C Niemann-Pick Disease: Use of Hydrophobic Amines to Study Defective Cholesterol Transport. *Dev. Neurosci.* **13**, 315–319 (1991).

170. Rodriguez-Lafrasse, C. *et al.* Abnormal cholesterol metabolism in imipramine-treated fibroblast cultures. Similarities with Niemann-Pick type C disease. *Biochim. Biophys. Acta BBA - Lipids Lipid Metab.* **1043**, 123–128 (1990).

171. Gabandé-Rodríguez, E., Boya, P., Labrador, V., Dotti, C. G. & Ledesma, M. D. High sphingomyelin levels induce lysosomal damage and autophagy dysfunction in Niemann Pick disease type A. *Cell Death Differ.* **21**, 864–875 (2014).

172. Taksir, T. V. *et al.* Optimization of a Histopathological Biomarker for Sphingomyelin Accumulation in Acid Sphingomyelinase Deficiency. *J. Histochem. Cytochem.* **60**, 620–629 (2012).

173. Sun, A. Lysosomal storage disease overview. *Ann. Transl. Med.* **6**, 476 (2018).

174. Juhl, A. D. *et al.* Niemann Pick C2 protein enables cholesterol transfer from endo-lysosomes to the plasma membrane for efflux by shedding of extracellular vesicles. *Chem. Phys. Lipids* **235**, 105047 (2021).

175. Diesendorf, V. *et al.* Drug-induced phospholipidosis is not correlated with the inhibition of SARS-CoV-2 - inhibition of SARS-CoV-2 is cell line-specific. *Front. Cell. Infect. Microbiol.* **13**, (2023).

176. Tummino, T. A. *et al.* Drug-induced phospholipidosis confounds drug repurposing for SARS-CoV-2. *Science* **373**, 541–547 (2021).

177. Mahdi, M., Hermán, L., Réthelyi, J. M. & Bálint, B. L. Potential Role of the Antidepressants Fluoxetine and Fluvoxamine in the Treatment of COVID-19. *Int. J. Mol. Sci.* **23**, 3812 (2022).

178. Le Corre, P. & Loas, G. Difficulty in Repurposing Selective Serotonin Reuptake Inhibitors and Other Antidepressants with Functional Inhibition of Acid Sphingomyelinase in COVID-19 Infection. *Front. Pharmacol.* **13**, 849095 (2022).

179. Loas, G. & Le Corre, P. Update on Functional Inhibitors of Acid Sphingomyelinase (FIASMAs) in SARS-CoV-2 Infection. *Pharmaceuticals* **14**, 691 (2021).

180. Ballout, R. A., Sviridov, D., Bukrinsky, M. I. & Remaley, A. T. The lysosome: A potential juncture between SARS-CoV-2 infectivity and Niemann-Pick disease type C, with therapeutic implications. *FASEB J.* **34**, 7253–7264 (2020).

181. Daniloski, Z. *et al.* Identification of Required Host Factors for SARS-CoV-2 Infection in Human Cells. *Cell* **184**, 92-105.e16 (2021).

182. Ahmad, I. *et al.* An overview of the role of Niemann-pick C1 (NPC1) in viral infections and inhibition of viral infections through NPC1 inhibitor. *Cell Commun. Signal. CCS* **21**, 352 (2023).

183. Raïch-Regué, D. *et al.* β-Cyclodextrins as affordable antivirals to treat coronavirus infection. *Biomed. Pharmacother.* **164**, 114997 (2023).

184. Takano, T. *et al.* The cholesterol transport inhibitor U18666A inhibits type I feline coronavirus infection. *Antiviral Res.* **145**, 96–102 (2017).

185. YOSHIDA, Y. *et al.* Reduction of Acid Sphingomyelinase Activity in Human Fibroblasts Induced by AY-9944 and Other Cationic Amphiphific Drugs1. *J. Biochem. (Tokyo)* **98**, 1669–1679 (1985).

186. Côté, M. *et al.* Small molecule inhibitors reveal Niemann–Pick C1 is essential for Ebola virus infection. *Nature* **477**, 344–348 (2011).

187. Sanders, D. W. *et al.* SARS-CoV-2 requires cholesterol for viral entry and pathological syncytia formation. *eLife* **10**, e65962.

188. Li, X. *et al.* Dependence of SARS-CoV-2 infection on cholesterol-rich lipid raft and endosomal acidification. *Comput. Struct. Biotechnol. J.* **19**, 1933–1943 (2021).

189. Wang, S. *et al.* Cholesterol 25-Hydroxylase inhibits SARS-CoV-2 and other coronaviruses by depleting membrane cholesterol. *EMBO J.* **39**, e106057 (2020).

190. Wang, H. *et al.* The role of high cholesterol in SARS-CoV-2 infectivity. *J. Biol. Chem.* **299**, 104763 (2023).

191. Schneider, W. M. *et al.* Genome-Scale Identification of SARS-CoV-2 and Pan-coronavirus Host Factor Networks. *Cell* **184**, 120-132.e14 (2021).

192. García-Dorival, I. *et al.* Identification of Niemann-Pick C1 protein as a potential novel SARS-CoV-2 intracellular target. *Antiviral Res.* **194**, 105167 (2021).

193. Tang, T., Bidon, M., Jaimes, J. A., Whittaker, G. R. & Daniel, S. Coronavirus membrane fusion mechanism offers a potential target for antiviral development. *Antiviral Res.* **178**, 104792 (2020).

194. Carpinteiro, A. *et al.* Inhibition of acid sphingomyelinase by ambroxol prevents SARS-CoV-2 entry into epithelial cells. *J. Biol. Chem.* **296**, 100701 (2021).

195. Palacios-Rápalo, S. N. *et al.* Cholesterol-Rich Lipid Rafts as Platforms for SARS-CoV-2 Entry. *Front. Immunol.* **12**, (2021).

196. Roncato, R., Angelini, J., Pani, A. & Talotta, R. Lipid rafts as viral entry routes and immune platforms: A double-edged sword in SARS-CoV-2 infection? *Biochim. Biophys. Acta Mol. Cell Biol. Lipids* **1867**, 159140 (2022).

197. Bakillah, A. *et al.* Lipid Raft Integrity and Cellular Cholesterol Homeostasis Are Critical for SARS-CoV-2 Entry into Cells. *Nutrients* **14**, 3417 (2022).

198. Levental, I., Levental, K. R. & Heberle, F. A. Lipid Rafts: Controversies Resolved, Mysteries Remain. *Trends Cell Biol.* **30**, 341–353 (2020).

199. Storti, B. *et al.* A spatial multi-scale fluorescence microscopy toolbox discloses entry checkpoints of SARS-CoV-2 variants in Vero E6 cells. *Comput. Struct. Biotechnol. J.* **19**, 6140–6156 (2021).

200. Matsuyama, S. *et al.* Enhanced isolation of SARS-CoV-2 by TMPRSS2-expressing cells. *Proc. Natl. Acad. Sci.* **117**, 7001–7003 (2020).

201. Pires De Souza, G. A. *et al.* Choosing a cellular model to study SARS-CoV-2. *Front. Cell. Infect. Microbiol.* **12**, (2022).

202. Wang, M. & Petersen, N. O. Lipid-coated gold nanoparticles promote lamellar body formation in A549 cells. *Biochim. Biophys. Acta BBA - Mol. Cell Biol. Lipids* **1831**, 1089–1097 (2013).

203. Davoren, M. *et al.* In vitro toxicity evaluation of single walled carbon nanotubes on human A549 lung cells. *Toxicol. In Vitro* **21**, 438–448 (2007).

204. Vercellino, S. *et al.* Biological interactions of ferromagnetic iron oxide–carbon nanohybrids with alveolar epithelial cells. *Biomater. Sci.* **10**, 3514–3526 (2022).

205. Kononenko, V. *et al.* Harmful at non-cytotoxic concentrations: SiO2-SPIONs affect surfactant metabolism and lamellar body biogenesis in A549 human alveolar epithelial cells. *Nanotoxicology* **11**, 419–429 (2017).

206. Esquivel-Gaon, M. *et al.* Bismuth-based nanoparticles as the environmentally friendly replacement for lead-based piezoelectrics. *RSC Adv.* **5**, 27295–27304 (2015).

207. Burton, P. R., Stueckemann, J., Welsh, R. M. & Paretsky, D. Some ultrastructural effects of persistent infections by the rickettsia Coxiella burnetii in mouse L cells and green monkey kidney (Vero) cells. *Infect. Immun.* **21**, 556–566 (1978).

208. Brahim Belhaouari, D. *et al.* The Strengths of Scanning Electron Microscopy in Deciphering SARS-CoV-2 Infectious Cycle. *Front. Microbiol.* **11**, 2014 (2020).

209. Ng, M.-L., Tan, S.-H., See, E.-E., Ooi, E.-E. & Ling, A.-E. Y. 2003. Proliferative growth of SARS coronavirus in Vero E6 cells. *J. Gen. Virol.* **84**, 3291–3303.

210. Ng, M. l., Tan, S. h., See, E. e., Ooi, E. e. & Ling, A. e. Early events of SARS coronavirus infection in vero cells. *J. Med. Virol.* **71**, 323–331 (2003).

211. Schneider, M. *et al.* Severe Acute Respiratory Syndrome Coronavirus Replication Is Severely Impaired by MG132 due to Proteasome-Independent Inhibition of M-Calpain. *J. Virol.* **86**, 10112–10122 (2012).

212. Barreto-Vieira, D. F. *et al.* SARS-CoV-2: Ultrastructural Characterization of Morphogenesis in an In Vitro System. *Viruses* **14**, 201 (2022).

213. Caldas, L. A. *et al.* Intracellular host cell membrane remodelling induced by SARS-CoV-2 infection in vitro. *Biol. Cell* **113**, 281–293 (2021).

214. Barreto-Vieira, D. F. *et al.* Morphology and morphogenesis of SARS-CoV-2 in Vero-E6 cells. *Mem. Inst. Oswaldo Cruz* **116**, e200443 (2021).

215. OpenOrganelle. https://openorganelle.janelia.org/datasets/jrc_ccl81-covid-1.

216. Chen, F., Tillberg, P. W. & Boyden, E. S. Expansion microscopy. *Science* **347**, 543–548 (2015).

217. Chang, J.-B. *et al.* Iterative expansion microscopy. *Nat. Methods* **14**, 593–599 (2017).

218. Gambarotto, D. *et al.* Imaging cellular ultrastructures using expansion microscopy (U-ExM). *Nat. Methods* **16**, 71–74 (2019).

219. Truckenbrodt, S. *et al.* X10 expansion microscopy enables 25-nm resolution on conventional microscopes. *EMBO Rep.* **19**, e45836 (2018).

220. Klimas, A. *et al.* Magnify is a universal molecular anchoring strategy for expansion microscopy. *Nat. Biotechnol.* 1–12 (2023) doi:10.1038/s41587-022-01546-1.

221. Damstra, H. G. *et al.* Visualizing cellular and tissue ultrastructure using Ten-fold Robust Expansion Microscopy (TREx). *eLife* **11**, e73775 (2022).

222. M'Saad, O. & Bewersdorf, J. Light microscopy of proteins in their ultrastructural context. *Nat. Commun.* **11**, 3850 (2020).

223. Tillberg, P. W. & Chen, F. Expansion Microscopy: Scalable and Convenient Super-Resolution Microscopy. *Annu. Rev. Cell Dev. Biol.* **35**, 683–701 (2019).

224. Truckenbrodt, S. Expansion Microscopy: Super-Resolution Imaging with Hydrogels. *Anal. Chem.* **95**, 3–32 (2023).

225. Wassie, A. T., Zhao, Y. & Boyden, E. S. Expansion Microscopy: Principles and Uses in Biological Research. *Nat. Methods* **16**, 33–41 (2019).

226. Wen, G., Leen, V., Rohand, T., Sauer, M. & Hofkens, J. Current Progress in Expansion Microscopy: Chemical Strategies and Applications. *Chem. Rev.* **123**, 3299–3323 (2023).

227. Gao, M. *et al.* Expansion Stimulated Emission Depletion Microscopy (ExSTED). *ACS Nano* **12**, 4178–4185 (2018).

228. Zwettler, F. U. *et al.* Molecular resolution imaging by post-labeling expansion single-molecule localization microscopy (Ex-SMLM). *Nat. Commun.* **11**, 3388 (2020).

229. Kylies, D. *et al.* Expansion-enhanced super-resolution radial fluctuations enable nanoscale molecular profiling of pathology specimens. *Nat. Nanotechnol.* **18**, 336–342 (2023).

230. Tillberg, P. W. *et al.* Protein-retention expansion microscopy of cells and tissues labeled using standard fluorescent proteins and antibodies | Nature Biotechnology. *Nat. Biotechnol.* **34**, 987–992 (2016).

231. Kanazawa, T., Takematsu, H., Yamamoto, A., Yamamoto, H. & Kozutsumi, Y. Wheat germ agglutinin stains dispersed post-golgi vesicles after treatment with the cytokinesis inhibitor psychosine. *J. Cell. Physiol.* **215**, 517–525 (2008).

232. Tartakoff, A. M. & Vassalli, P. Lectin-binding sites as markers of Golgi subcompartments: proximal-to-distal maturation of oligosaccharides. *J. Cell Biol.* **97**, 1243–1248 (1983).

233. Damstra, H. G. J. *et al.* GelMap: intrinsic calibration and deformation mapping for expansion microscopy. *Nat. Methods* **20**, 1573–1580 (2023).

234. Yu, C.-C. (Jay) *et al.* Expansion microscopy of C. elegans. *eLife* **9**, e46249 (2020).

235. Shi, X. *et al.* Label-retention expansion microscopy. *J. Cell Biol.* **220**, e202105067 (2021).

236. Gambarotto, D., Hamel, V. & Guichard, P. Chapter 4 - Ultrastructure expansion microscopy (U-ExM). in *Methods in Cell Biology* (eds. Guichard, P. & Hamel, V.) vol. 161 57–81 (Academic Press, 2021).

237. Laporte, M. H., Klena, N., Hamel, V. & Guichard, P. Visualizing the native cellular organization by coupling cryofixation with expansion microscopy (Cryo-ExM). *Nat. Methods* **19**, 216–222 (2022).

238. Chozinski, T. J. *et al.* Expansion microscopy with conventional antibodies and fluorescent proteins. *Nat. Methods* **13**, 485–488 (2016).

239. Sarkar, D. *et al.* Revealing nanostructures in brain tissue via protein decrowding by iterative expansion microscopy. *Nat. Biomed. Eng.* **6**, 1057–1073 (2022).

240. Wen, G. *et al.* Evaluation of Direct Grafting Strategies via Trivalent Anchoring for Enabling Lipid Membrane and Cytoskeleton Staining in Expansion Microscopy. *ACS Nano* **14**, 7860–7867 (2020).

241. Krull, A., Buchholz, T.-O. & Jug, F. Noise2Void - Learning Denoising from Single Noisy Images. Preprint at https://doi.org/10.48550/arXiv.1811.10980 (2019).

242. Chen, M. *et al.* Convolutional neural networks for automated annotation of cellular cryo-electron tomograms. *Nat. Methods* **14**, 983–985 (2017).

243. von Chamier, L. *et al.* Democratising deep learning for microscopy with ZeroCostDL4Mic. *Nat. Commun.* **12**, 2276 (2021).

244. Nahas, K. L., Fernandes, J. F., Crump, C., Graham, S. & Harkiolaki, M. Contour, a semi-automated segmentation and quantitation tool for cryo-soft-X-ray tomography. 2021.12.03.470962 Preprint at https://doi.org/10.1101/2021.12.03.470962 (2021).

245. Luengo, I. *et al.* SuRVoS: Super-Region Volume Segmentation workbench. *J. Struct. Biol.* **198**, 43–53 (2017).

246. Pennington, A. *et al.* SuRVoS 2: Accelerating Annotation and Segmentation for Large Volumetric Bioimage Workflows Across Modalities and Scales. *Front. Cell Dev. Biol.* **10**, (2022).

247. Schindelin, J. *et al.* Fiji: an open-source platform for biological-image analysis. *Nat. Methods* **9**, 676–682 (2012).

248. Belevich, I., Joensuu, M., Kumar, D., Vihinen, H. & Jokitalo, E. Microscopy Image Browser: A Platform for Segmentation and Analysis of Multidimensional Datasets. *PLOS Biol.* **14**, e1002340 (2016).

249. Gilbert, P. Iterative methods for the three-dimensional reconstruction of an object from projections. *J. Theor. Biol.* **36**, 105–117 (1972).

250. Zehtabian, A. *et al.* Precise measurement of nanoscopic septin ring structures with deep learning-assisted quantitative superresolution microscopy. *Mol. Biol. Cell* **33**, ar76 (2022).

251. Péricat, D. *et al.* Antiviral and Anti-Inflammatory Activities of Fluoxetine in a SARS-CoV-2 Infection Mouse Model. *Int. J. Mol. Sci.* **23**, 13623 (2022).

252. Rosen, D. A. *et al.* Modulation of the sigma-1 receptor–IRE1 pathway is beneficial in preclinical models of inflammation and sepsis. *Sci. Transl. Med.* **11**, eaau5266 (2019).

253. Dallé, E., Daniels, W. M. U. & Mabandla, M. V. Fluvoxamine maleate normalizes striatal neuronal inflammatory cytokine activity in a Parkinsonian rat model associated with depression. *Behav. Brain Res.* **316**, 189–196 (2017).

254. Lim, C.-M. *et al.* Fluoxetine affords robust neuroprotection in the postischemic brain via its anti-inflammatory effect. *J. Neurosci. Res.* **87**, 1037–1045 (2009).

255. Sukhatme, V. P., Reiersen, A. M., Vayttaden, S. J. & Sukhatme, V. V. Fluvoxamine: A Review of Its Mechanism of Action and Its Role in COVID-19. *Front. Pharmacol.* **12**, (2021).

256. Mehta, P. *et al.* COVID-19: consider cytokine storm syndromes and immunosuppression. *The Lancet* **395**, 1033–1034 (2020).

257. Asadi Anar, M. *et al.* Selective serotonin reuptake inhibitors: New hope in the fight against COVID-19. *Front. Pharmacol.* **13**, (2022).

258. Sun, D. *et al.* Click-ExM enables expansion microscopy for all biomolecules. *Nat. Methods* **18**, 107–113 (2021).

259. Götz, R. *et al.* Nanoscale imaging of bacterial infections by sphingolipid expansion microscopy. *Nat. Commun.* **11**, 6173 (2020).

260. White, B. M., Kumar, P., Conwell, A. N., Wu, K. & Baskin, J. M. Lipid Expansion Microscopy. *J. Am. Chem. Soc.* **144**, 18212–18217 (2022).

261. Halpern, A. R., Alas, G. C. M., Chozinski, T. J., Paredez, A. R. & Vaughan, J. C. Hybrid Structured Illumination Expansion Microscopy Reveals Microbial Cytoskeleton Organization. *ACS Nano* **11**, 12677–12686 (2017).

262. Weinhardt, V. *et al.* Switchable resolution in soft x-ray tomography of single cells. *PLoS ONE* **15**, e0227601 (2020).

263. Fahy, K. *et al.* Compact Cell Imaging Device (CoCID) provides insights into the cellular origins of viral infections. *J. Phys. Photonics* **3**, 031002 (2021).

264. Fahy, K. *et al.* A Laboratory Based Soft X-ray Microscope for 3D Imaging of Whole Cells. *Microsc. Microanal.* **29**, 1171–1172 (2023).

265. Rubino, S. *et al.* A site-specific focused-ion-beam lift-out method for cryo Transmission Electron Microscopy. *J. Struct. Biol.* **180**, 572–576 (2012).

266. Kremer, J. R., Mastronarde, D. N. & McIntosh, J. R. Computer visualization of three-dimensional image data using IMOD. *J. Struct. Biol.* **116**, 71–76 (1996).